Contributions to the Analysis and Design of Primary and Secondary Controllers of Electronic Power Converters in Power Systems

by
Diana Patricia Morán Río

supervised by
Dr. Javier Roldán Pérez
Dr. Milan Prodanović
Prof. Dr. Aurelio García Cerrada

a dissertation submitted to ICAI School of Engineering
in partial fulfilment of the requirements for the
degree of doctor of philosophy

ICAI School of Engineering
Universidad Pontificia Comillas

Madrid, January 2024

It matters not how strait the gate,
How charged with punishments the scroll,
I am the master of my fate,
I am the captain of my soul.

Invictus (1875), William Ernest Henley

Acknowledgements

After more than four years of work, I would like to dedicate some words to those that have somehow contributed to this Thesis. Firstly, I would like to thank my thesis advisors. I would like to specially thank Dr. Milan Prodanović and Dr. Javier Roldán Pérez for giving me the opportunity to devote these years to do research in this field, it has make me grow both personally and professionally. I would like to thank Dr. Javier Roldán Pérez for his close guidance through the PhD process, the teaching sessions and insightful comments and suggestions that have greatly improved the quality of this work. I would also like to thank Dr. Milan Prodanović for his encouragement to perform high-quality research, his profound questions and his mentoring sessions. Finally, I also thank Prof. Dr. Aurelio García Cerrada for his suggestions in the research topics, the thorough review of the published work and his help in the bureaucratic steps.

I thank the colleagues with whom I have shared so many hours in IMDEA: Adriana, Alberto E., Alberto R., Álex, Ebi, Érick, Marco and Josemi for all your help during these four years and especially thank you for the laughs and moments shared during breaks. I greatly appreciate the friendship built with the other PhD students: Pablo, Dion and Njegos. Guys, thank you for your help, your supporting words and the lessons and discussions on languages, Balcan culture, climbing, food, music and other not so important topics.

I would like to express my gratitude to Dr. Adolfo Anta, who gave me the opportunity to spend three months at the Power System Planning and Operation group of the Austrian Institute of Technology, in the beautiful city of Vienna. He broadened my view of electronic power converters in power systems. His research guidance and thorough comments have greatly contributed to one of the chapters of this Thesis and the associated publication. I would also like to thank the rest of the team in Vienna that made me feel so welcome in a post lockdown situation.

I thank IMDEA Energy for providing financial support to develop this research and for allowing me to use the laboratory facilities to develop a more complete piece of research. I would also like to thank IMDEA Energy researchers and management staff that create an open an warm environment to do research.

I would also like express my gratitude to the institutions that have provided fi-

nancial support to carry out this research: Spanish Government, which has partially financed this thesis with the project RTC-2017-6262-3 (*"MICROGRID-ON-CHIP: Inversor de baterías con control integrado de convertidor y microrred"*), Fundación Iberdrola España that funded the project *"CoorAlma: Coordinación de almacenamiento distribuido para mejorar la continuidad de suministro en redes de distribución"* and Generadores Europeos-Genesal through project "*NEXTFACTORY: Estudio de recuperación energética en ensayos de validación de grupos electrógenos*".

Last but not the least, I would like to thank my family and friends for their endless support and patience. I specially thank Cristian for his time, his encouragement and for taking care of me. Finally, I thank my family, they have provided me with everything that they have and I needed so I could develop my career.

Abstract

Electric power systems have experienced important changes in the past decades due to the massive integration of renewable energy sources. The adoption of these new sources not only imply changes in the generation mix but also in the technology, the size and the location of the generators. Conventional generation is mostly interfaced by using synchronous generators whereas renewable energy sources are commonly interfaced by using electronic power converters. Compared to synchronous generators, electronic power converters are faster and more flexible. However, the latter do not have rotating parts or kinetic energy stored and then cannot easily provide inertia to power systems. In addition, renewable energy sources are more spread across electrical networks and their size is smaller compared to conventional power plants.

In this context, the concept of microgrid (MG) was proposed to integrate distributed energy resources (DERs) and supply loads in remote areas. In this way, small renewable energy resources can substitute less efficient solutions such as diesel generators. Initially, the main intention of MGs was to feed small-scale isolated electrical grids, however, they can also be operated connected to the main grid. In islanded operation, the energy balance must be established within the MG, while in grid-connected operation the MG can import or export energy according to its availability and the market conditions. Moreover, due to the inherent flexibility of converter interfaced generation, MGs can provide ancillary services when connected to electrical grids.

To guarantee the quality of power supply, MG operation tasks are divided into three layers of control similar to the control layers in conventional grids. The lowest level, primary control, is responsible for the local control of devices. Then secondary control coordinates the operation of all devices. Finally, the objective of the tertiary control is the economic optimization of the grid. Although similar, converter controllers in MGs present some differences compared to the control of electronic power converters in conventional grids. For example, there are some primary controller designs that were proposed for their application in MGs and are now becoming more present in conventional grids. In addition, the secondary control that coordinates the synchronization and the islanding can only be found in MGs.

This thesis addresses the control of electronic power converters in MGs. It focuses

on the study of primary and secondary controllers for MGs. A common tool used to assess the stability of power systems is used along the thesis to study, from the stability point of view, the interactions between controllers applied at different layers, and the coordination of MG devices. Studies were validated using simulations. Part of them were also validated experimentally in a facility with several converters. At the end of the thesis, conclusions are drawn and some future research guidelines proposed.

Contents

List of Figures

List of Tables

Acronyms

AC Alternating current

AVR Automatic voltage regulator

BESS Battery energy storage system

COI Center of inertia

DC Direct current

DER Distributed energy resource

DFIG Doubly-fed induction generator

DSOGI Dual second order generalized integrator

DVPP Dynamic virtual power plant

ESS Energy storage system

GFL Grid-following

GFM Grid-forming

LPF Low-pass filter

MA Multi-agent

MG Microgrid

PCC Point of common coupling

PI Proportional-integral

PLL Phase-locked loop

PV Photovoltaic

RTT Real time targets

SEIL Smart energy integration lab

SG Synchronous generator

SOC State of charge

SRF Synchronous reference frame

VISMA Virtual synchronous machine [2]

VOC Virtual oscillator control

VPP Virtual power plant

VSC Voltage source converter

VSM Virtual synchronous machine [3]

Chapter 1

Introduction

In this thesis, stability and dynamic characteristics of microgrids (MGs) formed by power converters and synchronous generators (SGs) are explored. Special attention is paid to grid-forming (GFM) control strategies and their response in case of external events (i.e., frequency and voltage variations). A state of the art is presented and several primary and secondary control approaches are proposed. These control approaches are analytically evaluated to understand their impact in the MG small-signal stability. The proposed control systems were implemented in a laboratory in order to validate the main findings of this work. Conclusions and suggestions for further research are provided in the final part of the document.

1.1 Background and Overview

The decarbonization of electrical systems is giving rise to major changes in the electricity generation paradigm. In particular, traditional generation systems based on gas, coal and nuclear reactions, among others, are being replaced by renewable energy sources. These changes are leading to substantial modifications in the operation and planning of power systems as conventional and renewable generation feature substantially different characteristics [4–7].

From the planning point of view, the main differences are found in the size of the power plants, their location and the energy availability. Conventional power plants are usually large facilities located far away from the final consumers while renewable energy plants vary more in size and are more dispersed across the grid. In addition, the energy produced in conventional power plants usually comes from resources such as coal, water and gas. These resources are dispatchable and, therefore, the energy production can be adjusted according operator's requirements. However, for renewable energy sources, the power generation depends to a great extend on the environmental conditions. This means that renewable energy sources make the operation and control of power systems

more complex. Moreover, as power generation is becoming more dispersed, the direction of power flows can eventually change and there is a greater inherent uncertainty in the generation mix. In that respect, energy storage has become a key actor as is able to counteract the fluctuations in renewable energy production [8].

From the operation point of view, conventional and renewable generation also present significantly different characteristics. Solar power, wind power and batteries are connected to the grid by using power converters, and unlike traditional generators, these devices do not rely on rotating masses in the generation process. Therefore, they exhibit significantly faster dynamics [4]. In these technologies, the power is injected to the grid by means of an electronic device (a power converter) based on switching elements (i.e., semiconductors), filters and control systems. Power converters introduce both challenges and opportunities as these devices are more flexible than conventional generators, but also more prone to produce instabilities.

Renewable generators and batteries must fulfil grid-code requirements and, in this regard, the control system of the power converter is very relevant. Grid codes establish that these generators must fulfil certain power quality standards and should not cause instabilities [9]. In addition, renewable generators and batteries are expected to support the grid by providing grid services [10].

In power systems with a low share of renewable generators, the integration of additional renewable generation is rather simple as the system dynamics are kept almost unaltered. Moreover, the operation principles of renewable generators in these scenarios have already been studied in detail. However, when the share of renewable generation increases substantially, new dynamic interactions emerge. For instance, the total system inertia is substantially reduced. This may result in more significant frequency excursions after disturbances, which can eventually trigger protections and cause undesired cascaded effects [6]. Moreover, when the controllers of power converters are tuned with traditional methodologies, power converters may interact with the controllers of SGs, or with the controllers of other power converters, causing instabilities [5].

This thesis is focused in small-scale grids with high penetration of renewable energy sources, often known as MGs [11, 12], with special emphasis in control systems. This topic is attracting a lot of attention from industry and academia due to the changes that are taking place in the electricity generation worldwide.

1.2 Introduction to Microgrids

MGs had been proposed several decades ago as a solution for the integration of distributed energy resources, energy storage systems (ESSs) and controllable loads to electrical grids [11, 13]. These small-scale electrical networks are custom made for each application and the generation is usually based on a mix of renewable and traditional energy sources available locally [12]: photovoltaic (PV), wind, hydro, diesel, etc. In

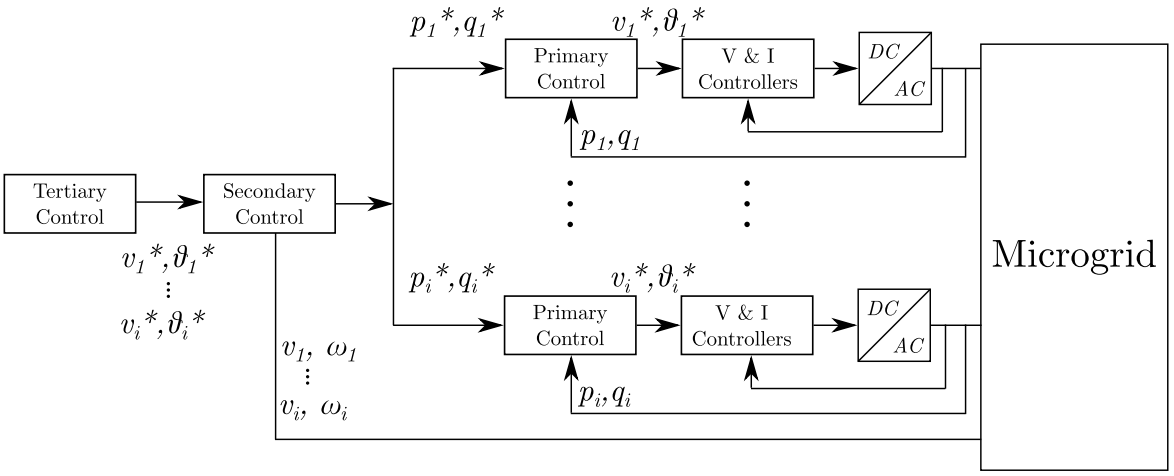

Figure 1.1: Hierarchical control structure of a MG, including the variables exchanged between layers [1].

this scenario, energy storage helps in the integration of non-dispachable resources such as wind and solar generation.

MGs are frequently used to provide power to isolated areas, where there is no connection to the utility grid, or when this connection is not reliable. In these cases, MGs operate isolated from the main grid. This operation mode is commonly known as "islanded mode". MGs can also be operated connected to the main grid, and this is commonly known as "grid-connected mode". In islanded mode, the power balance needs to be satisfied within the MG and, therefore, the MG control system should take care of the voltage and frequency levels. In grid-connected mode, the power balance is achieved by exchanging energy with the main grid since the latter sets the voltage and frequency of the MG. In this mode, MGs can provide ancillary services to the main grid by acting as controllable sources of active and reactive power.

1.3 Overview of Microgrid Control Systems

A hierarchical control scheme is commonly used in MGs [12, 14, 15]. With this control structure, MGs are able to provide many grid functionalities, in a similar way a grid controller would do it. Commonly, the control system of a MG consists of four control layers, as shown in Fig. 1.1: zero-level control (i.e., inner voltage and current control loops), primary, secondary and tertiary control. Each control level has its own control objective and generates set points for the control layer below. The lowest control layer is known as zero-level control [14]. It is a local control and it is often considered as part of the primary control layer. It includes the fastest control loops and it should guarantee adequate values of voltages and currents. These internal loops often include a

virtual impedance that simplifies the operation of converters acting as voltages sources in parallel configuration [16].

The primary control layer is applied locally, and its main objective is to maintain the voltage and frequency values within reasonable ranges during fast transients. Nevertheless, primary controllers also help in sharing the active and reactive power consumed by the loads and generate set point values for the zero-layer control. There are many options to implement the primary controller of converters. Among them, the most widely spread are droop control [14], virtual synchronous machine [3] (VSM) [2,3,17,18], synchronverter [19], SG matching [18,20] and virtual oscillator control (VOC) [18,21].

Droop control, VSMs and synchronverters mimic the dynamic characteristics of SGs to different extents. For droop controllers, the steady-state characteristic of conventional generators is adopted, although the control gains are not directly linked with the physical parameters of SGs. For VSMs and synchronverters, the swing and voltage equations of a SG are explicitly expressed to different extents. As demonstrated in the literature, under some considerations droops and VSMs are equivalent [22]. The so-called SG matching strategy considers the energy stored in the direct current (DC) capacitor of the converter to define its frequency (in a similar way as kinetic energy defines the frequency in SGs). Recently, a controller called VOC has been proposed as primary controller for power converters. This control option mimics the dynamics of a non-linear oscillator, which have inherent synchronisation properties. These features are utilised in the VOC control to synchronise power converters [23]. Due to the similarities of some primary controllers and SGs, converters with these controllers are commonly considered as providers of virtual (or synthetic) inertia. Synthetic inertia can be seen as the emulation of the natural response of a SG in the case of frequency variations (however, it should be noted there is no real shaft spinning in a power converter). This feature can be utilised to mitigate the lack of inertia in low-inertia power systems. Indeed, primary controllers have a significant impact on the dynamics of MGs and power systems formed by power converters.

The droop characteristic of primary control introduces voltage and frequency deviations from their set point values. Therefore, a secondary control is commonly used to restore the voltage and frequency to their nominal values [12]. Secondary control is also responsible for the coordination of MG devices. In this regard, it drives MG devices to the operating points defined by the tertiary controller. This task includes the operation in grid-connected mode, islanded mode and the transition between them [14,24].

Tertiary control is the highest level of control and it is in charge of the economic operation. In MGs, the role of tertiary control is crucial as it finds the optimal unit commitment of highly variable renewable energy resources. This control level commonly includes an optimal power flow algorithm that takes into account both energy-related aspects (losses, energy availability from generation and storage, etc.) and economic aspects (markets and depreciation of storage devices, among others) [12,14]. In MGs

connected to the main grid or to other MGs, it also defines the active and reactive power exchanged according to the set points provided by the grid operator, or by some pre-established rules (e.g., long-term contracts, etc.) [12].

1.4 Interactions between Primary Controllers

In islanded MGs, voltage and frequency have to be set and controlled by the devices that form the MG. This is commonly known as "forming the grid" and the devices that perform this task are known as GFM devices [25]. A simple control solution is to firstly deploy a GFM device and then to allow the connection of other devices that follow that voltage. This other control approach is known as grid-following (GFL) mode or, alternatively, grid-feeding mode [4, 26]. In the past, GFM in MGs relied on diesel generation sets, however, in recent years there have been several examples of droop-controlled power converters taking over this role.

The most common converter topology for GFL devices is a current-controlled voltage source converter (VSC) with a phase-locked loop (PLL) that is used to synchronise the converter with the voltage of the connection point. A control system based on a PLL works correctly in stiff grids and when the grid dynamics are relatively slow [26]. However, it has been demonstrated that the PLL has a strong influence on the stability of grid-tied converters. Particularly, in MGs the design of PLLs is conditioned by the controllers of the GFM devices [27].

1.5 Virtual Inertia Provision

The substitution of conventional generation by renewable generation is reducing power system inertia. In response to this situation, most system operators request the participation of renewable power plants in frequency-related ancillary services such as fast frequency response and inertia emulation [28–30]. These services are usually aimed at large power plants, which are the common actors in ancillary-service markets. Still, power ratings of distributed generators are significantly smaller and, in order for them to participate in these markets, they need to be aggregated first using the virtual power plant (VPP) concept [31] or via MGs. However, frequency-support actions of these aggregations are often unpredictable. In other words, as it is difficult to ensure the injection of specific power profiles during frequency events, the participation of these entities in frequency markets is not straightforward. This aspect has attracted the attention of researchers and the concept of dynamic virtual power plant (DVPP) has been proposed for the provision of ancillary services [32]. A DVPP is an aggregation of distributed energy resources (DERs) and loads that are placed in the same geographical area or feeder. Then, this aggregation can be used not only to follow power set points

sent by the grid operator but also to provide a combined response to certain grid events (i.e., ancillary services).

1.6 Design of Secondary Controllers

As mentioned before, hierarchical control is typically used to coordinate the operation of MGs [14]. Primary controllers like droops produce voltage and frequency deviations. The principal aims of secondary control are to restore voltage and frequency to their nominal values and to coordinate the operation of the MG devices [33].

Since the different control layers are cascaded, there should be sufficient bandwidth separation between them so they do not interact with each other. This makes secondary controllers slower than primary controllers. In conventional power systems, the time scale of the secondary frequency control is in the range from half a minute to half an hour due to the relatively slow dynamics of SGs [6]. However, primary controllers of converters have responses in the range of milliseconds and, therefore, secondary controllers can be designed to be much faster than in conventional grids. As secondary controllers are faster, communication delays during sending and receiving information processes have a significant impact on the system stability. Nowadays, the time range of secondary controllers in converter-dominated power networks is a major concern for researchers [6, 33, 34].

1.7 Microgrid Coordination and Synchronisation

The secondary control level coordinates the operation of all devices so that the high-level decisions made at the tertiary level can be applied. Among the coordination tasks, synchronisation of MGs operated in islanded mode with the main grid is a relevant issue. Synchronisation becomes challenging if the MG is formed by a mix of GFM and GFL devices, which is typically the case in MGs operated with batteries and renewable energy sources [35].

The seamless transition between the two operating modes and the integration of ESSs have been identified as some of the main challenges that MGs face nowadays [12]. Seamless transition ensures that the benefits of both control modes can be enjoyed. Due to their dispachability and dynamic characteristics, ESSs can help on the operation of MGs and ease the synchronization process [36].

1.8 Scope and Contributions and of this Research Work

The main objective of this research work has been to analyse and design primary and secondary controllers of MGs to facilitate the integration of renewable energy sources in power systems. This main research topic has been addressed from several perspectives:

- The impact of primary and secondary controllers in the small-signal stability of low-inertia power networks and MGs.
- The provision of synthetic inertia and frequency support with MGs formed by different GFM and GFL units.
- The design of secondary controllers for MGs considering the interactions between control layers and communication systems.
- The coordination of renewable energy sources and batteries in MGs to ensure seamless transitions between islanded and grid-connected operation modes.

The main contributions of this work are as follows:

1. Primary controllers of GFM and GFL converters and SGs have been widely studied for stiff grids. However, dynamic interactions between them in MGs and low-inertia power networks have been less studied. In this thesis, an exhaustive characterization of the dynamic interactions between primary controllers of power converters in MGs is conducted.
2. A detailed guideline is proposed for the design of primary controllers in MGs. The aim of this guideline is to avoid dynamic interactions between MG elements and to improve system robustness.
3. A methodology is proposed to calculate the control parameters of an aggregation of devices (i.e., a MG) so that they provide a specific power profile in case of variations in the grid frequency. This methodology can be applied offline, or during operation if the operating conditions of the aggregated devices change (e.g., the operating point, etc.). This feature is useful to ensure some pre-defined response to grid events when operating conditions change.
4. The well-known small-signal stability tools (eigenvalues, participation factors, etc.) have been applied to MGs and some additional tools have been proposed. These additional tools are based on the sensitivity of eigenvalues with respect to variations in system parameters. With these tools several eigenvalues of a MG can be placed at predefined places, simultaneously.

5. The coupling between primary and secondary controllers of MGs has been studied by using small-signal stability tools. By using these tools, it has been possible to understand the impact of communication delays and speed of controllers in the small-signal stability of a MG. Based on these results, some recommendations for the design of secondary controllers are given.

6. Traditional droop-based power sharing characteristics are considered to design the secondary controller of a MG. This controller coordinates the operation of electronic power converters with focus on the synchronisation process. The proposed secondary controller can maintain the operating point of certain GFM devices unaltered while batteries (and other selected GFM units) inject the required power in specific MG operations such as the synchronisation process.

7. The main findings in the field of primary controllers were tested experimentally in a laboratory with converters rated at 15 kW and 75 kW. The test system consisted of a GFM unit (SG or converter), a GFL converter and a load. Then, the contributions in the aggregation of GFM and GFL units were verified in the same laboratory. For that purpose, a benchmark low-voltage MG proposed by Cigré was replicated in the laboratory [37]. Finally, the contributions in the field of MG coordination were verified in the same benchmark MG by using hardware in the loop (HIL) simulations.

Some of the results presented in the following chapters were compiled and published in two journal articles and three conference articles:

1. D. P. Morán-Río, A. Anta, J. Roldán-Pérez, M. Prodanović, and A. García-Cerrada, "Coordination of Distributed Resources for Frequency Support Provision in Microgrids," in International Journal of Electrical Power & Energy Systems, vol. 155 (B), pp. 109539, Jan 2024, doi: 10.1016/j.ijepes.2023.109539.

2. D. P. Morán-Río, J. Roldán-Pérez, M. Prodanović, and A. García-Cerrada, "Influence of the Phase-Locked Loop on the Design of Microgrids Formed by Diesel Generators and Grid-Forming Converters," in IEEE Transactions on Power Electronics, vol. 37, no. 5, pp. 5122-5137, May 2022, doi: 10.1109/TPEL.2021.3127310.

3. D. P. Morán-Río, J. Roldán-Pérez, M. Prodanović, and A. García-Cerrada, "Enabling the Seamless Coordination and Synchronization of Microgrids using Batteries," 2023 IEEE International Conference on Environment and Electrical Engineering (EEEIC), Madrid, Spain, 2023, pp. 1-6, doi: 10.1109/EEEIC/ICPSEurope 57605.2023.10194700.

4. D. P. Morán-Río, J. Roldán-Pérez, M. Prodanović, and A. García-Cerrada, "Small-Signal Analysis of a Microgrid with Secondary Control Including the Dynamics of

Primary Control and Communication Delays," 2022 IEEE PES Innovative Smart Grid Technologies Conference Europe (ISGT-Europe 2022), Novi Sad, Serbia, 2022, pp. 1-5, doi: 10.1109/ISGT-Europe54678.2022.9960692.

5. D. P. Morán-Río, J. Roldán-Pérez, M. Prodanović, and A. García-Cerrada, "Influence of PLL Parameters on Small-Signal Stability of Microgrids with Synchronous Generators," 2020 IEEE Energy Conversion Congress and Exposition (ECCE), 2020, pp. 2451-2458, doi: 10.1109/ECCE44975.2020.9235342.

The author of this thesis also collaborated in:

1. J. Roldán-Pérez, D. P. Morán-Rio, D. Moutevelis, P. Rodríguez-Ortega, N. Jankovic, M. E. Zarei, and M. Prodanović, "Emulation of Complex Grid Scenarios by using Power Hardware In the Loop (PHIL) Techniques," 47th Annual Conference of the IEEE Industrial Electronics Society (IECON 2021), Toronto, Canada, 2021, pp. 1-6, doi: 10.1109/IECON48115.2021.9589168.

1.9 Thesis Outline

This thesis is divided into seven chapters and two appendices. Chapters describe the essential work while appendices include important information that can be omitted in a first reading, but will certainly be useful for a more detailed analysis.

Chapter 1 presents the topic of the thesis. Challenges of modern power systems and MGs are presented, together with a brief introduction to the control of power converters in those systems. Objectives, contributions and an outline of this document are also described here.

Chapter 2 gathers the state of the art of control systems for power converters. Primary and secondary controllers proposed in the literature are analysed to establish the research gap that is addressed in this thesis.

Chapter 3 focuses on the stability of primary controllers. Primary controllers in MGs are modelled and their interactions studied by using small-signal analysis tools. Results are validated in a laboratory environment.

Chapter 4 addresses the design of primary controllers of several GFM units to shape the frequency dynamics of MGs. A methodology based on small-signal analysis tools is proposed to automatically tune controllers when MG conditions change so that the MG dynamics are preserved. The methodology has been applied in a lab-scale MG for its validation.

Chapter 5 analyses two possible limitations in the design of secondary controllers: the bandwidth of primary controllers and communication delays. Eigenvalue analysis is used for the analysis.

Chapter 6 is dedicated to the use of ESSs to improve the operation of MGs, with special attention to MG synchronisation. A secondary controller is proposed. This controller provides the required power for synchronisation and transitions with ESSs while other GFM devices maintain their operating point. The proposed controller is validated using real time simulations.

Chapter 7 presents the conclusions and contributions and provides guidelines for further research.

In the Appendices, complementary information can be found. Appendix A contains the small-signal models of the MGs presented in Chapter 3. Appendix B describes the laboratory where the experimental validation of this research was carried out.

Chapter 2

State of the Art

The objective of this chapter is to present the state of the art of several control systems for electronic power converters in microgrids (MGs) and identify the research gaps addressed in this thesis. Section 2.1 describes the topology of the electronic power converters that are commonly used to interface renewable energy sources. The internal control of those power converters is discussed in Section 2.2 while their control in a MG context is presented in Section 2.3. Section 2.4 presents an overview of secondary controllers for MGs. Section 2.5 focus on the primary control of MGs and on the dynamic interactions between phase-locked loops (PLLs) and other controllers. Section 2.6 describes the design of primary controllers for the provision of synthetic inertia and other grid services. Relevant aspects that influence the design of secondary controllers are addressed in Section 2.7. In Section 2.8, coordination and synchronisation aspects related to secondary control are presented. Finally, the research gaps identified in the state of the art are summarised in Section 2.9.

2.1 Electronic Power Converters

Photovoltaic (PV) solar, wind turbines and batteries are typically interfaced with the grid via electronic power converters. In some cases, renewable energy sources can be integrated without an electronic interface, although in this case the fulfillment of grid codes is becoming increasingly difficult [4, 38]. PV panels are commonly connected by using a direct current (DC)/alternating current (AC) converter[1], although in some cases, an intermediate DC/DC converter is added in order to improve flexibility [4]. A similar converter topology is commonly used for batteries[2]. In the case of wind generators, the topology of the converter depends on the type of electric machine coupled to

[1]DC/AC converter because energy most often go from the DC side to the AC side but, when these converters are reversible, they could also be called AC/DC.

[2]The need for "reversibility" in the electronic converter is very clear in this case.

the wind turbine.

DC/AC power converters can be classified into current source converters and voltage source converters (VSCs). The latter are, by far, more common in power systems since their operation principles and control are simpler. VSCs cannot produce ideal sinusoidal output voltages and their output contain harmonics (fortunately far from the fundamental frequency) which must be filtered out using passive filters at the point of connection with the grid. In this regard, the simplest solution is to add an inductor in series with the converter (L-filter). If required, an additional capacitor can be added in parallel to form an LC filter. The LC filter is a common option when VSCs are used to feed loads with a controlled output voltage (acting as a uninterruptible power supply, for example) [26]. However, for the injection of active and reactive power to electricity grids, the most common option is to add an additional inductor in series (often a transformer), to have an LCL filter. Both LC and LCL filters generate resonances. Therefore, these filters should be designed carefully so they do not interact with the pulse-width modulation nor with the internal controllers of the converters [4]. In some cases, additional damping elements are used (e.g., resistors) while in some other cases the resonances are damped by using dedicated control systems [39].

2.2 Control of VSCs

VSCs require specific controllers to regulate electrical variables (currents and voltages). In general, different voltage and current controllers with sufficient bandwidth separation are applied in a cascaded structure. The number and type of controllers depend on the specific application and will be explained in the following sections.

2.2.1 Grid-Forming and Grid-Following Control Strategies

Traditionally, VSCs were connected to stiff grids. In this case, the most common option is to use a current controller that regulates the active and reactive power injected to the grid, indirectly, by orientating the converter output current with respect to the voltage at the point of common coupling (PCC). For this purpose, a synchronisation algorithm that estimates the grid voltage angle is required. This control strategy is know as grid-following (GFL) since the converter "follows" the voltage imposed by an existing grid. If required, GFL converters could provide ancillary services to the grid by injecting specific profiles of active and reactive power, or by using additional control loops.

Current controllers and synchronisation algorithms of GFL converters provide adequate results in stiff grids. However, there are cases in which the voltage at the connection point is not fixed, such as in isolated power systems and when converters are used as back-up systems. In these cases, VSCs have to form (or help form, at least)

the grid, and therefore voltage and frequency should be actively regulated by them. Converters that help in forming power networks are commonly known as grid-forming (GFM) converters.

GFM converters are generally controlled by using an internal current controller that regulates the current through the converter-side inductance plus an external voltage controller that regulates the voltage across the filter capacitor (see Fig. 2.1). Nonetheless, there are other GFM control strategies that avoid the need of internal controllers [40].

In GFM converters, frequency and voltage set points are generated internally. This means that there is no need to use synchronisation algorithms such as PLLs [2], although some form of synchronisation is needed when the converter is first connected to the grid or when a large disturbance momentarily forces the converter out of synchronism. In general, power injection is controlled with a control loop that resembles the swing equation of synchronous generators (SGs) while reactive power is controlled with a voltage regulator that resembles an automatic voltage regulator (AVR) [3]. Additionally, a virtual impedance loop is sometimes used to simplify the operation of converters in parallel configuration (e.g., connected to the grid or forming a MG) [41]. In some cases, virtual impedance and the power controller are formulated as a single control algorithm.

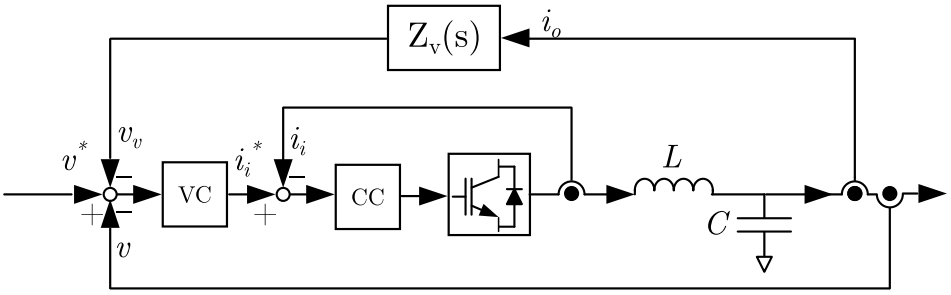

Figure 2.1: Electrical and control diagram of a GFM converter with internal current and voltage controllers, and a virtual impedance loop.

2.2.2 Three-Phase Transformations

Due to the sinusoidal shape of current and voltages in AC systems, different transformations are used to simplify their analysis and control. In particular, Clarke transformation is used to represent three-phase magnitudes in a stationary reference frame by means of the $\alpha\beta 0$ components [4]. For three-wire systems, the 0 component of currents is zero and therefore hardware elements can be represented just by the $\alpha\beta$ components [26]. This simplifies the implementation of controllers since only two (and not three) controllers are required to control an electrical variable. Moreover, $\alpha\beta$ dynamics are decoupled and this simplifies the implementation of the control system. The

main disadvantage of this approach is that electrical variables are still sinusoidal and resonant controllers are required to achieve zero error in steady state [26]. To avoid these issues, variables in an $\alpha\beta$ reference frame can be transformed to a synchronous reference frame (SRF) (dq) by means of Park transformation [4, 26]. In a dq reference frame, electrical variables are seen as constant values in steady state, and then simple proportional-integral (PI) controllers can be used [26]. For this reason, a dq reference frame is very common for controlling three-phase VSCs. In this application d and q dynamics are coupled but an effective decoupling can be provided easily. Moreover, adq reference frame has been traditionally used for analysing power systems as it simplifies many tasks [42].

2.2.3 Control Loops for VSCs

Internal Control Loops for GFM and GFL Converters

In GFLs converters, a **PLL** is commonly used to estimate the angle of the voltage at the connection point and the grid frequency. The simplest PLLs consists of a phase detector, a filter and a voltage controlled oscillator [43]. It is commonly implemented as a closed loop system that transforms the grid voltage (in abc) into a signal referred to a dq reference frame using an estimated angle for that frame. A PI controller is then fed with one of the voltage components (typically the q-axis one) to force it to zero by tuning the estimated grid frequency, which is integrated to estimate a new position for the reference frame. The rest of electrical variables are then transformed, with the estimated angle, to the SRF and are placed relatively to the grid voltage space vector.

Simple PLLs perform well in balanced, strong grids that are not distorted. On the contrary, when harmonics and other higher frequency disturbances are expected, or when the actions of power converter are likely to produce important voltage variations at the PCC, more advanced synchronisation algorithms must be used [43]. For example, the use of quadrature signals and adaptive filters to estimate the positive sequence of the grid voltage improves the performance of PLLs. One of these filters is called dual second order generalized integrator (DSOGI), and it is commonly used in the literature and in industrial applications [4].

Current controllers are essential pieces of the control system of VSCs. They calculate the reference voltage for the VSC (i.e., the duty cycle in PWM control) according to the current error [4]. For example, in GFL converters, the current set point components are calculated to achieve specific values of active and reactive power injection. For simplicity, it is often assumed that the grid voltage magnitude is constant, but this task is carried out efficiently only if the PLL is correctly aligned with either the d or the q-axis voltage of the grid [26]. In all cases, current controllers protect VSCs in case of overcurrents and voltage dips [4].

For many renewable generators, a large DC capacitor is used in the DC side of the

DC/AC electronic interface. The voltage of this DC capacitor should be maintained constant by using a controller that actively modifies the power set point of the grid-connected converter. The use of a **DC-voltage controller** implies that the power set point of the converter cannot be set freely (it is imposed by the amount of active power injected to the DC-link by the primary energy source). Conversely, the reactive power reference can be set to any value provided the limits of the converter are not surpassed [26]. In some scenarios like in MGs, weak grids and back-up systems, converters should also be in charge of regulating the voltage. In these cases, an additional **AC-voltage controller** is implemented on top of the current controller. An inner current controller regulates the current through the converter-side inductance (quickly) while the outer voltage controller regulates the output voltage of the AC capacitor. As the controllers are connected in cascade configuration, the voltage controller must be sufficiently slower than the current controller to prevent interferences between them. Voltage controllers that help in regulating grid voltages can be implemented in GFL converters. However, these controllers in GFL converters do not allow to form the grid, unlike in the case of GFM converters.

The **virtual impedance** is another control loop and is generally implemented on top of the voltage controller to facilitate the operation of VSCs in parallel configuration. It modifies the voltage controller set point by emulating the voltage droop across an impedance (see Fig. 2.1). As the virtual impedance is the loop that controls the electrical variable that is closer to the grid (the output current) it is commonly used to address many issues, such as improving the system stability, improve power quality, manage the power sharing between units or improve the fault ride-through capability [16].

Frequency Control and Power Sharing in GFM Converters

GFM converters have a control system that resembles the operation of SGs. In the literature, there are different options to control GFM converters. The most representative ones are explained in the following lines.

- The most extended (and simplest) GFM power control strategy is called droop control [14, 44]. Droop controllers emulate the static operation of SGs. The traditional droop control is written as follows:

$$\omega_i = \omega_{ni} - m_i P_i, \tag{2.1}$$

$$V_i = V_{ni} - n_i Q_i, \tag{2.2}$$

  where ω_i and V_i are the output frequency and voltage of the ith converter, ω_{ni} and V_{ni} are the no-load voltage and frequency and m_i and n_i are the droop coefficients of the ith converter. Droop controllers usually include a low-pass filter (LPF) to avoid fast transients in the frequency set point and filter noise out in power

measurments [14]. The application of droop controllers allows sharing active and reactive power demand among the devices that are forming the grid. In particular, the droop coefficients determine the specific power-sharing ratio. Notice that droop controllers (as other controllers with droop characteristic) introduce voltage and frequency deviations, in steady state. These deviations are defined by (2.1) and (2.2) and should be corrected by additional secondary or tertiary controllers.

- Another option to control active and reactive power with GFM converters is to emulate the dynamic characteristics of SGs [17, 22]. The first solution known in this regard was called virtual synchronous machine [2] (VISMA) and it included a seventh order model that mimicked the internal dynamics of a SG [2]. Nowadays, the most extended solution consists of a second-order model that only mimics a swing equation with an ideal fast governor plus a reactive power controller. Compared to droop, the characteristic of the frequency droop in (2.1) is substituted by the swing equation in (2.3), while the characteristic of the voltage droop commonly remains unaltered:

$$\frac{d\omega_{i,pu}}{dt} \approx \frac{p_0}{T_a} - \frac{p_e}{T_a} - \frac{k_d}{T_a}(\omega_{i,pu} - \omega_{g,pu}), \tag{2.3}$$

  where $\omega_{i,pu}$ is the output frequency (in pu) of the converter, $\omega_{g,pu}$ is the frequency of the grid , p_0 is the active power initially delivered by the converter, p_e is the current electrical output power of the converter, and T_a and k_d are related to the inertia and damping factor of the emulated machine. Swing equation and reactive power controllers generate the set points for either the modulation stage or the internal controllers (voltage and/or current). The first solution is commonly known as synchronverter. It is simpler compared to the second one, but it does not provide over-current protection in its basic form and does not take into account the output filter behaviour [19]. The second solution is commonly known as virtual synchronous machine [3] (VSM), it provides current limitation and closed-loop control of the filter output voltage. However, inner controllers must be carefully designed to avoid mutual interactions [3, 45]. Due to safety reasons, VSMs are far more common in practical applications. The small-signal response of a frequency droop controller with a first-order LPF and a VSM based on a second-order model are equivalent [22]:

$$T_a = \frac{1}{m_p \omega_c},\ k_d = \frac{1}{m_p}, \tag{2.4}$$

  where ω_c is the cutoff frequency of the LPF used in the droop controller.

- Some authors have proposed to match the electromechanical dynamics of SGs with those of power converters by using the so-called matching control [18, 20] which takes advantage of the electrical resemblance between SGs and LC filters.

Then, an oscillator linked to the DC voltage generates the frequency and voltage references. In this way, both voltage magnitude and frequency are controlled. This controller offers GFM characteristics, power sharing and inertia emulation. Compared to droop and VSM, it does not include internal controllers. This avoids interactions between control loops but the VSC is not protected against overcurrents. Matching control is relatively new and, therefore, more work must be done in several aspects (e.g., interaction between devices, fulfilment of grid codes, etc.).

- Recently, a GFM control technique called virtual oscillator control (VOC) has gained the attention of researchers [21]. Compared to other control techniques, it has faster dynamics [23] and has better performance than others in case of large disturbances. However, under certain grid conditions and for small variations of the operating conditions, VOC and droop control present similar dynamics. VOC features a fast synchronisation, provides power sharing among units and can track power set points [46]. In order to provide inertia, additional loops must be added to the original VOC [46]. VOC has promising features. However, it generates low-frequency harmonics in the output signals, which is a serious drawback compared to other alternatives [21, 47].

2.3 Microgrids as Aggregations of Converters

MGs were initially proposed as a solution to supply remote loads with local resources. When operated in islanded mode, it is essential to have at least one GFM device that regulates the MG voltage and frequency. Traditionally, diesel generators were used as GFM devices, but nowadays batteries and renewable generation are taking that role. Indeed, GFM converters are mostly studied for their application in MGs. MGs can also be regarded as aggregations of GFM, GFL converters, and loads. Although they were firstly proposed to be operated in islanded mode, they can also be operated connected to the main grid. In the latter case, they can provide a variety of ancillary services due to their flexible control system. MGs can be operated as aggregations of distributed generators easing the penetration of small distributed resources in power systems [48, 49].

MGs are usually controlled with a hierarchy consisting of four control layers. The zero control layer is applied locally and consists of internal control loops that regulate currents and voltages. Current controllers, DC and AC-voltage controllers, synchronisation algorithm (i.e., PLL) and the virtual impedance loop described above are included in this layer. These controllers are the fastest ones and, sometimes, are considered part of the primary control layer. The primary control layer determines the power sharing among units. Droop, VSM, VISMA, synchronverter, matching control and VOC are examples of primary controllers.

In MGs, the set points for the primary control are set by the secondary control layer. The secondary control restores voltage and frequency to their nominal values and coordinates the operation of the devices that form the MG. In addition, in grid-connected mode, the secondary control coordinates the distributed resources so the energy exchanged with the main grid follows the set points sent by the tertiary control layer. Secondary control is also responsible for the coordination of resources to achieve seamless transitions between operating modes, mainly, the synchronisation of the MG with the external grid. Secondary controllers are explained in detail in the following sections.

Tertiary control sets the set points for secondary controllers. In this control layer, techo-economical optimizations are run to establish the system unit commitment. This control is out of the scope of this thesis and is not detailed here [1, 12].

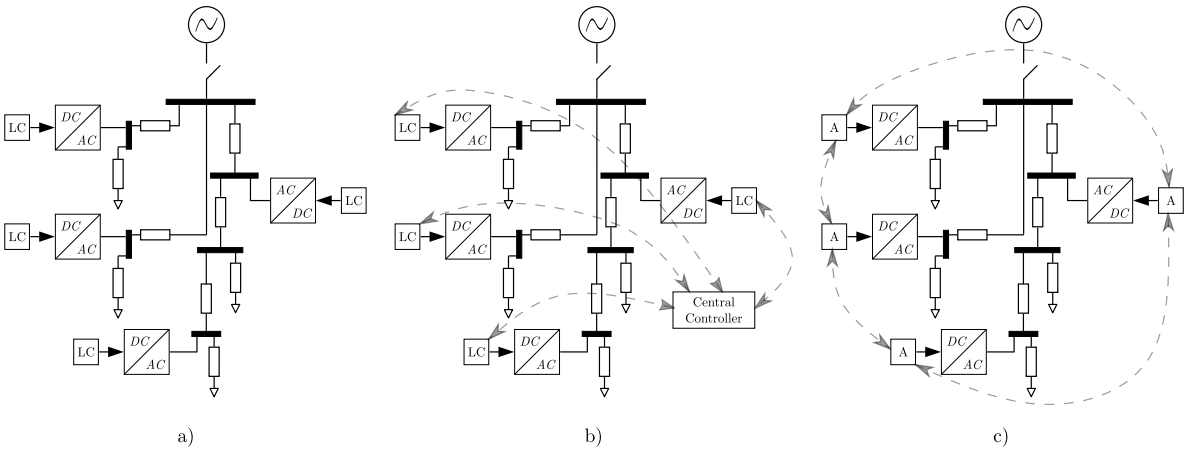

Figure 2.2: Topologies of MGs. LC means local controller and A means agent. (a) Decentralised, (b) centralised and (c) distributed or multi-agent [1].

In addition to the hierarchical division of MG controllers, they can also be classified according to the way they are implemented in MGs. Fig. 2.2 shows the most common classification: centralised, decentralised or local, and distributed. Primary controllers are commonly implemented in a decentralised way while centralised and distributed alternatives are preferred for secondary and tertiary controllers [1, 14, 33]. In decentralised control, local controllers act according to local information without exchanging information with other controllers. The main advantage of decentralised controllers is their high reliability since they have small dependence on communications. In the centralised approach, a single controller gathers the information from local devices in real time. Then, according to a control law, it sends back the set points for lower control levels. Centralised control allows the coordination of all devices in the MG and optimal utilization of resources [50, 51]. The main drawback of this control strategy is its high dependence on communication links [52]. Distributed control is implemented

with multi-agent (MA) technologies, where the local controllers (called agents) share information with neighboring agents and act locally [53]. This communication topology allows the implementation of a coordinated control between units and also to perform economic and energy optimization. Compared to centralised controller, the dependency on communications is smaller. This classification is used in the following section to explore the state-of-the-art of secondary control in MGs.

2.4 Secondary Control of Microgrids

The main objective of secondary control is the coordination of MG devices in grid-connected and islanded modes, and during the transitions between these two modes: synchronisation and islanding. In grid-connected mode, secondary control drives converters to the unit commitments calculated by the tertiary control so that the aggregated response of the MG meets the grid operator's requirements. In islanded mode, this control coordinates the devices that form the MG to compensate voltage and frequency deviations from their nominal values induced by primary controllers. Secondary control is also in charge of adjusting the operating points of the units in this operating mode according to tertiary control commands. Additionally, secondary control ensures that the transition between operating modes is seamless and does not produce undesired transients. Moreover, when energy storage systems (ESSs) are involved, specially batteries, secondary controllers will also look after state of charge (SOC) balancing. In order to accomplish these tasks, secondary control may have to introduce slight variations on primary controllers.

2.4.1 Decentralised Secondary Control

Although decentralised secondary control of MGs is not the most common alternative, some examples can be found in the literature. Voltage and frequency restoration to their nominal values can be done using decentralise secondary control but centralised or distributed solutions are preferred for device coordination.

One of the approaches to restore voltage and frequency to their nominal values in a MG in a decentralised way is the use of wash-out filters in primary controllers [54–56]. Wash-out filters have zero steady-state gain, i.e., the frequency and voltage of the MG come back to their original values after disturbances. In the literature, it has been proved that a secondary controller based on a PI controller is equivalent to primary controllers with wash-out filters [54]. Other filters and controllers can be implemented in addition to the standard droop control to compensate frequency deviations [57, 58]. In [57], it is shown that a PI controller can be used to modify converter droops. In this case, frequency and voltage drifts in steady-state are avoided, and droop parameters are optimised by using a quadratic cost function. Similarly, in [58], a PI controller is applied

to modify the output signal of the droop, with the same purpose. However, since there is not communication between units, power sharing during transients may be inadequate. To avoid this issue, secondary controllers must be designed carefully. However, this may result in a slow restoration process. Predictive control and other control options based on estimators have also been proposed as decentralised secondary controllers [59–61]. In [59], a model predictive controller substitutes conventional inner control loops and droop to maintain constant voltage in a DC MG. Some authors use models to estimate voltages across the MG and set the set-point values for droop controllers [60, 62]. For example, in [60], a large-signal model of a MG is used to predict the operating point of each unit and achieve the required reactive-power sharing. Meanwhile, a small-signal model is used in [62] to implement a model predictive controller. The main drawback of model-based estimators is that models for all parts of the MG are not always available and, consequently, robustness against parameter and topology variations is often difficult to achieve.

In MGs with battery energy storage systems (BESSs), a common approach is to balance the SOC. This prevents BESSs with lower capacity from discharging frequently, reducing the degradation of those devices. In decentralised secondary controllers, two different types of adaptive droops are proposed to address this objective (see Fig. 2.3) [63]:

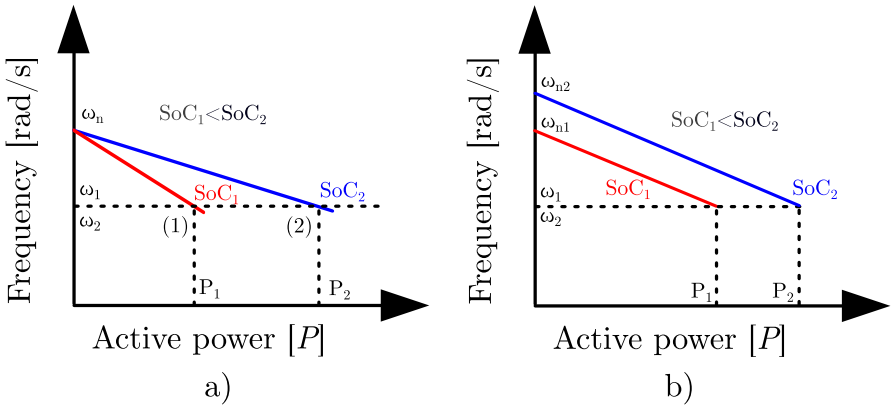

Figure 2.3: Modifications of droop controllers according to SOC levels.

1. In the case of Fig. 2.3 (a), the droop characteristic m_p is adjusted according to the SOC of each unit [63–67]. Droop constants are set to be proportional to SOC_i^n for the charging process and inversely proportional in the discharging process. During discharging, this method forces ESSs with higher SOC to inject more power into the grid. While charging, ESSs with lower SOC absorb more power. The value of the exponent n is chosen to adjust the speed required to achieve SOC balance. The technique depicted in Fig. 2.3 (a) must be applied carefully in low-voltage

systems, where droop constants must be kept small to limit voltage and frequency deviations.

2. Alternatively (see Fig. 2.3 (b)) droop lines can be shifted up and down according to the SOC of each unit [67,68]. A droop line is lowered when the unit SOC is low, forcing all other units to inject more power and, eventually, charge the battery, and vice-versa.

Additionally, several solutions that rely on a set of rules have been proposed to provide decentralised coordination in a MGs with BESSs [67,69]. However, these proposals are designed for a specific MG topology and their application to general cases is limited.

From the point of view of stability, controllers that follow a strategy similar to that presented in Fig. 2.3 (b) are preferred. In this way MG parameters are not changed and, consequently, the small-signal stability characteristics of the grid are preserved [70]. Indeed, this philosophy is the one followed by decentralised secondary controllers for voltage and frequency restoration presented before [54–58].

Decentralised secondary controllers, due to their small dependence on communication systems, are suitable for MGs sensitive to communication failures or cyber-attacks. However, to avoid undesired variations in the power sharing, coordination among MG devices in a centralised or distributed way is preferred to a decentralised approach.

2.4.2 Centralised Secondary Control

Centralised secondary control in MGs is based on a central controller that communicates with each of the distributed devices and defines their set points based on a control law. This approach allows full utilization of the resources of the MG because the central controller has access to all the states of the grid. However, any communication loss may affect the stability of the MG [52]. Secondary central controllers have been successfully implemented to restore voltage and frequency levels [14,71,72], to enhance power quality by harmonic cancellation [73, 74] and voltage unbalance compensation [75], to perform active and reactive power sharing [74, 76], to coordinate transitions between operation modes [66], and to balance SOC if ESSs are involved.

PI controllers have been widely use as centralised secondary controllers to restore frequency and voltage and enhance power quality [14, 66, 73, 75, 76]. This approach is rather simple but cannot take into account the techno-economic characteristics of the individual units, which can only be taken into account by solving optimization problems with constraints [51, 71].

Advanced techniques such as fuzzy logic and artificial neural networks are sometimes applied in centralised secondary controllers [77, 78]. The outcomes of these control laws, as in decentralised secondary control, may determine the set points for primary

controllers as in Fig. 2.3 (b) or the values of certain primary-controller parameters such as droop constants (Fig. 2.3 (a)) or virtual impedances [76, 79, 80].

In [66], a secondary controller coordinates the operation of a MG and prevents uneven discharge of ESSs during islanded operation. Droop coefficients of each unit are set to be inversely proportional to their SOCs. This SOC balancing control strategy may lead to large frequency deviations for low levels of SOC and, therefore, the controller limits should be adjusted properly.

Some centralised secondary controllers adjust the value of virtual impedances to improve power sharing and unit coordination [50, 76, 81]. As with droops, this method produces voltage and frequency deviations that should be corrected.

2.4.3 Distributed Secondary Control

Distributed secondary control is implemented with the MA technology. Agents are autonomous control units that are implemented locally in different devices such as distributed generators, storage devices, loads, switches, etc. They interchange information with neighbouring agents and, by following different rules, calculate commands for lower control levels [53]. This control strategy allows the deployment of a coordinated control among units, and economic and energy optimizations are viable. Since agents are autonomous, a central controller is not needed. This avoids instabilities caused by small-scale communication failures [1]. Compared to centralised controller, the dependence on communications is smaller.

Cooperative and competitive distributed controllers can be found in the literature [1]. The objective of cooperative control is to reach a steady state point where the states of the units tend to the same value, namely, the consensus value [53, 82]. On the other hand, competitive control is applied when agents have different objectives.

Most MA control strategies applied to secondary control require additional terms in the droop control [33]:

$$\begin{aligned} \omega_i &= \omega_n - m_{pi} P_i + \delta u_{\omega,i}, \\ V_i &= V_n - n_{qi} Q_i + \delta u_{v,i}, \end{aligned} \tag{2.5}$$

which is equivalent to Fig. 2.3 (b). There are some instances where other parameters such as virtual impedances or droop constants are adjusted by means of MA [83]. These parameters can be calculated in many different ways: average-based [84], consensus-based [83, 85, 86] or solving cooperative-tracker problems [1, 86, 86].

The main objectives of distributed secondary controllers in AC MGs are the restoration of the frequency and voltage levels [85], appropriate active and reactive power sharing and SOC balancing, if there are ESSs [84].

MA control has a clear advantage over centralised control regarding robustness in the case of communication failures. However, distributed control also presents disadvantages, mainly due to the sparse communications. The convergence of consensus algo-

rithms depends on the distribution of the agents and the communication links between them [53]. When designing this type of controllers, it is convenient to perform convergence studies to asses their suitability [83, 87]. Additionally, reference [88] presents an algorithm to select the location of agents and achieve optimum controllability.

2.5 Interactions between Converters and SGs

PLLs have been widely used in conventional power systems where electronic converters were most often (if not always) connected inGFL mode. A control system based on a PLL works properly in strong grids and when the network dynamics are relatively slow [26]. Nevertheless, it has been demonstrated that the PLL design of a GFL converter has a strong influence on the stability of grid-tied converters and the network as a whole. Instabilities of GFL converters sometimes come from a negative value of the *dq* impedance model, which is related to the PLL bandwidth and the power levels injected to the grid [89]. Indeed, it has been found that power transfer in high-voltage DC interconnections is limited as PLLs used become faster [90]. The interaction between the PLL and DC-voltage controller can also have a negative effect on the stability of grid-connected converters that operate as rectifiers [91]. Some recommendations for the design of current controllers, PLLs and DC-voltage controllers for grid-connected converters were presented in [91].

The behaviour of PLLs in grids with low inertia and high penetration of renewable generation, such as in a typical MG, has not been addressed in detail in the literature. Interactions between PLLs and SGs have been previously studied in the literature [27, 92–95]. Katiraei *et al.* [92, 93] corroborate that the power injected by GFL converters, as well as their current controllers and PLLs, have a relevant influence in the MG stability. By using eigenvalue analysis, it was found that the AVR, the excitation and the generator inertia affect the stability of MGs with SGs and GFL converters [27]. The interaction between loading conditions and PLL design was studied in [95]. Results showed that loading conditions and the design of the PLL have influence over the same eigenvalues. Therefore, loading conditions should also be considered in the design of PLLs.

The stability of a MG consisting of droop controlled converters and a controllable load (interfaced by a series-shunt converter that uses PLL) was studied in [96]. That work found that the PLL has a small contribution to the oscillatory modes, which mainly depend on the droop parameters. In addition, interactions between the DC-voltage controller and other controllers of VSCs were studied in [97, 98]. It was found that these interactions are more pronounced in weak grids. In particular, it was found that the stability margins are reduced when the DC-voltage controller and PLLs have similar bandwidths.

Interactions of PLLs with current controllers and DC-voltage controllers have been

studied in conventional grids and in MGs [89–91]. However, interactions between different control loops and the rest of elements present in a MG (AVR, excitation, droops, and voltage and current controllers of GFM converter, etc.) have not been studied in detail. Furthermore, in the case of MGs, there are no clear guidelines to design the controllers of GFM converters, such as those that already existing for GFL converters.

Models used to describe SGs in MGs are diverse. For example, in some references damping windings are neglected [27, 42] while they are considered in others [92, 93]. In addition, small-signal models of such hybrid and diverse MGs have been rarely validated experimentally [93].

Dynamic interactions caused by PLLs in MGs (formed by either diesel gen-sets or droop-controlled converters) are studied in Chapter 3 and a design methodology is proposed to assist the designer in choosing the control parameters in MGs comprised of GFM and GFL devices.

2.6 Design of primary controllers and frequency control

MGs and other aggregations of generators such as virtual power plants (VPPs) commonly consist of a heterogeneous mixture of GFM and GFL converters and can, therefore, provide a wide palette of grid services. In the field of inertial services, contributions have focused on the design of GFM controllers and the provision of adequate inertial responses. For example, several authors have proposed the use of dedicated storage devices with a control scheme that emulates some of the characteristics of SGs [99]. By using this solution the response can be flexibly adjusted. However, the need of a dedicated storage device increases the cost and reduces the feasibility of the solution.

Regarding the provision of frequency-support services without storage, the coordination of generating units using a secondary controller was proposed in [100]. However, inertial services must be relatively fast and the response time of centralised controllers usually limits the feasibility of this option. To avoid these limitations, some researchers have proposed methodologies for designing primary controllers in a group of converters (inherently faster than secondary controllers), such as droops and VSMs, so that they operate as a single device with a customised inertial response [101–105].

For example, in [101], the parameters of several VSMs in a MG are calculated using particle swarm optimization to provide inertial response and guarantee frequency stability against disturbances. In the MG presented in [102], the VSM parameters are adjusted, for the same purposes, by using a linear quadratic regulator based on the actual frequency of the grid. In [104, 105], analytical aggregated models of VSMs are developed and, taking into account these models, VSM parameters are adjusted so the aggregated response of all units has specific inertial characteristics.

These references focus on external primary controllers (e.g., VSMs), while inner control loops such as virtual impedance and voltage control are only sometimes taken into consideration. In fact, current control loops are very often neglected [104]. Still, only a few authors have studied the coordinated design of droop controllers in MGs to adjust their inertial response. For example, in [106], the primary controllers of a MG are adjusted, by solving an optimization problem, to have an aggregated droop characteristic.

On the one hand, analytical design methods give a better insight into the impact of parameters on frequency dynamics, however, the operation of each device must be fully understood before the design can be addressed. On the other hand, optimization tools do not require detailed analytical models and, therefore, they are simpler to use with a variety of devices. Unfortunately, these methods do not provide clear information about the relationship between control parameters and frequency dynamics.

When the operating conditions change, MG controller parameters may have to be reconfigured to meet frequency specifications [102, 107]. Examples of when controllers need to be redesigned are: after a generator is connected/disconnected, when power sharing among units must be changed or when battery droop characteristics are adjusted according to battery SOC [68]. Sensitivity analysis has often been used for adjusting converter controllers and to study their influence on system eigenvalues (and, therefore, on system stability) [70]. Some authors have designed controllers by taking into account only one eigenvalue, and using parametric sensitivity. This has been done by using one [108] or the two [109] components of the sensitivity. The movement of several eigenvalues based on sensitivity analysis has been addressed in [110], in controllers for conventional synchronous generators, and in [111], in a multi-terminal HVDC system embedded into a bulk power system.

A methodology to redesign primary controllers of GFM units to shape the frequency response of a MG is presented in Chapter 4. The proposed methodology uses common small-signal tools such as eigenvalue and participation factor analyses and parametric sensitivity for the relocation of several eigenvalues simultaneously.

2.7 Design of Secondary Controllers

One of the drawbacks of hierarchical and cascaded control is that the operation of MGs may be severely slowed down due to the bandwidth separation between controllers. This is specially important in secondary controllers. Traditional secondary controllers consist of a centralised controller, inherently slower than primary controllers, that restores voltage and frequency to their nominal values [14]. Secondary control speed is limited by the possible interaction of control layers and the limitations imposed by communication delays. Compared to centralised controllers, distributed secondary control presents small dependence on communications, but still its speed is limited by commu-

nications [82]. In particular, references such as [34, 112–114] show that communication delays play an important role in the stability of MGs, especially when the bandwidth of controllers increases.

In [115], the impact of time-invariant communication delays on the secondary control of islanded MGs is studied and linked to the design criteria. However, in most MG applications communication delays are not time invariant and stochastic models are required to represent them accurately [116]. Some authors have already considered communication delays when designing secondary controllers to guarantee stability [34, 117]. For example, in [34], a predictive model is used to mitigate the effects of communication delays, which, in turn, also allows speeding up the secondary control. Additionally, several more approaches have been presented to achieve faster secondary controllers [34, 117–119]. A common approach is to use model predictive primary controllers, faster than traditional controllers [119]. Then secondary controller is implemented on top following the traditional bandwidth separation criteria [118]. Model predictive control has also been applied to secondary controllers, achieving fast transient responses and robustness against communication uncertainties [120].

Although fast secondary controllers have already been proposed in the literature, the nature of the interactions between primary and secondary controllers has not been addressed yet. Moreover, the influence of communication time delays on the design of centralised secondary controllers has not been studied sufficiently, either [121]. In Chapter 5 of this thesis, the interactions between primary and secondary controllers and the influence of communication delays on the design of secondary controllers are studied.

2.8 Coordination of Devices for Synchronising MGs

MG synchronisation consists in reducing the difference in voltage magnitude and phase between both sides of the PCC, namely, the main grid and the MG. The most extended approach is to coordinate GFM units to modify frequency and voltage [122–124]. The rather simple case where all GFM units are connected to the PCC has been studied in detail [122]. Controllers that can synchronise devices regardless the MG topology have also been proposed in the literature [124].

For angle synchronisation, a common approach is to adjust the frequency of the GFM converters to be as close as possible to the ideal frequency of the MG [125]. Then, the MG is connected when the phase difference between the two sides of the PCC is sufficiently small. This approach may be slow and cause undesired transients. Therefore, it is not suitable for large MGs where small angle differences at the connection point may cause large oscillations. Other authors have proposed to reduce the angle mismatch by changing the frequency of GFM converters until the phase difference is zero [126]. While the first solution focuses on matching the frequency, the second

one directly addresses the angle difference, avoiding unwanted oscillations. The most common approach in this respect is to use consensus algorithms to adjust the frequency of each device [124,127]. Since power constraints are not always included, this approach may result in "uneven" power sharing during transitions.

When it comes to voltage magnitude synchronisation, if consensus algorithms are used, the voltage level of the considered nodes is controlled to converge to the voltage of the grid PCC. This is suitable if all GFM units are connected to the PCC, but it leads to voltage differences between both sides of the PCC if GFM units are distributed across the MG. When the voltage at the connection point is monitored and a PI controller is used to reduce the voltage difference, the problem just mentioned disappears [126]. Solutions that monitor the voltage at both sides of the PCC and use a PI controller commonly generate a signal that modifies the output of droop controllers, as indicated in Fig. 2.3 (b). As in phase synchronisation, power constraints are are often ignored and power-sharing ratios and operating points may change during transitions [127].

Changes in the operating points should be avoided in units operating at their optimal power points. This can be done by tuning power sharing among converters. Power sharing in droop dominated MGs has been widely studied in the literature [128, 129]. Typically, traditional droops ($P-f$, $Q-V$) are used in inductive grids [66] while $Q-f$, $P-V$ droops or traditional droops with virtual impedances are implemented in resistive grids [130]. In both cases, droop gradients are adjusted to achieve a specific power sharing in steady state and after unplanned operations [66]. The selection of droop gradients may be based on generator ratings, economical dispatching or SOC of storage units [66]. For example, when BESSs are involved, droop gradients are commonly chosen to be inversely proportional to the SOC [63, 66].

Secondary control usually alters the operating point of GFM units during synchronisation, islanding, voltage and frequency restoration, and connection and disconnection of devices [131]. Batteries are often used in MGs to enable smooth transition between operating modes [132]. In these scenarios, batteries (or selected GFM units) can be used to absorb/inject the necessary energy and allow GFM units to maintain their operating points. Nevertheless, this aspect has not been studied in detail in the literature [133].

In Chapter 6 of this thesis, a secondary controller that coordinates batteries and distributed energy resources (DERs) in MGs is presented. The proposed secondary controller modifies droop controllers to maintain the operating point of certain GFM units and allow batteries to inject/absorb the necessary energy to ensure a seamless synchronisation of the MG.

2.9 Chapter Summary

The state of the art of GFM and GFL converters in MGs has been presented in this chapter. In this review, the following research gaps have been found:

- Although PLLs have been extensively studied for the use in conventional power systems, the possible interactions with GFM devices in MGs and low inertia power grids has not been addressed in detail. The design of PLLs with the aim of avoiding interactions with other primary controllers in MGs is studied in Chapter 3.

- Similarly to conventional generation, aggregations of distributed resources can provide frequency support. However, the solutions proposed in the literature to provide frequency support by means of several GFM units are not general enough or ignore operating limitations. A methodology to design primary controllers of a MG and preserve its frequency dynamics when the operating conditions change is presented in Chapter 4.

- The extent to which bandwidth of primary controllers and communication delays limit the design of secondary controllers must be investigated further. This aspect is addressed in Chapter 5.

- During transitions, GFM units share the power demand according to their droop laws. However, in some cases, this results in unwanted changes in their operating point. A secondary controller that coordinates the energy injected by BESSs to ensure seamless transitions and avoids changes in the operating point is presented in Chapter 6.

Chapter 3

Modelling and Analysis of Electronic Power Converters in Microgrids

This chapter addresses the modelling and analysis of microgrids (MGs) based on synchronous generators (SGs) and voltage source converters (VSCs), with special emphasis on the impact on the phase-locked loop (PLL) dynamics. This chapter is organised as follows. MG topologies are described in Section 3.1. Section 3.2 presents the small-signal models for each of the elements of the MG. Section 3.3 is focused on the interactions between the PLL and other MG controllers using eigenvalues and participation factors. A design guide for primary controllers is developed in Section 3.4 while experimental results are presented in Section 3.5. Laboratory results are discussed in Section 3.6, including the impact of additional control loops and advanced synchronisation algorithms like dual second order generalized integrator (DSOGI). Conclusions are drawn in Section 3.7.

3.1 Application Overview

The interactions between PLLs and grid-forming (GFM) devices are studied in a MG that can be formed by either a diesel generator or a droop-based converter. In this section, the MG studied in this chapter is described.

3.1.1 System Description

Fig. 3.1 shows the MG studied in this chapter. It consist on a GFM device and a grid-following (GFL) converter that feed a resistive-inductive load. For simplicity, all of them are connected to the point of common coupling (PCC).

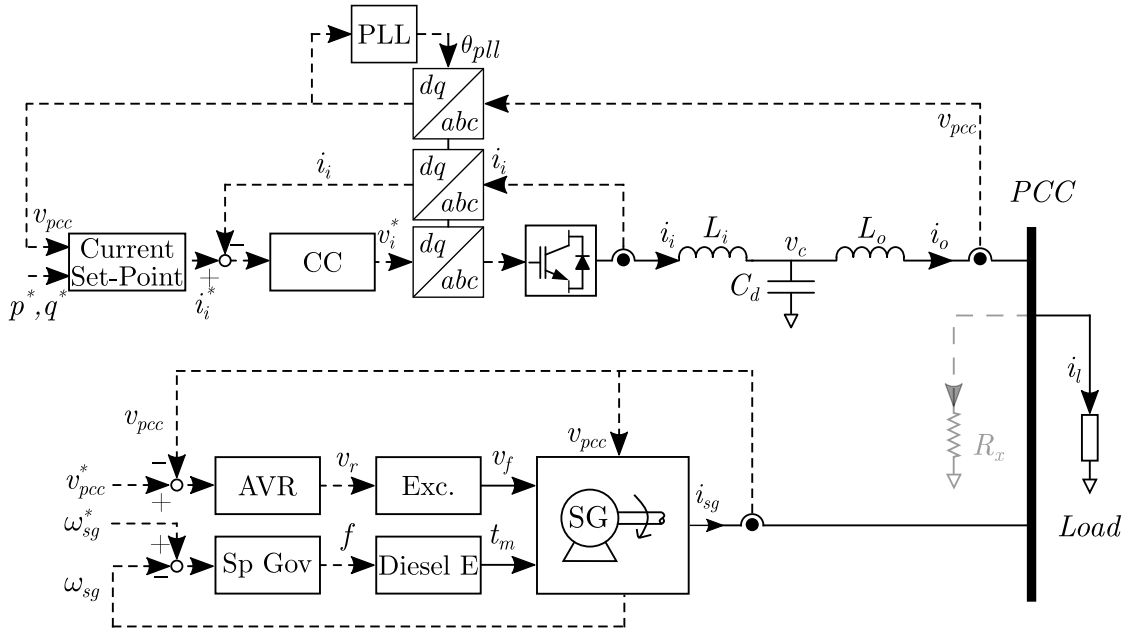

Figure 3.1: Electrical and control diagram of a diesel gen-set and a GFL converter connected to a common bus.

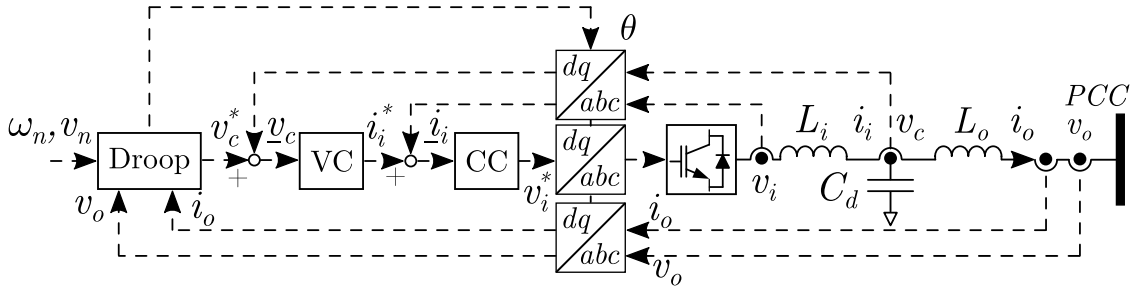

Figure 3.2: Electrical and control diagram of a GFM converter.

Fig. 3.1 shows the diagram of the MG when the SG (at the bottom) forms the grid. A diagram of the GFM converter is presented in Fig. 3.2. This MG topology may be used for energy supply of remote residential or industrial areas [11,13], although here it is used as a simplified test system to understand the interactions between the different MG elements. In the rest of this chapter, MG1 refers to the MG formed by a SG while MG2 refers to to the MG formed by a GFM VSC.

The diesel generator includes a diesel engine mechanically coupled to a SG that has its excitation system formed of an alternator and a diode rectifier. The PCC voltage and frequency are controlled by the automatic voltage regulator (AVR) and the speed governor of the SG, respectively. The AVR generates the set point for the excitation system (v_r) while the speed governor generates the set point for the fuel injection (f).

In order for this study to be applicable to larger MGs, and MG power parks, LCL

filters are considered for both GFM and GFL converters. These filters are commonly used to interface GFM converters [70] or to facilitate the parallel operation of GFM converters. Current and voltage loops are used to control the current through the inner inductance and the voltage across the AC capacitor. Voltage and frequency droop controllers are used to define the voltage and frequency of the GFM converter.

The GFL converter is connected to the PCC via an LCL filter. The active and reactive power injections are controlled indirectly by using a current controller implemented in dq. The synchronous reference frame (SRF) is obtained by using a PLL [26].

3.1.2 Reference Frames

The small-signal models of all the elements in the grid have been developed following the methodology presented in [70]. State-space equations are represented in a common reference frame (DQ) synchronised with the output voltage of the GFM device (SG or droop-controlled VSC). An additional reference frame (dq) generated by the PLL is used to model the GFL converter. Variables are transformed between the reference frames by using [70]:

$$\begin{bmatrix} f^D \\ f^Q \end{bmatrix} = \begin{bmatrix} \cos\delta & -\sin\delta \\ \sin\delta & \cos\delta \end{bmatrix} \begin{bmatrix} f^d \\ f^q \end{bmatrix}, \tag{3.1}$$

where δ is the angle of the dq reference frame with respect to the DQ reference frame and f refers to a three-phase voltage or current.

3.2 Small-Signal Modelling of MG Elements

The small-signal models of the diesel generator, the GFM converter and the GFL converter are introduced in this section, while their detailed models are provided in Appendix A.

3.2.1 Small-Signal Model of a Diesel Generator

The gen-set model consists of the equivalent electrical circuit of the SG, the excitation circuit, the prime mover (diesel engine), the controllers mentioned above (voltage and frequency) and a shaft model [42, 93, 134–136]. The SG equations are presented in pu (in SG base) and represent variables in the (DQ) reference frame [42].

Electromechanical Model

The SG is modelled using a set of differential equations with flux linkages as state variables and a set of algebraic equations that link the currents and the flux linkages [42]. A three-wire system has been considered, so $0-$axis equations are omitted [42]. A

laminated salient-pole machine has been considered. Therefore, the small-signal model has five states, $x_\psi = [\psi^D, \psi_f, \psi_k^D, \psi^Q, \psi_k^Q]^T$:

$$\Delta\dot{x}_\psi = A_{EM}\Delta x_\psi + B_{EM1}\left[\Delta v_f\right] + B_{EM2}\left[\Delta v_{sg}^{DQ}\right] + B_{EM3}\left[\Delta\omega_r\right], \tag{3.2}$$

where ψ^{DQ} is the stator flux linkage, ψ_f and ψ_k^{DQ} are the rotor flux linkages, v_f is the generator field voltage, v_{pcc}^{DQ} is PCC voltage in DQ and in this case the generator output voltage in DQ, ω_r is the rotor angular frequency in pu and A_{EM}, B_{EM1}, B_{EM2} and B_{EM3} are calculated analytically according to (A.11) and (A.16) (in Appendix A). The output variables are the electric torque (t_e), the stator currents (i_{sg}^{DQ}) and the field current (i_f). Currents can be calculated from flux linkages using (A.6)−(A.10), while the electric torque is [42]:

$$t_e = i_{sg}^Q\psi^D - i_{sg}^D\psi^Q. \tag{3.3}$$

The linearised expressions for the electric torque and the stator and field currents are:

$$\left[\Delta t_e\right] = C_{EM1}\Delta x_\psi, \tag{3.4}$$

$$\begin{bmatrix}\Delta i_{sg}^D \\ \Delta i_{sg}^Q\end{bmatrix} = C_{EM2}\Delta x_\psi, \quad \left[\Delta i_f\right] = C_{EM3}\Delta x_\psi. \tag{3.5}$$

The analytical expressions for C_{EM1}, C_{EM2} and C_{EM3} are shown in Appendix A, in (A.17)−(A.19).

Motion Equations

The shaft is modelled by using the following differential equation, as in [42]:

$$\frac{d\omega_r}{dt} = \frac{t_m - t_e}{2H}, \tag{3.6}$$

where t_m is the mechanical torque and H is the per unit inertia constant of the SG shaft. This equation is linear and can be rewritten as [42]:

$$\left[\Delta\dot{\omega}_{sg}\right] = B_{S1}\left[\Delta t_m\right] + B_{S2}\left[\Delta t_e\right]. \tag{3.7}$$

Exciter

The exciter includes an alternator in series with a diode rectifier [135]. The model AC5A has been used [137]:

$$\frac{dv_f}{dt} = \frac{1}{T_E}v_r - \frac{S_E + K_E}{T_E}v_f, \tag{3.8}$$

where v_r is the regulated voltage and T_E, S_E and K_E are the time constant, a parameter that models the saturation function and the self-excitation constant of the excitation system respectively. This model can be linearised, yielding:

$$\left[\Delta\dot{v}_f\right] = A_E\left[\Delta v_f\right] + B_{E1}\left[\Delta v_r\right]. \tag{3.9}$$

Engine

The dynamics of the diesel engine used as primer mover is often modelled as follows [134]:

$$\frac{dt_m}{dt} = \frac{1}{\tau_m(\sigma + t_m)}(f - t_m), \tag{3.10}$$

where f is the injected fuel, τ_m is the constant term of the engine time constant and σ is the degree of increased retarding of the engine. The linearised model becomes (details in Appendix A):

$$\left[\Delta \dot{t}_m\right] = A_D \left[\Delta t_m\right] + B_D \left[\Delta f\right]. \tag{3.11}$$

Automatic Voltage Regulator (AVR)

For simplicity, a proportional-integral (PI) controller has been adopted for the AVR [134]. This regulator controls the amplitude of the PCC voltage (v_{sg}), ($v_{sg} = v_{pcc}$) by generating the set point for the regulated voltage (v_r). The module of the PCC voltage is:

$$v_{sg} = \sqrt{{v_{sg}^D}^2 + {v_{sg}^Q}^2}. \tag{3.12}$$

The linearised model of the AVR is (details in Appendix A):

$$\left[\Delta \dot{\alpha}\right] = B_{AVR1} \left[\Delta v_{sg}^*\right] + B_{AVR2} \left[\Delta v_{sg}^{DQ}\right], \tag{3.13}$$

$$\left[\Delta v_r\right] = C_{AVR} \left[\Delta \alpha\right] + D_{AVR1} \left[\Delta v_{sg}^*\right] + D_{AVR2} \left[\Delta v_{sg}^{DQ}\right], \tag{3.14}$$

where α is the state variable of the AVR and v_{sg}^* is the voltage set-point at the PCC.

Speed Governor

The speed governor controls the SG frequency by modifying the fuel injection set point. For simplicity, a PI controller has been used [134]. This controller is linear, so state-space matrices can be defined as:

$$\left[\Delta \dot{\beta}\right] = B_{Gov} \left[\Delta \omega_r^*\right] + B_{Gov2} \left[\Delta \omega_r\right], \tag{3.15}$$

$$\left[\Delta f\right] = C_{Gov} \left[\Delta \beta\right] + D_{Gov} \left[\Delta \omega_r^*\right] + D_{Gov} \left[\Delta \omega_r\right], \tag{3.16}$$

where β is the state variable of the speed governor and ω_r^* is the frequency set point.

Diesel Generator Aggregated Small-Signal Model

The detailed models defined in the previous subsections can be merged together to form the model of the diesel generator. Input variables are transformed from real to pu

values, while the output variables are transformed from pu to real values. The resulting model is:

$$\left[\Delta \dot{x}_{SG}\right] = A_{SG}\left[\Delta x_{SG}\right] + B_{SG1}\left[\Delta v^{*}_{sg}\right] + B_{SG2}\left[\Delta \omega^{*}_{sg}\right] + B_{SG3}\left[\Delta v^{DQ}_{sg}\right], \tag{3.17}$$

$$\left[\Delta i^{DQ}_{sg}\right] = C_{SG1}\left[\Delta x_{SG}\right], \quad \left[\Delta \omega_{sg}\right] = C_{SG2}\left[\Delta x_{SG}\right], \tag{3.18}$$

where x_{SG} is the vector of state variables of the gen set.

3.2.2 Small-Signal Model of the GFL Converter

The small-signal model of a GFL converter includes an LCL filter, a current controller (in dq), the calculation of the current set points and a PLL. The detailed state space model can be found in the Appendix A and in the literature [138]. Only the PLL is presented here.

Phase-Locked Loop (PLL)

A PLL is used to synchronise the GFL converter (in dq) with the voltage at the PCC (in DQ), as shown in Fig. 3.3. Fig. 3.3 represents the diagram of the PCC in the SRF of the GFL converter (dq). Due to this reason δ_{PLL} is calculated using the frequency of the common reference frame ($\omega_{com} = \omega_{sg}$). A typical PLL implementation has been considered [26, 138]:

$$\dot{\epsilon} = k_{ipll}(v^{D}_{pcc}\cos\delta_{PLL} + v^{Q}_{pcc}\sin\delta_{PLL}), \tag{3.19}$$

$$\dot{\delta}_{PLL} = \epsilon + k_{ppll}(v^{D}_{pcc}\cos\delta_{PLL} + v^{Q}_{pcc}\sin\delta_{PLL}) - \omega_{sg}, \tag{3.20}$$

where ϵ is the state variable of the PLL, δ_{PLL} is the angle generated by the PLL and k_{ppll} and k_{ipll} are the proportional and integral constants of the PI. Clearly, the PLL is a non-linear system as it has trigonometric functions involved. Its linearised model is:

$$\begin{bmatrix}\Delta\dot{\epsilon}\\ \Delta\dot{\delta}_{PLL}\end{bmatrix}_i = A^{i}_{PLL}\begin{bmatrix}\Delta\epsilon\\ \Delta\delta_{PLL}\end{bmatrix}_i + B^{i}_{PLL1}\left[\Delta v^{DQ}_{pcc}\right]_i + B^{i}_{PLL2}\left[\Delta\omega_{com}\right]_i, \tag{3.21}$$

where ω_{com} is the frequency of the common reference frame (DQ) and index i will be used to denote the converter. The detailed matrices can be found in Appendix A.

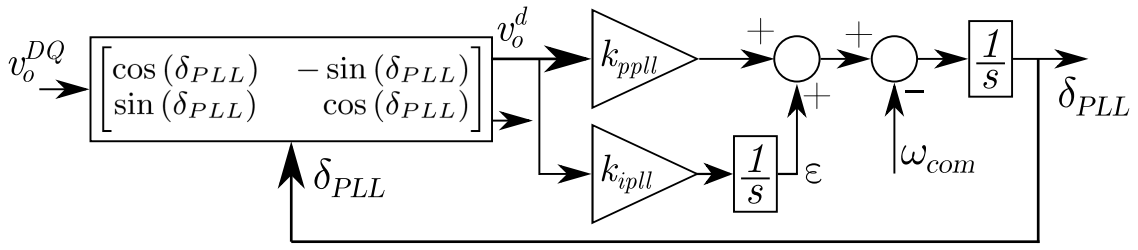

Figure 3.3: SRF-PLL control diagram, in dq.

Aggregated Small-Signal Model of the GFL Converter

The small-signal models of the current set points calculation, the current controller, the LCL filter and the PLL are then combined to obtain the GFL converter model:

$$\left[\Delta\dot{x}_{inv}\right]_{GFL} = A^{GFL}\left[\Delta x_{inv}\right]_{GFL} + B_{PQ}^{GFL}\begin{bmatrix}\Delta p^*\\ \Delta q^*\end{bmatrix}_{GFL} + \\ + B_V^{GFL}\left[\Delta v_{pcc}^{DQ}\right]_{GFL} + B_\omega^{GFL}\left[\Delta\omega_{com}\right]_{GFL}, \quad (3.22)$$

where

$$\left[\Delta x_{inv}\right]_{GFL} = \left[\Delta\epsilon,\ \Delta\delta_{PLL},\ \Delta\gamma^{dq},\ \Delta i_i^{dq},\ \Delta v_c^{dq},\ \Delta i_o^{dq}\right]_{GFL}^T, \quad (3.23)$$

$$\left[\Delta u_{inv}\right]_{GFL} = \left[\Delta p^*,\ \Delta q^*,\ \Delta v_{pcc}^{DQ},\ \Delta\omega_{com}\right]_{GFL}^T, \quad (3.24)$$

$$\left[\Delta i_{DQ}\right]_{GFL} = C^{GFL}\left[\Delta x_{inv}\right]_{GFL}, \quad (3.25)$$

where p^* and q^* are the active and reactive power set points of the GFL converter, γ^{dq} are the state variables of the current controller and i_i, v_c and i_o are internal current, capacitor voltage and external current of the LCL filter.

One should note that v_{pcc}^{DQ} represents an input variable of the state-space model. However, in the GFL converter model, variables are referenced to the local dq reference frame. Therefore, they should be transformed by taking into account (A.74), (A.76) and (A.77), derived from (3.1). This transformation is directly included in the state-space matrices A^{GFL}, B_{PQ}^{GFL}, B_V^{GFL}, B_ω^{GFL} and C^{GFL}, in (A.78)−(A.82).

3.2.3 Small-Signal Model of the GFM Converter

The model of the GFM converter consist of the models of the LCL filter, the current controller, the voltage controller and the droop controller (details in the Appendix A) [70].

Aggregated Small-Signal Model of the GFM Converter

All the models mentioned above are combined to obtain the small-signal model of the GFM converter:

$$\left[\Delta\dot{x}_{inv}\right]_{GFM} = A^{GFM}\left[\Delta x_{inv}\right]_{GFM} + B_{In}^{GFM}\begin{bmatrix}\Delta\omega_{nd}\\ \Delta v_{nd}^{dq}\end{bmatrix}_{GFM} + \\ + B_V^{GFM}\left[\Delta v_{pcc}^{DQ}\right]_{GFM} + B_{\omega com}^{GFM}\left[\Delta\omega_{com}\right]_{GFM}, \quad (3.26)$$

$$\left[\Delta i_o^{DQ}\right]_{GFM} = C_I^{GFM}\left[\Delta x_{inv}\right]_{GFM}, \quad (3.27)$$

$$\left[\Delta\omega_{com}\right]_{GFM} = C_\omega^{GFM}\left[\Delta x_{inv}\right]_{GFM} + D_\omega^{GFM}\begin{bmatrix}\Delta\omega_{nd}\\ \Delta v_{nd}^{dq}\end{bmatrix}_{GFM}, \quad (3.28)$$

where

$$[\Delta x_{inv}]_{GFM} = \left[\Delta\delta,\ \Delta\tilde{P},\ \Delta\tilde{Q},\ \Delta\phi^{dq},\ \Delta\gamma^{dq},\ \Delta i_i^{dq},\ \Delta v_c^{dq},\ \Delta i_o^{dq}\right]^T_{GFM}, \tag{3.29}$$

ω_{nd} and v_{nd} are the droop no load characteristics, $\tilde{P}$ and $\tilde{Q}$ are the filtered active and reactive powers, δ is the relative angle of the reference frame and ϕ^{dq} are the state variables of the voltage controller. As in (3.22), the state-space matrices include the transformations between the reference frames (details in Appendix A).

3.2.4 Load Modelling

A resistive-inductive linear load has been considered [42]:

$$\left[\Delta \dot{i}_l^{DQ}\right] = A_L\left[\Delta i_l^{DQ}\right] + B_{L1}\left[\Delta v_{pcc}^{DQ}\right] + B_{L2}\left[\Delta\omega_{com}\right], \tag{3.30}$$

being i_l^{DQ} the current absorbed by the load in the DQ reference frame.

The state matrices can be found in Appendix A.

3.2.5 Coupling of Devices

The linearised mathematical models of the diesel gen-set, the converters and the load include variable Δv_{pcc}^{DQ} as their input and the currents as their output. Therefore, an auxiliary resistor has been used to define this voltage adequately (R_x in Fig. 3.1) [70]:

$$\left[\Delta v_{pcc}^{DQ}\right] = D_{R1}\left[\Delta i_o^{DQ}\right]_{GFM} + D_{R1}\left[\Delta i_o^{DQ}\right]_{GFL} + D_{R2}\left[\Delta i_l^{DQ}\right]. \tag{3.31}$$

3.2.6 Aggregated Model of MG1: Gen-Set, GFL Converter and Load

Because of the MG topology v_{pcc}^{DQ} and ω_{com} are equivalent to v_{sg}^{DQ} and ω_{sg} (their real values). Then, the MG model is:

$$\begin{bmatrix}\Delta\dot{x}_{SG}\\ \Delta\dot{x}_{inv}\\ \Delta\dot{x}_L\end{bmatrix} = A^{MG1}\begin{bmatrix}\Delta x_{SG}\\ \Delta x_{inv}\\ \Delta x_L\end{bmatrix} + B_v^{MG1}\left[\Delta v_{sg}^*\right] + B_\omega^{MG1}\left[\Delta\omega_{sg}^*\right] + B_{PQ}^{MG1}\begin{bmatrix}\Delta p^*\\ \Delta q^*\end{bmatrix}, \tag{3.32}$$

where

$$A^{MG1} = \begin{bmatrix} A_{SG} + B_{SG3}D_{R1}C_{SG1} & B_{SG3}D_{R1}C^{GFL} & B_{SG3}D_{R2}\\ B_\omega^{GFL}C_{SG2} + B_V^{GFL}D_{R1}C_{SG1} & A^{GFL} + B_V^{GFL}D_{R1}C^{GFL} & B_V D_{R2}\\ B_{L2}C_{SG2} + B_{L1}D_{R1}C_{SG1} & B_{L1}D_{R1}C^{GFL} & A_L + B_{L1}D_{R2}\end{bmatrix},$$

$$B_v^{MG1} = \begin{bmatrix}B_{SG1}\\ 0\\ 0\end{bmatrix}, B_\omega^{MG1} = \begin{bmatrix}B_{SG2}\\ 0\\ 0\end{bmatrix}, B_{PQ}^{MG1} = \begin{bmatrix}0\\ B_{PQ}^{GFL}\\ 0\end{bmatrix}.$$

3.2.7 Aggregated Model of MG2: GFM and GFL Converters and Load

In MG2, $v_o^{DQ} = v_{pcc}^{DQ}$. By using a virtual resistor to combine all the elements, the following model is obtained:

$$\begin{bmatrix} \Delta\dot{x}_{invGFM} \\ \Delta\dot{x}_{invGFL} \\ \Delta\dot{x}_L \end{bmatrix} = A^{MG2} \begin{bmatrix} \Delta x_{invGFM} \\ \Delta x_{invGFL} \\ \Delta x_L \end{bmatrix} + B_{\omega v}^{MG2} \begin{bmatrix} \Delta\omega_{nd} \\ \Delta v_{nd}^{dq} \end{bmatrix} + B_{PQ}^{MG2} \begin{bmatrix} \Delta p^* \\ \Delta q^* \end{bmatrix}, \tag{3.33}$$

where

$$A^{MG2} = \begin{bmatrix} A^{GFM} + B_{\omega com}^{GFM} C_{\omega com}^{GFM} + B_V^{GFM} D_{R1} C_I^{GFM} & B_V^{GFM} D_{R1} C^{GFL} & B_V^{GFM} D_{R1} C_L \\ B_\omega^{GFL} C_\omega^{GFM} + B_V^{GFL} D_{R1} C^{GFL} & A^{GFL} + B_V^{GFL} D_{R1} C^{GFL} & B_V^{GFL} D_{R2} C_L \\ B_{L2} C_\omega^{GFM} + B_{L1} D_{R1} C_I^{GFM} & B_{L1} D_{R1} C^{GFL} & A_L + B_{L1} D_{R2} C_L \end{bmatrix},$$

$$B_{\omega v}^{MG2} = \begin{bmatrix} B_{In}^{GFM} + B_{\omega com}^{GFM} \begin{bmatrix} D_{P\omega}^{GFM} & 0 \end{bmatrix} \\ B_\omega^{GFL} \begin{bmatrix} D_{P\omega}^{GFM} & 0 \end{bmatrix} \\ B_{L2} \begin{bmatrix} D_{P\omega}^{GFM} & 0 \end{bmatrix} \end{bmatrix}, \; B_{PQ}^{MG2} = \begin{bmatrix} 0 \\ B_{PQ}^{GFL} \\ 0 \end{bmatrix}.$$

3.3 Analytic Study

In this section, MG1 and MG2 are analysed. System stability is analysed based on the information obtained from the participation factors and system eigenvalues (Fig. 3.4, Fig. 3.5, Fig. 3.6 and Fig. 3.7 for MG1, and Fig. 3.8, Fig. 3.9, Fig. 3.10 and Fig. 3.11 for MG2, respectively) [42]. The small signal model of each scenario presented in the study was developed considering their individual operating points. The operating point of each scenario was calculated by means of a non-linear model developed in *Simulink*. Then, the small signal model was used to calculate eigenvalues and participation factors. Participation factors have been calculated as in [42]:

$$P_M = \begin{bmatrix} f_{11} & \cdots & f_{1m} \\ \vdots & \ddots & \vdots \\ f_{m1} & \cdots & f_{mm} \end{bmatrix}, \quad f_{ki} = \frac{\partial \lambda_i}{\partial a_{kk}} = \psi_{ik}\phi_{ki}, \tag{3.34}$$

where the participation factor f_{ki} measures the participation of the ith eigenvalue (λ_i) on the kth state variable (Δx_k), m denotes the number of states, ψ_{ik} is the kth element of the left row eigenvector and ϕ_{ki} is the kth element of the right column eigenvector associated with λ_i. Each participation factor is calculated as the derivative of the eigenvalue λ_i with respect to a_{kk}, which is in the diagonal of the characteristic matrix of the dynamic system. Eigenvectors were normalised so that $\psi_i\phi_i = 1$ This implies that the sum of the participation factors along a row or a column is equal to one [42]:

$$\sum_{i=1}^{m} f_{ki} = 1, \quad \sum_{k=1}^{m} f_{ki} = 1. \tag{3.35}$$

3.3.1 Test System Description

The nominal power of the SG is 60 kVA. The electromechanical parameters of the SG and the diesel engine are taken from reference [134]. For the excitation system, the reference values are taken from the AC5A model in [137] (see Table 3.1). Parameters of GFM and GFL converters are defined in Table 3.2. Two VSCs of the same power rating (15kVA) (and, therefore, the same LCL parameters) have been considered.

Table 3.1: Diesel gen-set parameters (SC1).

Parameter	Value	Parameter	Value	Parameter	Value
r_a	3.54E-2 pu	l_{kkq}	1.4967 pu	σ	1 pu
r_f	6E-4 pu	l_{ad}	2.38 pu	k_{pAVR}	2.47 pu
r_{kd}	3.54E-2 pu	l_{aq}	1.24 pu	k_{iAVR}	0.42 pu
r_{kQ}	4.28E-2 pu	H	3.7E-1 s	k_{pGov}	5.57 pu
l_d	2.83 pu	T_E	0.8 pu	k_{iGov}	6.39 pu
l_q	1.69 pu	S_E	1 pu	Poles	4 pu
l_{ff}	2.6371 pu	K_E	0.68 pu	U_B	$400\sqrt{2}$ V
l_{kkd}	2.58 pu	τ_m	0.1 pu	f_B	50 Hz

Table 3.2: Parameters of GFM and GFL converters (SC1).

Parameter	Value	Parameter	Value
L_i	2.3 mH	$k_{iv}(GFM)$	6.92
R_i	72.2 mΩ	m_p	6.67E-6
L_o	0.93 mH	n_q	3.33E-4
R_o	29.2 mΩ	ω_c	31.41
C_d	8.83 μF	$k_{pc}(GFL)$	4.43
$k_{pc}(GFM)$	1.81	$k_{ic}(GFL)$	3.05E3
$k_{ic}(GFM)$	2.17E3	k_{ppll}	0.0136
$k_{pv}(GFM)$	0.0553	k_{ipll}	0.0492

A base scenario (SC1) has been defined for both MGs. In SC1, the load is consuming 18 kW. The active power set point for the GFL converter is 4 kW and the reactive power set point is zero. The voltage and frequency set points of the SG are 400 V and 50 Hz, respectively. The AVR and the speed governor have been designed to be as fast as possible, resulting in bandwidths of 0.17 Hz and 1.7 Hz, respectively (see Table 3.1). Controllers have been designed by using open-loop techniques, with phase

margins of 45 deg (speed governor and current controllers), 50 deg (AVR) and 60 deg (PLL and voltage controller). The bandwidth of the current controller and the PLL of the GFL converter are set to 490 Hz and 1.4 Hz, respectively, while the bandwidth of the current and voltage controllers of the GFM converter are set to 490 Hz and 30 Hz, respectively. The rest of parameters are defined according to Table 3.2. Additional scenarios considered in this study are defined in Table 3.3. Scenarios SC2 to SC23 are derived by modifying some parameters of the base scenario.

Table 3.3: Definition of scenarios SC2-SC23 showing the initial (base) scenario, the parameter changed, its new value and the purpose related to PLL design.

SC	**Base SC**	**Changed Param**	**New Value**	**Impact evaluation of:**
SC2	SC1	P_{GFL}	6 kW	Power sharing
SC3	SC1	P_{GFL}	9 kW	Power sharing
SC4	SC1	P_{GFL}; P_L	2,6 kW; 12 kW	Low loading conditions
SC5	SC1	P_{GFL}; P_L	4 kW; 12 kW	Low loading conditions
SC6	SC1	P_{GFL}; P_L	6 kW; 12 kW	Low loading conditions
SC7	SC6	$BWGFL_{cc}$	380 Hz	Low current control speed
SC8	SC6	$BWGFL_{cc}$	260 Hz	Low current control speed
SC9	SC7	J	3,6 kg m^2	SG inertia
SC10	SC7	J	0,9 kg m^2	SG inertia
SC11	SC7	BWf	2,1 Hz	Governor speed
SC12	SC7	BWf	0,5 Hz	Governor speed
SC13	SC1	P_{GFL}; P_L	12 kW; 18 kW	Power sharing
SC14	SC1	P_{GFL}; P_L	8 kW; 12 kW	Low loading conditions
SC15	SC14	$BWGFL_{cc}$	380 Hz	Slower GFL CC
SC16	SC14	$BWGFL_{cc}$	260 Hz	Slower GFL CC
SC17	SC16	GFM_{vc}; GFM_{cc}	30 Hz; 260 Hz	Slower GFM CC
SC18	SC16	GFM_{vc}; GFM_{cc}	20 Hz; 490 Hz	Slower GFM VC
SC19	SC16	GFM_{vc}; GFM_{cc}	20 Hz; 260 Hz	Slower GFM CC and VC
SC20	SC1	P_{GFL}; P_L; GFL_{cc}; GFL_{PLL}	9 kW; 23 kW; 120 Hz; 17 Hz	Limit case for stability evaluation of MG1
SC21	SC1	P_{GFL}; P_L; GFM_{cc}; GFM_{vc}; GFL_{cc}; GFL_{PLL}	11 kW; 13 kW; 520 Hz; 34 Hz; 250 Hz; 19 Hz	Limit case for stability evaluation of MG2
SC22	SC20	GFL_{cc}; GFL_{PLL}	380 Hz; 7 Hz	SC20 redesigned parameters
SC23	SC21	GFM_{cc}; GFM_{vc}; GFL_{cc}; GFL_{PLL}	380 Hz; 40 Hz; 380 Hz; 7 Hz	SC21 redesigned parameters

3.3.2 Participation Factors for MG1 (Diesel Gen-Set)

Fig. 3.4 shows the moduli of the participation factors for MG1, SC1. For instance, the modulus of the participation factors of state δ_{PLL} in the modes 7-13 are 0.03, 0.03, 0.7, 0.7, 0.08, 0.08 and 0.03, respectively. Modes are ordered by numbers in the x-axis according to their proximity to the imaginary axis (1 being the closest). The states related to the SG are mainly affected by Modes $1-8$. These modes have small influence on the PLL states, while their influence on the rest of the GFL converter states is negligible. Modes $6-12$ participate in the engine and the rotor states (ω_r and t_m), but also in the PLL states (ϵ and δ_{PLL}), thus creating a dynamic interaction between the two devices. Modes $11-12$ are related to the PLL (ϵ and δ_{PLL}) and the current controller (γ_d) and, therefore, represent their interaction. The rest of the modes are mainly related to electromagnetic phenomena and represent the link between the current controller, the LCL filter variables and the load.

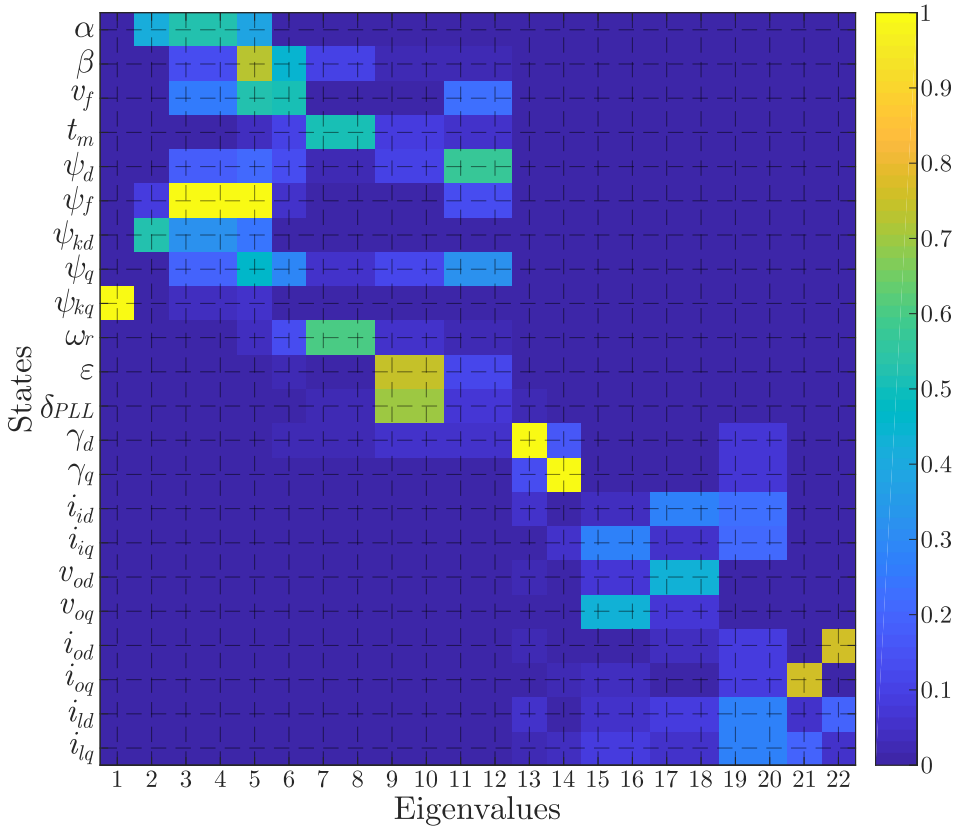

Figure 3.4: Participation matrix for MG1, SC1. Eigenvalues are ordered left to right according to their distance from the imaginary axis.

In contrast to the existing literature, no relevant interactions were observed between the PLL and the voltage controller of the diesel gen-set, as it was previously reported in the literature when standard excitation AC4A was used [27, 137]. This could be

motivated by the use of different AVR and excitation system (AC4A excitation is used in [27, 137] while here AC5A and a PI controller were considered) [139].

3.3.3 Stability Limits of MG1 (Diesel Gen-Set)

Fig. 3.5, Fig. 3.6 and Fig. 3.7 show how the eigenvalues of MG1 are affected by the PLL bandwidth in different scenarios. Only low frequency eigenvalues are shown because the PLL mainly affects low frequency dynamics. Fig. 3.5 shows the eigenvalues for six different loading scenarios (SC1-SC6), with three different levels of power injected by GFL converter (22 %, 33 % and 50 % of load). The eigenvalues that are affected by the PLL move towards the imaginary axis when the relative power share of the GFL converter is increased. This effect is more pronounced and evident at light load conditions. For instance, in SC1 and SC4 the GFL converter has a 22 % power share but the eigenvalues in SC4 (the lightest load) are located closer to the imaginary axis. This will result in a reduction of the stability limits linked with the parameters of the PLL.

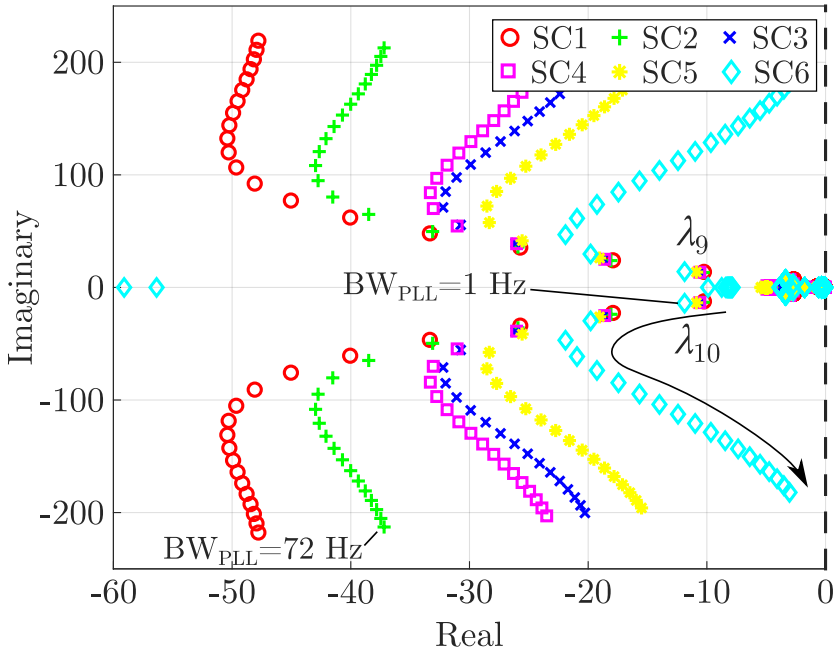

Figure 3.5: Trajectory of MG1 eigenvalues (low frequency) when the bandwidth of PLL is increased for different loading conditions. See Table 3.3 for detailed definition of scenarios.

Fig. 3.6 shows the results of the study for three scenarios with different bandwidths of the current controller (SC6, SC7 and SC8). The current controller bandwidth has a strong influence on the maximum bandwidth attainable by the PLL. The lower the current controller bandwidth, the lower the PLL bandwidth attainable. For instance, for a current controller bandwidth of 260 Hz (SC8), the MG becomes unstable when the

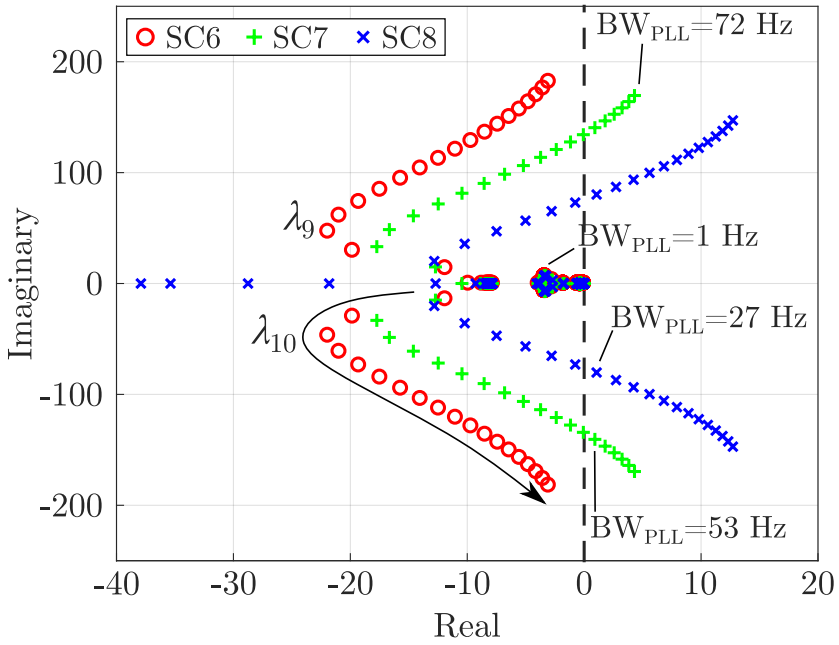

Figure 3.6: Trajectory of MG1 eigenvalues (low frequency) when the bandwidth of PLL is increased for different current controller bandwidths of the GFL converter. See Table 3.3 for detailed definition of scenarios.

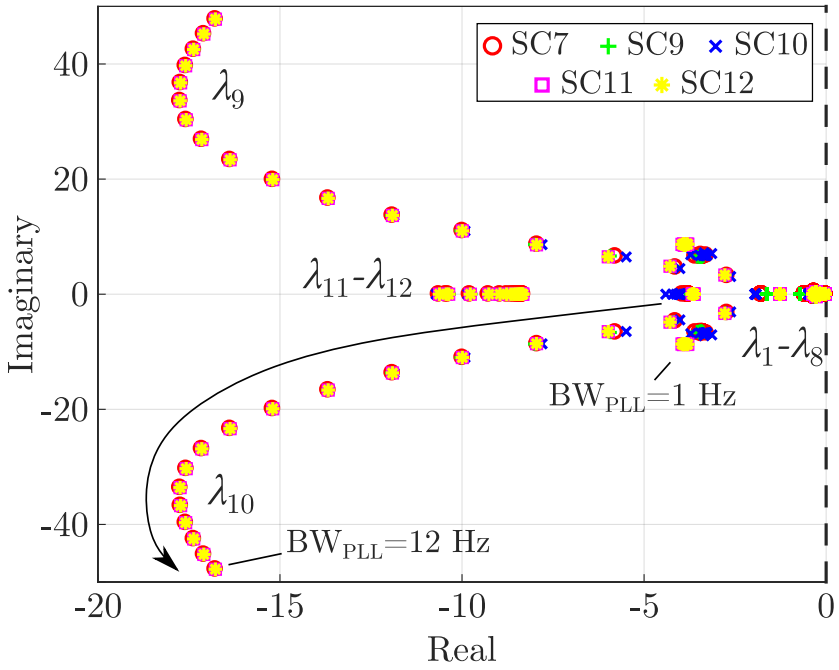

Figure 3.7: Trajectory of MG1 eigenvalues (low frequency) when the bandwidth of PLL is increased for different designs of speed governor and SG inertia. See Table 3.3 for detailed definition of scenarios.

PLL bandwidth is higher than 27 Hz; while for current controller bandwidth of 380 Hz (SC7), the MG becomes unstable when the PLL bandwidth is higher than 53 Hz.

Different scenarios for the inertia and the design of the speed governor have been examined and the results are collected in Fig. 3.7 (SC7, SC9, SC10, SC11 and SC12) showing that the SG inertia and the bandwidth of the speed governor have little influence on the eigenvalues linked with the PLL.

In summary, for the type of the generator, prime movers and controllers considered, the mechanical parameters have only a small contribution to the eigenvalues related to the PLL. In contrast, the loading conditions and the design of the current controller greatly affect the aforementioned eigenvalues. With this respect, increased load levels, low relative power contribution from the GFL converter and fast current controllers are preferable. A summary is presented in Table 3.4.

3.3.4 Participation Factors for MG2 (GFM Converter)

Fig. 3.8 shows the participation matrix for MG2 and SC1. Each mode of MG2 participates only in one state or in two related ones, like ϵ and δ_{PLL}, at most. Clearly, here the states and modes are more decoupled than in MG1. Modes 2−3 mainly participate

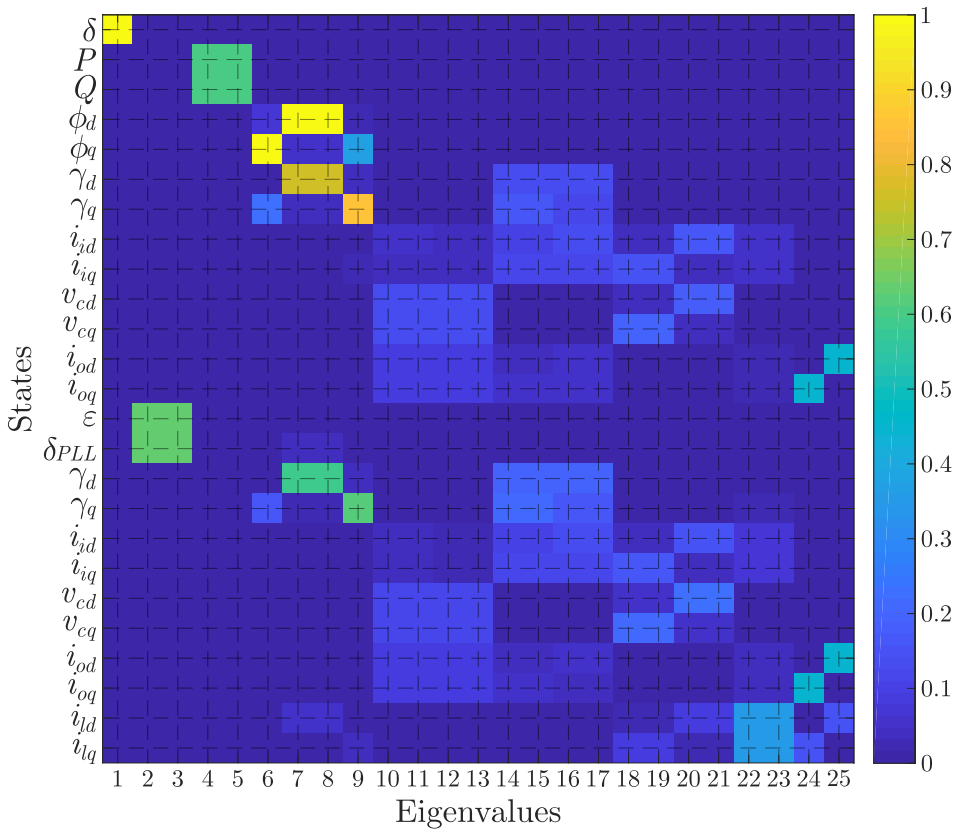

Figure 3.8: Participation matrix of MG2, SC1. Eigenvalues are ordered left to right according to their distance from the imaginary axis.

in the states related to the PLL, and to a lesser extent, the states of the voltage controller of the GFM converter. The interaction between these parameters is studied in the following section.

3.3.5 Stability Limits of MG2 (GFM Converter)

Fig. 3.9, Fig. 3.10 and Fig. 3.11 show the trajectories of the low frequency eigenvalues of MG2 as the PLL bandwidth is increased, in different scenarios. Fig. 3.9 shows that in MG2, as in MG1, the eigenvalues move to the right when the power injected by the GFL converter increases. For instance, scenarios in SC2, SC3 and SC13 (with the same load) as power injected by the GFL converter increases (from SC2 to SC13 respectively) eigenvalue λ_6 is closer to the imaginary axis. Scenarios with light-load conditions (SC5, SC6 and SC14) also tend to destabilise the system more when compared to those with more load (SC2, SC3 and SC13 respectively). For instance, scenarios in SC2 and SC5 present the same power sharing for converters, but load is lower in SC5. In this case eigenvalue λ_6 is closer to the imaginary axis in SC5 compared to SC2. Furthermore Fig. 3.9 shows that for PLL bandwidths higher than 20 Hz approximately, λ_6 and λ_7 move away from the imaginary axis although eigenvalues present slightly lower damping. This aspect, that can also be seen in Fig. 3.10 and Fig. 3.11, has not been studied in detail since PLL bandwidths values higher than 20 Hz are not common.

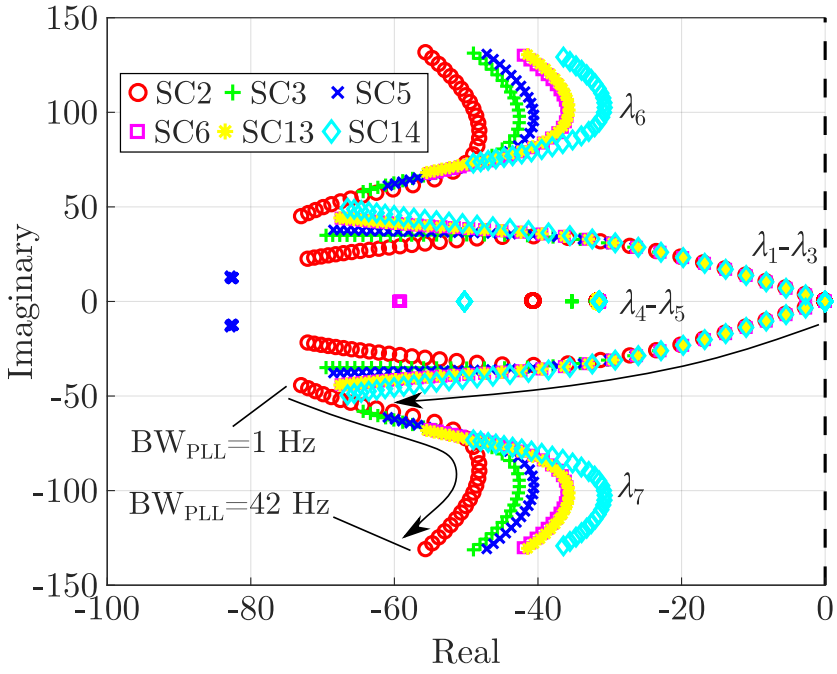

Figure 3.9: Trajectory of MG2 eigenvalues (low frequency) when the PLL bandwidth of is increased for different loading conditions. Table 3.3 shows the details of scenarios.

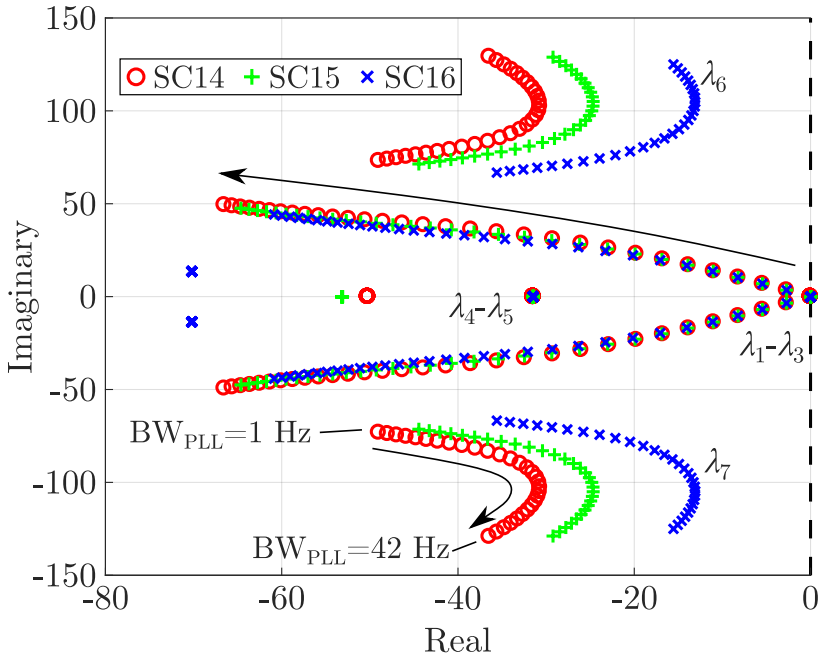

Figure 3.10: Trajectory of MG1 eigenvalues (low frequency) when the bandwidth of PLL is increased for different current controller bandwidths of the GFL converter. See Table 3.3 for detailed definition of scenarios. The $BWGFL_{cc}$ in SC6, SC7 and SC8 is (red) 490 Hz, (green) 380 Hz and (blue) 260 Hz, respectively.

Fig. 3.10 shows that eigenvalues are closer to the imaginary axis if the bandwidth of the current controller decreases, similarly to the case of MG1. This results in limited PLL bandwidth under certain loading conditions.

Fig. 3.11 shows MG2 eigenvalues when the bandwidth of the PLL increases for different designs of the GFM converter voltage and current controllers. As shown in Fig. 3.11, the eigenvalues are closer to the imaginary axis when the voltage controller is slowed down (SC18 and SC19). In general, interactions between the voltage and current controllers are avoided by ensuring a sufficient time-constant separation between them. More precisely, current controllers are typically designed to be faster than voltage controllers. However, as shown in Fig. 3.11, increasing the GFM converter current controller bandwidth has a negative effect on the stability (comparing SC18 with SC19), unless the voltage controller bandwidth is increased at the same time (comparing SC18 with SC16).

In summary, both loading conditions and the design of the GFL converter current controller have impact on the eigenvalues related to the PLL, as it happened in MG1. Increased loading, low relative power injection by the GFL converter and fast current controllers in the GFL converter allow higher PLL bandwidths. The GFM converter also affects the design of the PLL. The PLL bandwidth can be increased for fast voltage

controllers and slow current controllers. In this case, the loading conditions do not limit the PLL design as much as in MG1. These aspects are summarised in Table 3.4.

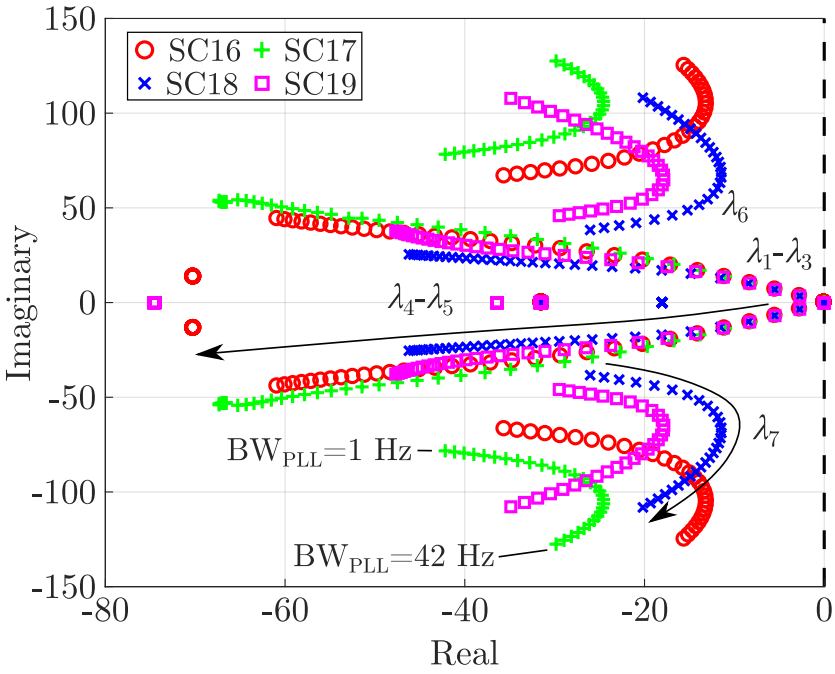

Figure 3.11: Trajectory of MG2 eigenvalues (low frequency) when the bandwidth of PLL is increased for different designs of the GFM converter voltage and current controllers. See Table 3.3 for detailed definition of scenarios.

Table 3.4: Changes that reduce PLL bandwidth stability limits.

Parameter	Type of change in parameter
P_L	Decrease ↓
P_{GFL}/P_{GFM}	Increase ↑ (specially in MGs with SG)
$BWGFL_{cc}$	Decrease ↓
$BWGFM_{vc}$	Decrease ↓
$BWGFM_{cc}$	Increase ↑

3.4 Guidelines for the Design of Control Parameters in a MG

The conclusions drawn from the analysis have been used to develop and propose design guidelines for the selection of control parameters in a MG. The guidelines assume the use of the small-signal model, however, some of the recommendations are generally applicable and are helpful even without the model. The flowchart with the design

procedure is shown in Fig. 3.12. The flowchart also indicates the sections in which each task is addressed. The design of the parameters is based on the stability limits calculated using the small-signal model. Initially, a stable scenario is used by applying typical values for the controllers. Preliminary stability limits are calculated by assuming this scenario, which is also used to compute a stable operating point. Then, the preliminary stability limits are used to define the controllers of the MG under most unfavourable conditions for the stability (low levels of power injected by the GFM device and high levels of power injected by the GFL converter). Both non-linear and linear models are developed for the unfavourable condition scenario. MG controllers are redesigned to meet the specifications taking into account the stability limits under the unfavourable conditions. At this point any design specification like response time, damping or phase margins can be considered.

3.4.1 Preliminary Controller Settings

Diesel-Based MGs

To start with, the controllers of diesel gen-sets can be configured to be as fast as it is required while the bandwidth of the PLL should be similar to that of the frequency controller. The current controller of the GFL converter should be designed in a typical way by using the desired settling time and the adequate damping of the LCL filter resonance [4, 26]. The bandwidth of the direct current (DC)-voltage controller should not be close to that one used for the PLL to avoid undesired oscillations. Also, it should not be unnecessarily wide [97, 140].

Converter-Based MGs

The current controllers of the GFL converter and the GFM converter should be designed by using standard design rules [4, 26]. Then, the voltage controller of the GFM converter should be configured to be as fast a possible, however, a sufficient time-constant separation between the current and the voltage loops must be guaranteed. The PLL can be designed to be fast enough to track standard frequency variations in power grids [141] (a bandwidth between 1 and 10 Hz would be sufficient in most cases). The DC-voltage controller, if required, should be designed in a similar way as it is done in diesel-based MGs.

3.4.2 Model Development, Operating Points and Stability

Non-Linear Model and Operating Point

A non-linear model of the MG is used to perform the time-domain simulations and to calculate the operating point. The model should include all the non-linear equations of

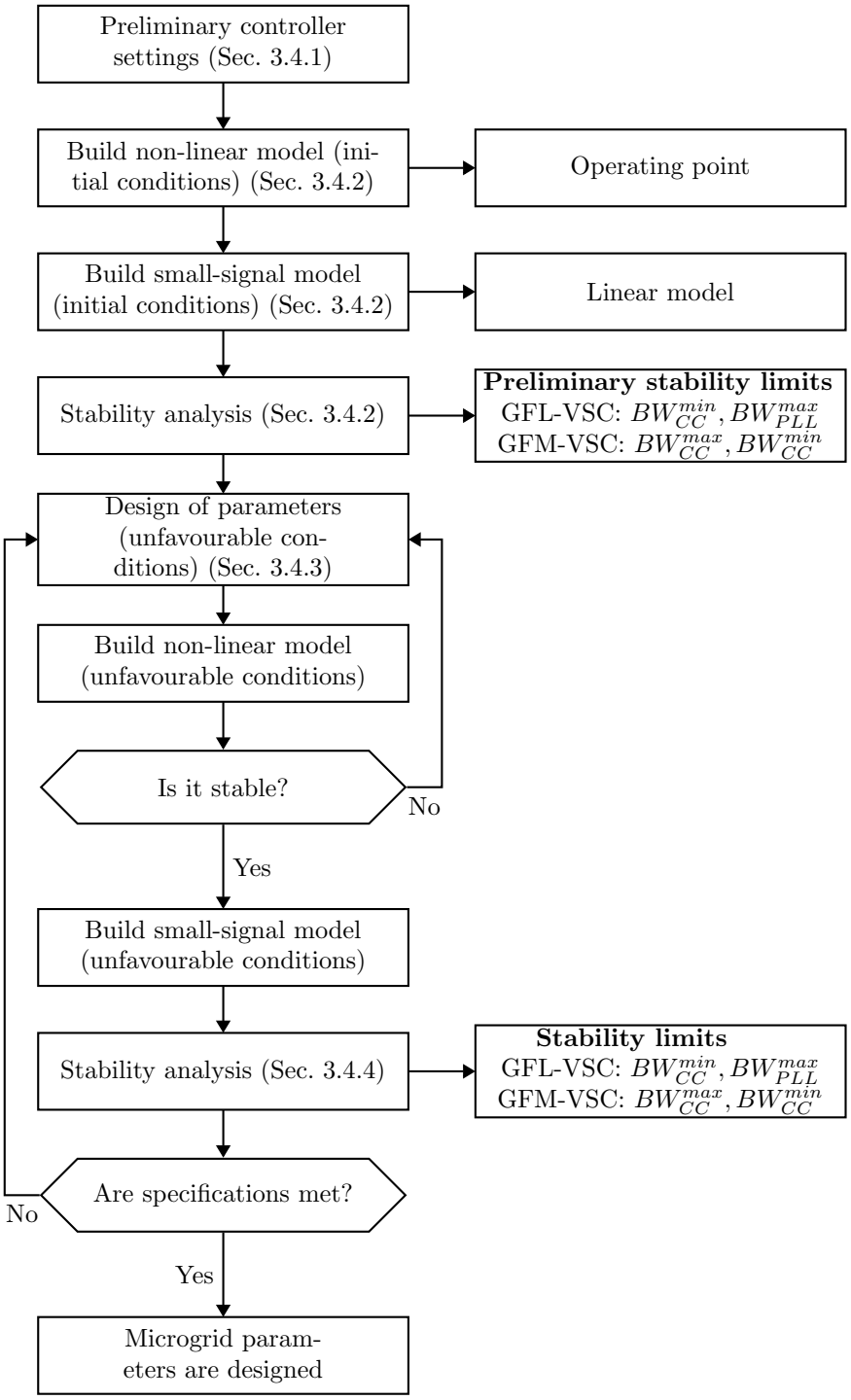

Figure 3.12: Flow chart of the proposed method for the design of MG controllers.

the desired GFM device (SG or converter), the GFL converter and the load. In order to find a suitable operating condition to start the analysis and the control design, it is recommended to set the GFM converter to feed a moderate load (50-80 % of its rated power) and the GFL converter not to inject any power.

Small-Signal Model of the MG

A small-signal model of the MG should be developed. It can be obtained by using the analytical expressions included in this thesis (in Section 3.2), or by using automatic tools (e.g. *Simulink Control Design* toolbox [142]).

Initial Conditions for the Stability Test

Stability limits of the bandwidth of MG controllers can be found by using the small-signal analysis techniques presented in this chapter. These limits will be used for the design of MG parameters under most unfavourable conditions.

3.4.3 Fine Tuning of Control Parameters under Unfavourable Conditions

An unfavourable operating condition can be found when the GFM converter injects its minimum power and when the relative GFL converter power injection is high. By following the steps mentioned before, the designer may have already found control parameter values that guarantee the stability. However, a more elaborated selection can lead to improved stability margins and an optimisation procedure can be used to find the optimal selection.

MGs Formed by Diesel Gen-Sets

The PLL can be redesigned by taking into account the upper limit of its bandwidth and the expected frequency variations. If the design specifications cannot be met, the GFL converter current controller should be made faster to increase the stability limit of the PLL bandwidth.

MGs Formed by GFM Converters

The current controller of the GFL converter can be redesigned by taking into account the lower stability limit imposed by the MG and other restrictions imposed by the LCL resonance and the switching frequency. Finally, the PLL can be redesigned by taking into account its upper stability limit and the expected variations of the MG frequency. If the design specifications cannot be fulfilled, the voltage and current controllers should be redesigned by reducing the bandwidth of the GFM converter current controller and increasing both - the bandwidth of the GFL converter current controller and the bandwidth of the voltage controller of the GFM converter to allow for wider PLL bandwidths.

3.4.4 Stability Analysis under Unfavourable Conditions

It is recommended to calculate the small-signal model for the operation under these conditions. Also, it is recommended to carry out transient simulations in order to check if the system operates within its limits even during large transients. If the system is not well damped (e.g. damping factor smaller than 0.3), the controllers should be redesigned. This can be checked by analysing the system eigenvalues. For example, the PLL and the current controller of the GFM converter can be slowed down, and the speed of the current controller of the GFL converter and the voltage controller of the GFM converter can be increased.

3.5 Experimental Validation

3.5.1 Prototype Description

MG1 and MG2 were implemented in the smart energy integration lab (SEIL) of IMDEA Energy [143,144] (Fig. 3.13 and Fig. 3.14). A 75 kVA VSC was used as the grid emulator. The model of the SG was implemented in the VSC to emulate the operation of the diesel gen-set and part of the load (12 kW) in MG1. Two 15 kVA converters were used as GFM converter and GFL converter in the experimental validation. Different loading conditions were implemented by using a programmable resistive load bank. The single-line electrical diagrams of the two MG implementations are shown in Fig. 3.14 (MG1 in red and green and MG2 in red and blue).

Figure 3.13: Lab photo. From left to right: (green) 75 kVA converter used as emulator for the SG and part of the load in MG1, (cyan) real time targets (converter controllers), (blue) 15 kVA converter used as GFM converter, (red) 15 kVA converter used as GFL converter, (yellow) AC bus bars and (magenta) loads.

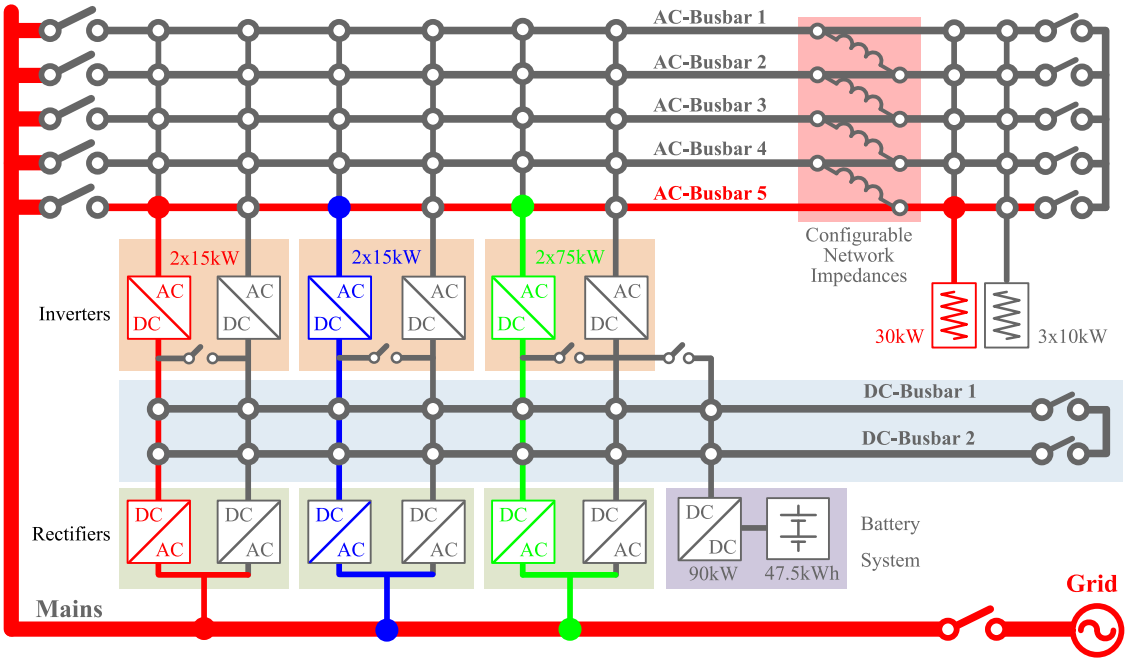

Figure 3.14: Electrical diagram of the laboratory. The common elements of MG1 and MG2 are shown in red (GFL converter and load). Grid emulator is shown in green, and GFM converter is shown in blue. MG1: red and green. MG2: red and blue.

3.5.2 Validation of Small-Signal Models

Fig. 3.15 and Fig. 3.16 show a comparison between the transient responses obtained from the experimental setup and the linearised models when applying scenario SC1. Since MG dynamics is slow, the models are validated by using dq signals instead of oscilloscope, as it is common in the literature [70, 138]. Experimental dq signals were obtained from the control boards of the converters, without filters. The experimental results were also available by using an oscilloscope, see Fig. 3.17 as an example. However, in this case, it was difficult to compare the theoretical results with the experimental waveforms, therefore oscilloscope data was not used. A 10 V and a 0.2 Hz step were applied to the set points of the SG voltage and frequency controllers (Fig. 3.15). The same steps were used for the GFM converter (Fig. 3.16). It is clear that the small-signal models accurately reproduce the low-frequency dynamics of the experimental platform. Since high frequency phenomena (e.g. pulse-width modulation) were not considered in the modelling, high frequency dynamics cannot be predicted by using the developed linear models. In v_{dq}, ω_{GFL} and ω_{GFM} some harmonics can be observed due to the lack of filters at the measuring stage. This oscillations are not present in ω_{SG} because this variable is taken from the emulated model.

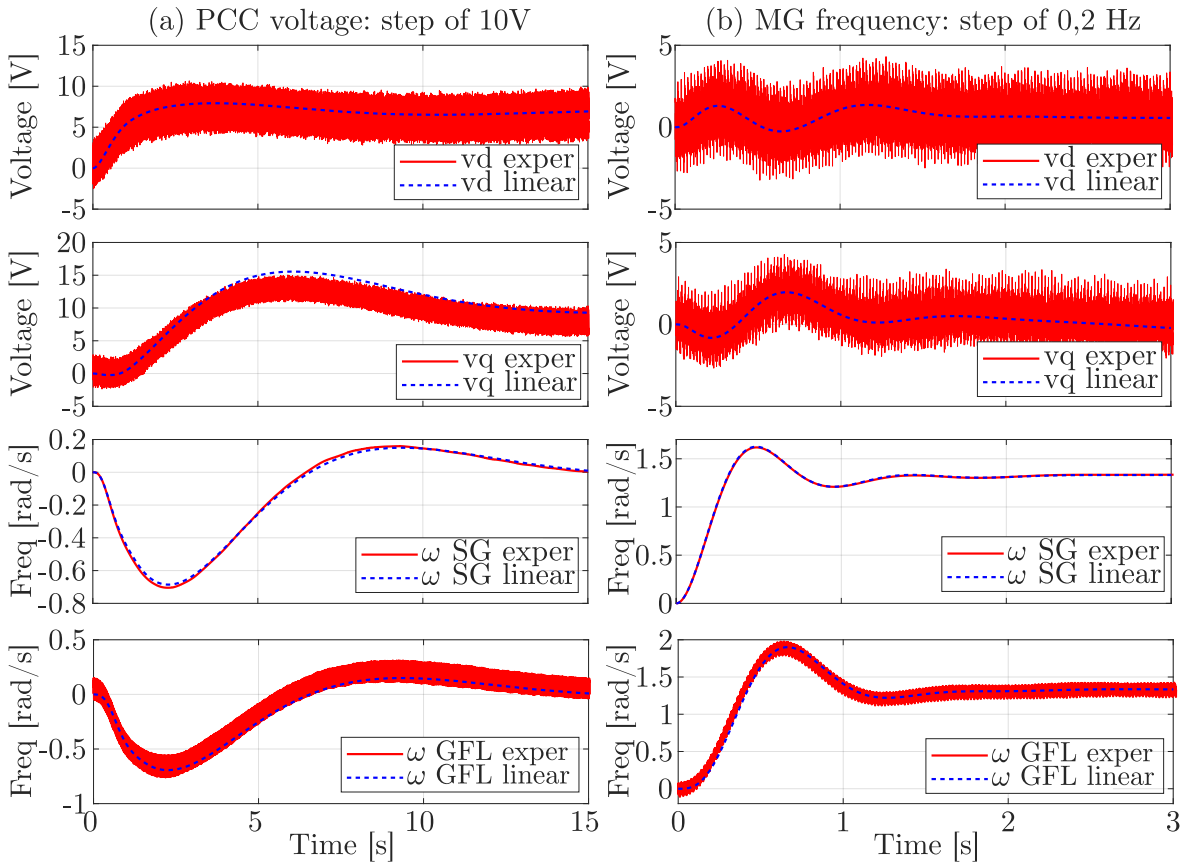

Figure 3.15: Response of MG1 when there is step change of (a) 10 V and (b) 0.2 Hz in the SG voltage and frequency set points. (red) Experimental and (blue) linearised model results.

3.5.3 Validation of Stability Limits

The theoretical stability limits of the PLL were validated experimentally. MG1 was validated for SC20, where the load was 23 kW (12 kW were emulated). The GFL converter injected 9 kW (39 %). The SG parameters are defined in Table 3.1. The current controller bandwidth was 120 Hz. In this scenario, the linear model analyses suggested a maximum PLL bandwidth of 18 Hz. However, during the validation, the system remained stable up to a bandwidth of 17 Hz. Even though the dynamics was accurately described by the linear model, the range of frequency for the system to be marginally stable differs slightly. This is common in experimental validations as linear models show different sensitivity to parameter variation at the edge of the stability region [145]. However, small-signal tools are still useful in grid applications since the main objective here is to ensure that the system operates away from the unstable region [42]. Fig 3.18 (a) shows the response of MG1 when the PLL bandwidth was 17 Hz and a variation of the load from 23 kW (SC20) to 22 kW was applied. This means that the GFL converter power varies from 39 % to 40 % of the total demand. The MG

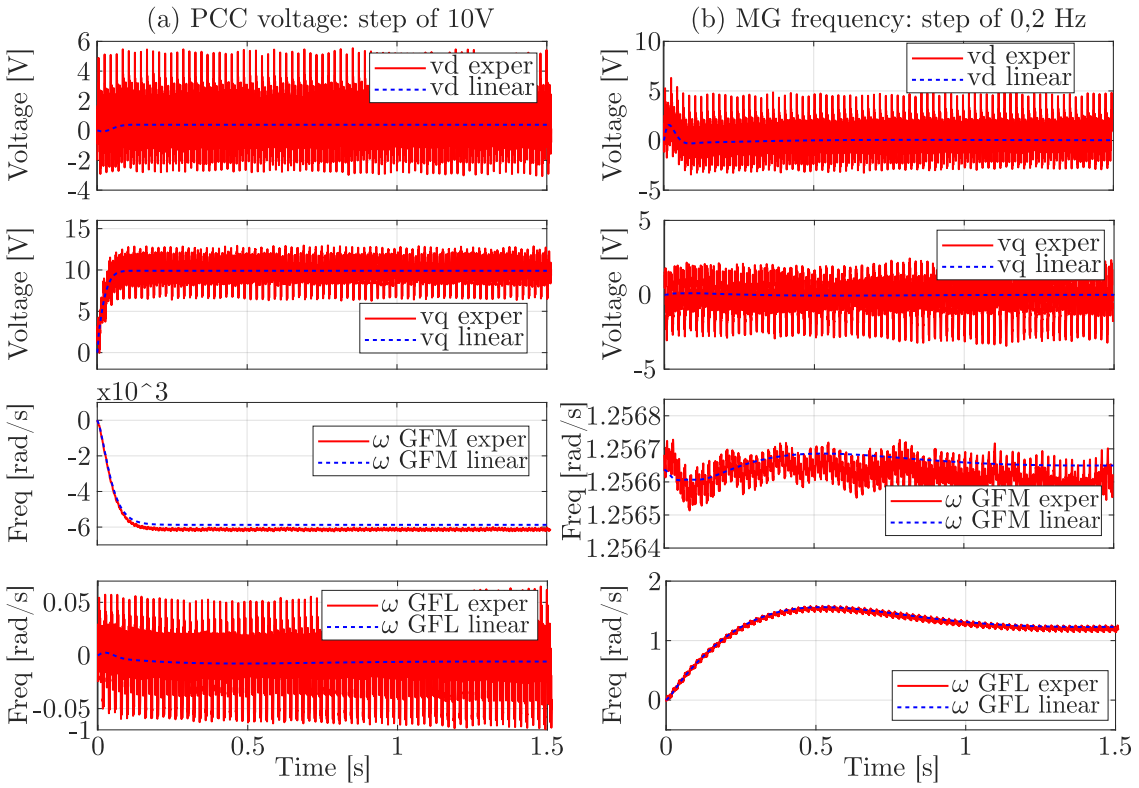

Figure 3.16: Response of MG2 for (a) a step of 10 V applied to the nominal voltage of the droop controller and (b) a step of 0.2 Hz applied to the nominal frequency of the controller. (red) Experimental results and (blue) linearised model results.

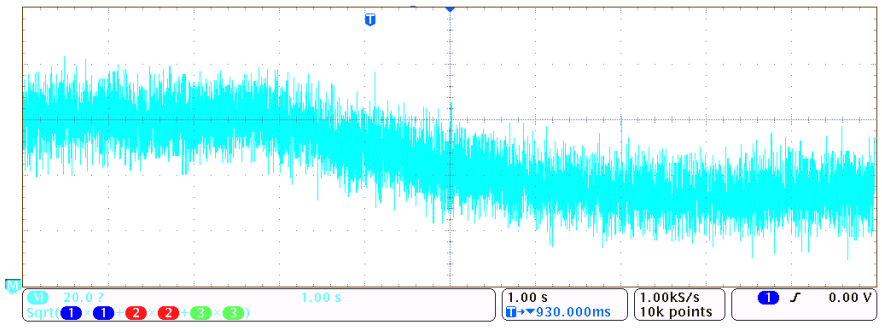

Figure 3.17: Response of modulus of v_{abc}, when there is a 10 V step change of the SG set point. Horizontal scale, 1 s/div, vertical scale, 20 V/div.

becomes unstable due to the higher ratio of power injected by the GFL converter. The load is increased back in two steps at $t = 10$ s and $t = 12$ s, and the MG recovers its sable operation.

The stability limits of MG2 where validated using SC21: $P_{load} = 13$ kW, $P_{GFL-VSC} = 11$ kW, $BW_{ccGFM} = 520$ Hz, $BW_{vcGFM} = 34$ Hz, $BW_{ccGFL} = 250$ Hz. The linear model analysis suggests the MG becomes unstable for PLL bandwidths higher than 21 Hz. In the validation, the maximum bandwidth was 19 Hz. Fig 3.18 (b) shows the response of

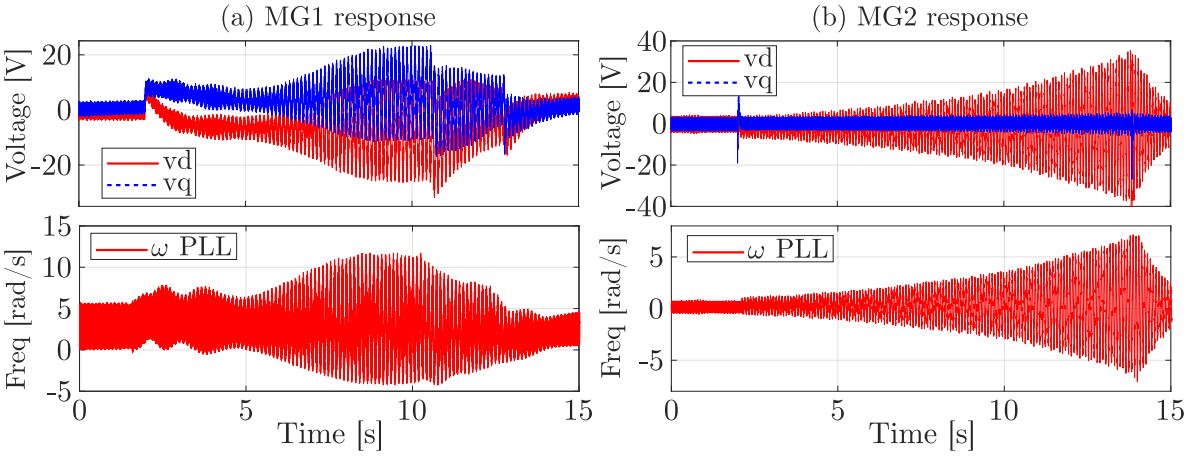

Figure 3.18: Response of MG1 and MG2 in SC20 and SC21, respectively, when the load decreases 1kW (and hence the ratio of power injected by the GFL converter increases) making both MGs unstable.

MG2 in SC21 when there was a load variation from 13 kW to 12 kW (85 % and 92 % of the load power injected by the GFL converter). MG2 became unstable with the load step at $t = 2$ s. The load returned to 13 kW at $t = 14$ s, and then the system regained its stability.

3.5.4 Validation of Design Procedure for Control Parameters

Controllers of MG1 and MG2 used in SC20 and SC21 were redesigned following the guidelines introduced in Section 3.4.3 for scenarios SC22 and SC23 respectively. In MG1, the current controller and the PLL of the GFL converter were designed to have bandwidths 380 Hz and 7 Hz, respectively. In MG2, the current and voltage controller bandwidths of the GFM converter were re-adjusted to 380 Hz and 40 Hz, respectively. Meanwhile, the PLL and the current controller bandwidths in GFL converter were designed to be 7 Hz and 380 Hz and, respectively.

Fig. 3.19 (c) and (d) and Fig. 3.20 (c) and (d) show the response of the MGs for SC22 and SC23, respectively, when the load changes were applied as in Fig. 3.18. In this case, the MGs did not become unstable due to the improved controller design. Fig. 3.19 (a) and Fig. 3.20 (a) show the low-frequency eigenvalues for the two MGs at their operating point. The transient responses associated with the pairs of eigenvalues in Fig. 3.19 (a) and Fig. 3.20 (a) are depicted in Fig. 3.19 (b) and Fig. 3.20 (b). These responses are calculated as:

$$y_i(t) = e^{\lambda_i t}.$$

In MG1, the response of ω_r can be represented as a linear combination of the time characteristics of the dominant eigenvalues $5-8$, as the participation matrix suggests in

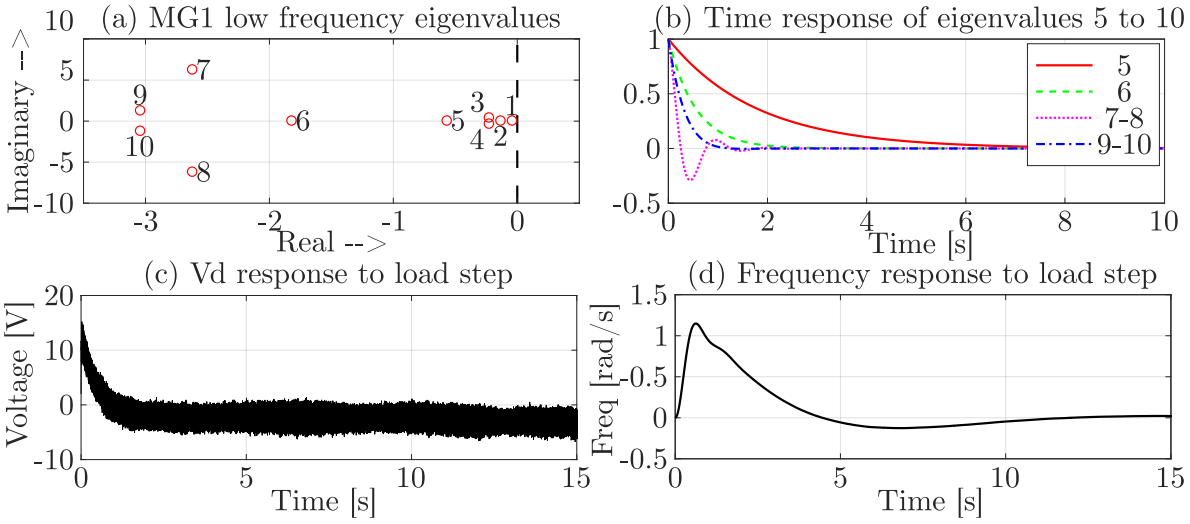

Figure 3.19: Response of MG1 in SC22 when the load decreased 1 kW with a recommended controller design. Comparison between the time responses obtained from the corresponding eigenvalues and the experimental setup.

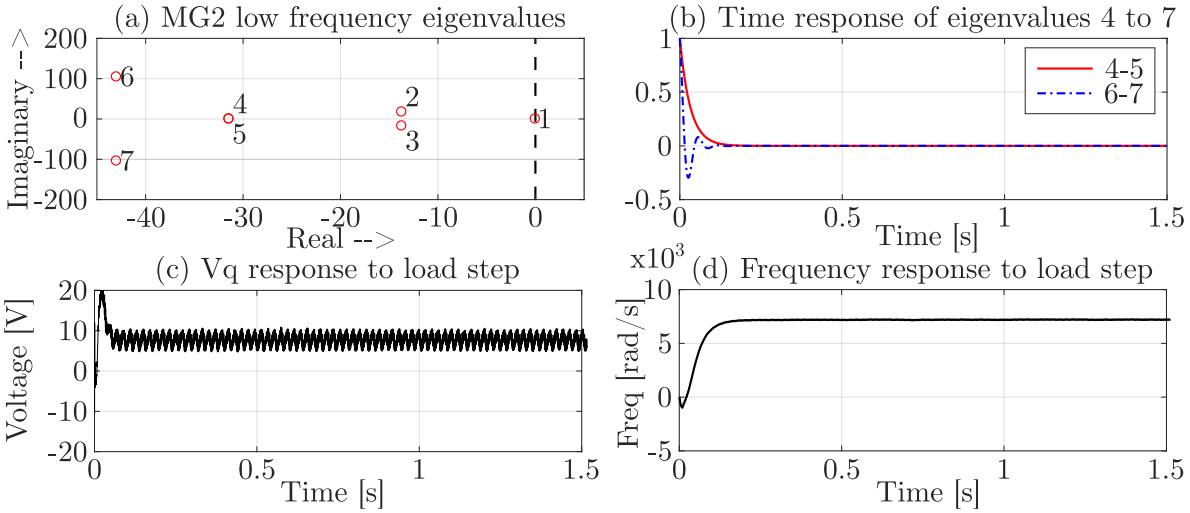

Figure 3.20: Response of MG2 in SC23 when the load decreased 1 kW, with the fine tuning. Comparison between the time responses obtained from the corresponding eigenvalues and the experimental setup.

Fig. 3.4. Also, the time response of v_d can be represented as a linear combination of the time characteristics of eigenvalues $9-10$. Similarly, in MG2 the responses of the voltage and frequency can be represented as a linear combination of the time characteristics of eigenvalues $6-7$ and $4-5$, respectively. These eigenvalues are mainly linked with the states of the voltage controller and the droop control, respectively, as shown in Fig. 3.8.

3.6 Discussion

3.6.1 Controller Design and Interactions

The analysis of participation factors confirmed that low-frequency modes are affected by the PLL states and, at the same time, by the mechanical states of the diesel gen-set and the states of the current and voltage controllers. The eigenvalue analysis revealed the PLL design is closely linked with the loading conditions and the design of the voltage and current controllers of the VSCs. In general, slow GFL converter current controllers, slow GFM converter voltage controllers and fast GFM converter current controllers limit the range of the PLL bandwidth in which the stability is guaranteed. Previous studies also showed that systems may become unstable when the PLL and the GFL converter DC-voltage controller have similar bandwidths [97, 98]. Therefore, as shown in the literature and in the results presented in this chapter, the design of the PLL is critical for the stability of MGs.

3.6.2 Additional Control Loops

The study did not reveal any relevant interactions between the PLL and the voltage control loop of the SG (excitation and AVR) unlike in the results reported in the literature for other types of excitation. The most likely cause is that a different excitation systems was considered. While other works use a static excitation system, the excitation system considered in this research is based on alternating current. Also, as reported in the literature, the DC-voltage controller may interact with the PLL and cause instabilities [91,97,98]. In order to study this interaction, a standard DC-voltage controller was implemented in the GFL converter [26]. Then, the response of v_{dPLL} was investigated in MG2, for different designs of the PLL and the DC-voltage controller. Fig. 3.21 shows the response of MG2 at SC21 with PLL bandwidth of (a) 10 Hz and (b) 20 Hz (close to the stability limit of the PLL). Fig. 3.21 (a) shows that v_{dPLL} exhibits an oscillation which is poorly damped in (b) when the the PLL bandwidth is close to instability. This seems to point at the PLL as one to blame. Results also show that the design of the DC-voltage controller only affects the oscillation slightly: the amplitude of the oscillation is amplified when the DC-voltage controller and the PLL have the same bandwidths. The fact that interaction between PLL and DC-voltage controller is stronger when they have similar bandwidths was already reported in [97, 98].

Further work is required to find out when and how the PLL interacts with other control loops (e.g., the governor of the SG) and, also, the interaction between DC-voltage controller and the rest of the MG controllers.

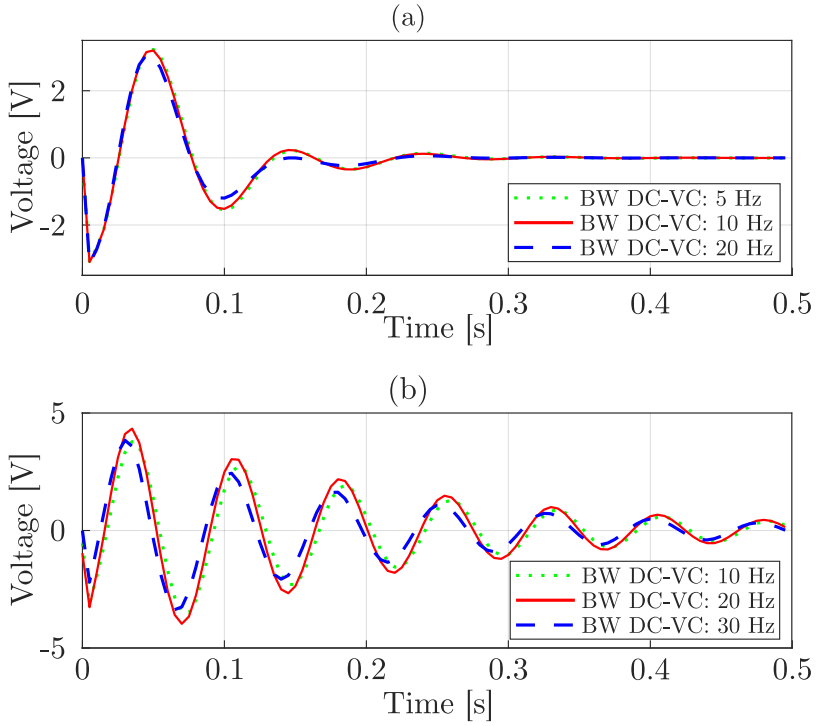

Figure 3.21: Response of MG2 (v_{dPLL}) when there is a 3 kW change of the load and the DC-voltage controller has different bandwidths. (a) SC21 with PLL bandwidth of 10 Hz and (b) SC21 with PLL bandwidth of 20 Hz (stability limit).

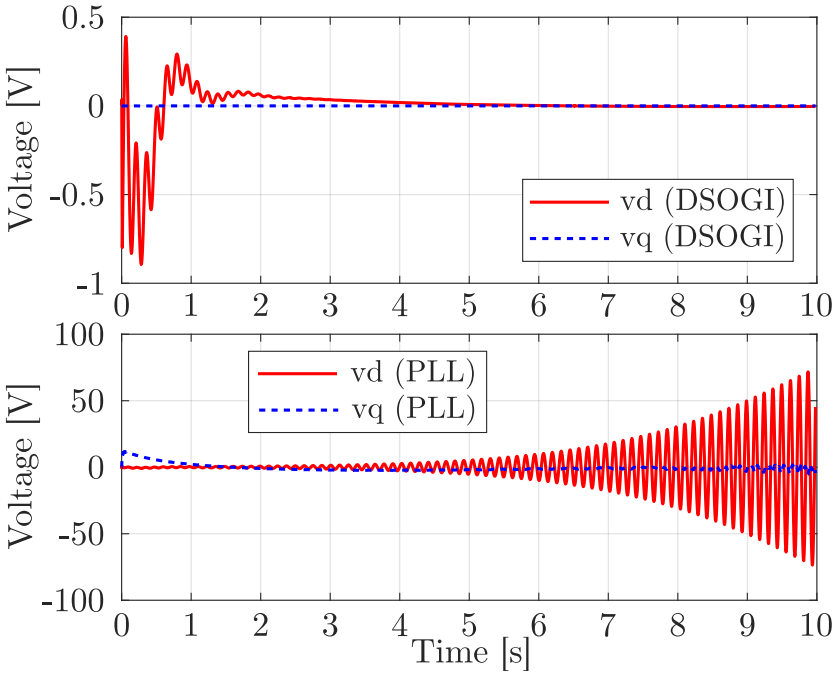

Figure 3.22: PCC voltage (in dq) of the non-linear model of MG1 (SC20), when there is a 1 kW change of the load, with and without a DSOGI-PLL.

3.6.3 Advanced PLL Structures

In order to study the effect of advanced synchronisation techniques, the DSOGI was implemented to calculate the positive sequence of the PCC voltage in the studied MGs [4]. For MG1 and MG2, the non-linear models were used to obtain the stability limits of the DSOGI-PLL bandwidth under different scenarios. Table 3.5 shows a comparison of the obtained stability limits for the PLL bandwidth, with and without the additional DSOGI. Both implementations have similar stability limits with only a slight improvement with the DSOGI. In some scenarios, like in SC20, the MG is stable for all values of the PLL bandwidth when the DSOGI is used. Stable operation was confirmed for MG1 in SC20, see Fig. 3.22. Therefore, advanced synchronisation techniques may offer extended stability limits, yet they have to be studied in more detail.

Table 3.5: Stability limits of PLL bandwidth under different scenarios ("−" means "limit not found").

MG	SC	BW_{CC}	PLL	PLL+DSOGI
MG1	SC20	120 Hz	18 Hz	−
MG1	SC8	120 Hz	3 Hz	3 Hz
MG1	SC8	160 Hz	4 Hz	4 Hz
MG1	SC8	250 Hz	8 Hz	10 Hz
MG2	SC21	250 Hz	1 Hz	−
MG2	SC18	160 Hz	13 Hz	13 Hz
MG2	SC18	260 Hz	−	−

3.7 Chapter Summary

In this chapter the dynamic interactions between a GFL converter with PLL and two types of GFM devices (diesel gen-set and droop-controlled VSC) in MGs have been studied. Firstly, detailed small-signal models for the two different GFM cases have been derived analytically and then the participation factor and eigenvalue analyses have been used to study the interactions between PLL and other controllers operating in the MG. All the theoretical developments have been validated experimentally.

Stability studies showed how the loading conditions and the design of current, voltage and frequency controllers of GFM and GFL converters and SGs affect the PLL stability limits. Based on these findings, design guidelines have been presented to help MG designers understand the interactions between GFL-PLL, GFM devices and other elements in MGs and to facilitate the correct configuration of the control system parameters. The experimental results and those obtained from the small-signal models showed a good match. Small deviations were found only for the parameter values that made the

system operate close to the maximum PLL bandwidth allowed. Finally, the experimental results obtained for the control system configured according to the proposed design guidelines confirmed that the dynamic response of MGs can be significantly improved by following the proposed design criteria.

Chapter 4

Design of the Primary Control of Electronic Power Converters to Shape the Frequency Curve after a Disturbance

This chapter presents a systematic method for updating the primary control parameters of grid-forming (GFM) converters in a microgrid (MG). This method allows to shape the MG frequency curve after a disturbance. The chapter is organised as follows. The MG topology, the converter controllers and an overview of the proposed methodology are presented in Section 4.1. Section 4.2 provides details about the methodology while its implementation is described in Section 4.3. Experimental results validating the methodology can be found in Section 4.4 and the conclusions are drawn in Section 4.5.

4.1 Overview

4.1.1 Application Scope

The MG in Fig. 4.1 is a simplified version of the low-voltage distribution benchmark network for the integration of distributed energy resources (DERs) proposed by Cigré [37]. This MG can either work in islanded mode as in Fig. 4.1 or connected to the main grid if the switch $BG - B0$ is closed. The system consists of a feeder and a transformer that feeds two resistive loads ($L1$ and $L2$). DERs such as photovoltaic (PV), wind generation and battery energy storage are connected to grid via grid-following (GFL) converters ($C4$) or by GFM converters ($C1, C2, C3$ and $C5$). All converters have an LCL output filter.

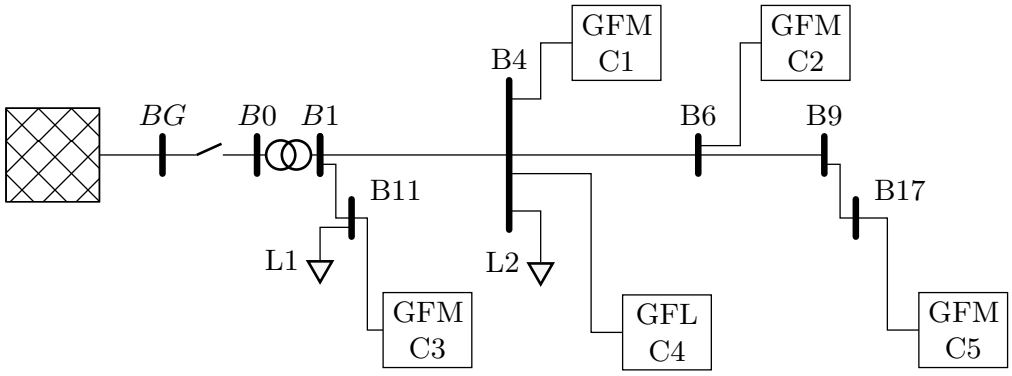

Figure 4.1: Single-line diagram of the MG studied in this chapter.

4.1.2 Control Overview

The GFL converter controls the active and reactive powers injected to the grid. For that purpose, it has a proportional-integral (PI) controller that regulates the current through the converter-side inductance of the LCL filter. A phase-locked loop (PLL) is used to synchronise the converter with the MG voltage at the point of connection.

GFM devices are equipped with an inner current loop and an outer voltage loop. The current loop is used to regulate the current through the converter-side inductance while the voltage loop is used to regulate the voltage at the alternating current (AC) filter capacitor. GFM converters also include a quasi-stationary virtual impedance loop that is applied on top of the voltage controller and facilitates the parallel connection of GFM devices (i.e., when forming the MG) [16]. Frequency and voltage magnitude control set points are internally generated according to [25]:

$$\omega = g_1(P), \;\; V = g_2(Q), \tag{4.1}$$

where ω is the output frequency of the converter, V is the voltage magnitude, P and Q are the active and reactive power measured at the converter output, and $g_1(\cdot)$ and $g_2(\cdot)$ are the desired GFM characteristics. For simplicity, conventional frequency and voltage droops are considered here, although other options could be also implemented [70]:

$$\omega = \omega_n - m_p\tilde{P}, \;\; V = V_n - n_q\tilde{Q}, \tag{4.2}$$

where ω_n and V_n are the no-load output frequency and voltage magnitude, and m_p and n_q are the droop gains. $\tilde{P}$ and $\tilde{Q}$ are the filtered active and reactive powers injected by the unit:

$$\tilde{P} = \frac{1}{s/\omega_c + 1}P, \;\; \tilde{Q} = \frac{1}{s/\omega_c + 1}Q, \tag{4.3}$$

where ω_c is the cut-off frequency of the filter. The equivalent inertia (H_i), measured in seconds (s), of the ith GFM converter can be calculated as [146]:

$$2H_i = \frac{1}{\omega'_{ci}m'_{pi}}, \tag{4.4}$$

being ω'_{ci} and m'_{pi} the pu values of the cut-off frequency and constant of the droop controller.

4.1.3 Methodology Overview

The aim of the proposed methodology is to adjust the controller parameters of a MG to achieve some specific metrics. In this chapter, metrics related to the transient response of the frequency of the MG center of inertia (COI) have been chosen. However, the proposed methodology is generic enough and can be also adapted to adjust other system metrics.

For simplicity, the frequency of COI is used as a measurement of the whole MG frequency. Borrowing the notion from conventional power systems, the COI frequency is defined as follows [147, 148]:

$$\omega_{COI} = \frac{\sum_{i=1}^{n} \omega_i H_i}{\sum_{i=1}^{n} H_i}, \tag{4.5}$$

where ω_i is the frequency of the ith converter and H_i was defined in (4.4). The desired transient response is designed by defining the nadir and/or the rate-of-change-of-frequency (ROCOF) of ω_{COI}, and changing DER primary controller accordingly.

Fig. 4.2 shows the flowchart of the proposed methodology. The relationships between nadir, ROCOF and the control parameters are determined by using the MG small-signal model, parametric sensitivities, and participation factors. Then, the parameters are modified based on these relationships. The new control parameters are validated according to stability and operational constraints. Since the methodology is based on the use of linear tools, MG control parameters should be modified by using small increments to prevent a large drifting from the original operating point. After an iterative search, the definitive values of the parameters are selected. In addition, as the system eigenvalues are placed far away from the imaginary axis during the iterative process, the system would be relatively robust against the changes of the operating point.

4.2 Details of the Methodology

In this section, the proposed methodology is explained. First, small-signal tools are described. Then, the relationships between COI dynamics, system eigenvalues and control parameters are derived. Finally, the iterative search for the control parameters is explained.

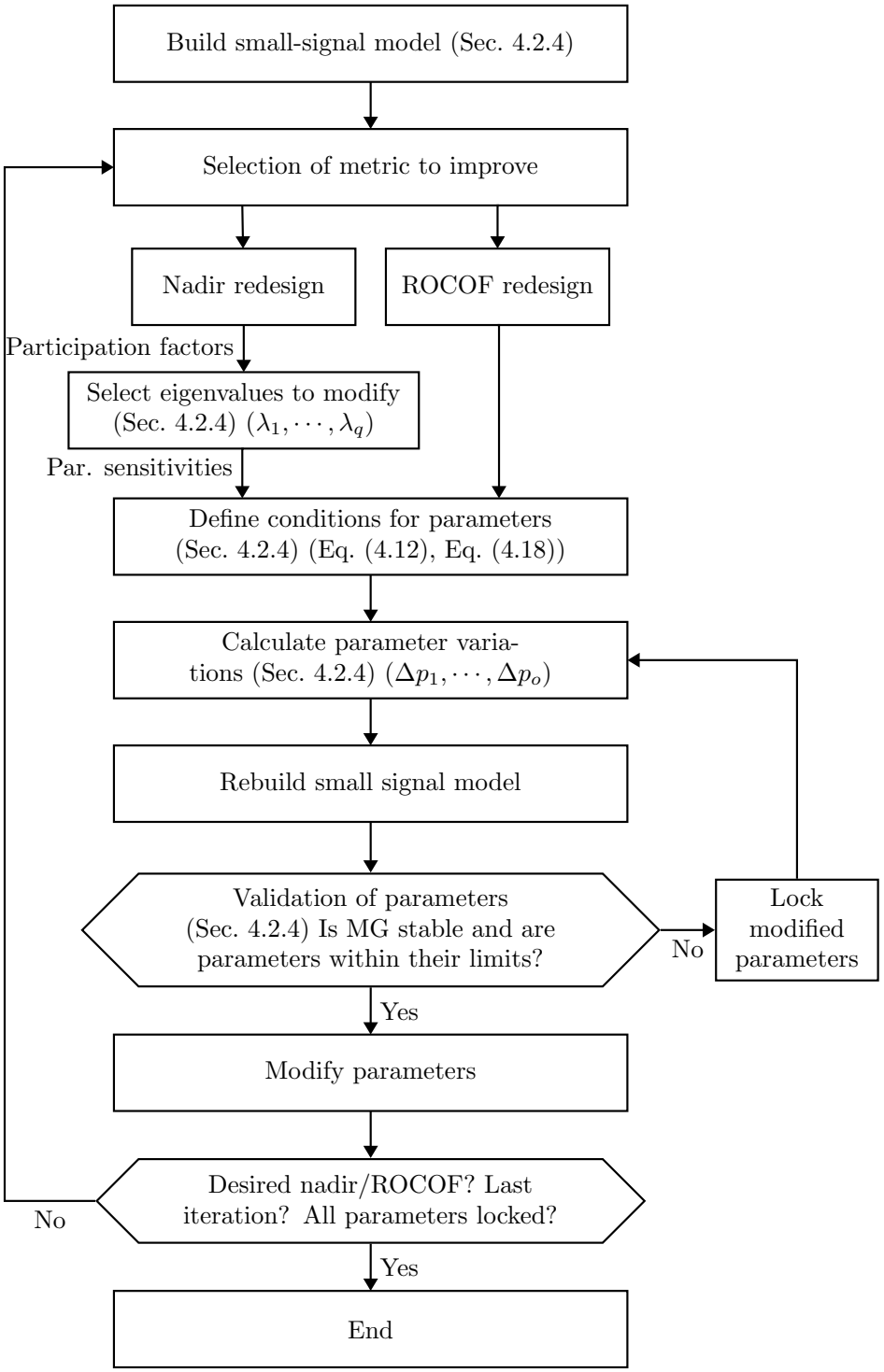

Figure 4.2: Flowchart diagram of the proposed methodology.

4.2.1 Small-Signal Analysis and Participation Factors

A small-signal model of the MG can be described as follows:

$$\begin{aligned} \left[\Delta \dot{x}\right] &= A\left[\Delta x\right] + B\left[\Delta u\right], \\ \left[\Delta y\right] &= C\left[\Delta x\right] + D\left[\Delta u\right], \end{aligned} \tag{4.6}$$

where Δx is the state vector, Δu is the input vector, Δy is the output vector, and A, B, C and D are the state-space matrices. The state-space model is derived considering a power variation in the load (ΔP_L) as the input and $\Delta\omega_{COI}$ as the output, following the methodology presented in [70]. The exact models of the MG devices can be found in Chapter 3 and Appendix A. The transfer function from a load step to ω_{COI} is used to study frequency dynamics.

The participation matrix (P_M) establishes the link between the state variables in (4.6) and the eigenvalues of A as explained in Chapter 3. The output $\Delta\omega_{COI}$ can be written as a function of the state variables and the inputs using (4.5) and (4.6):

$$\left[\Delta\omega_{COI}\right] = C_{COI}\left[\Delta x\right] + D_{COI}\left[\Delta u\right], \tag{4.7}$$

where the first term fully defines $\Delta\omega_{COI}$, so $D_{COI} = 0$. The participation vector of $\Delta\omega_{COI}$ shows which eigenvalues participate more in $\Delta\omega_{COI}$ and can be simply calculated as:

$$P_{COI} = C_{COI} P_M, \tag{4.8}$$

where P_M is the participation matrix of the whole system [42].

4.2.2 Eigenvalue Sensitivities

In this work, the eigenvalue sensitivities are used to explain how each control parameter participates in the dynamics of $\Delta\omega_{COI}$. Parametric eigenvalue sensitivities are defined as the derivative of a system eigenvalue with respect to a parameter [42, 108, 149]:

$$s_{ij} = \frac{\partial\lambda_i}{\partial p_j} = \psi_i \frac{\partial A}{\partial p_j}\phi_i, \tag{4.9}$$

where s_{ij} is the sensitivity of eigenvalue λ_i with respect to parameter p_j, ψ_i and ϕ_i are the left-row eigenvector and the right-column eigenvector associated to λ_i, respectively. Sensitivities are complex numbers that describe, in a quantitative manner, how eigenvalues move in the complex plane when a parameter is modified.

For small variations of parameter p_j (Δp_j), (4.9) can be expressed as:

$$\Delta\lambda_i = \lambda_i' - \lambda_i \approx s_{ij}\Delta p_j, \quad \lambda_i' \approx \lambda_i + s_{ij}\Delta p_j, \tag{4.10}$$

where λ_i' is the value of λ_i after applying Δp_j. This can be extended for variations of o parameters and q eigenvalues:

$$\begin{bmatrix}\Delta\lambda_1 \\ \vdots \\ \Delta\lambda_q\end{bmatrix} \approx \begin{bmatrix}s_{11} \\ \vdots \\ s_{q1}\end{bmatrix}\Delta p_1 + \cdots + \begin{bmatrix}s_{1o} \\ \vdots \\ s_{qo}\end{bmatrix}\Delta p_o. \tag{4.11}$$

One should note that (4.11) is an expression with complex numbers and it will contain $2q$ linear equations if all λ_i are complex numbers. As it will be shown in Section 4.3.2, real and imaginary parts of sensitivities have comparable magnitudes for the case studied in this work and both must be used to calculate eigenvalue variations. Other references only use the real parts when obtaining their results [108]. Still, the validity of this simplification depends on each specific application.

For a given operating point (with its specific eigenvalues and set of parametric sensitivities) the parameter variations that move eigenvalues $\lambda_1, ..., \lambda_q$ to their desired location $\lambda'_1, ..., \lambda'_q$ can be calculated by solving (4.11). Since (4.11) is only valid for small changes in Δp_j, this expression can only be used for small displacements of the eigenvalues. To calculate larger displacements, (4.11) can be applied iteratively until a solution is found.

4.2.3 Adjustment of Nadir and ROCOF of $\Delta\omega_{COI}$

Nadir

The transfer function of interest, representing the frequency dynamics, can be expressed as the sum of the contributions of each eigenvalue weighted by its corresponding residue [42]:

$$G(s) = \sum_{i=1}^{m} \frac{R_i}{s - \lambda_i}, \tag{4.12}$$

where R_i is the residue of $G(s)$ for λ_i. Both participation factors and residues have impact on the relationship between eigenvalues and $\Delta\omega_{COI}$ (see [149] for more details).

Both real and complex eigenvalue dynamics are studied here to understand their differences:

- *Effect of One Real Eigenvalue:* When the response of ω_{COI} is dominated by a real eigenvalue, the nadir is approximately $\Delta\omega_{COI}(\infty)$, because there is no overshoot, and can be calculated by applying the final value theorem [150]:

$$\begin{aligned} \Delta\omega_{COI}(\infty) &= \lim_{s\to 0} sG(s)U(s) = \\ &= \lim_{s\to 0} G(s) \approx \lim_{s\to 0} \frac{R_i}{s - \lambda_i} = \frac{R_i}{-\lambda_i}. \end{aligned} \tag{4.13}$$

  Therefore, to reduce the nadir in this case, the value of λ_i should be increased, that is, the eigenvalue should be moved to the left. This case is not very representative of a real system with machines, but it can happen in systems with power converters. In this case, the steady-state droop characteristic is directly related to the frequency nadir.

- *Effect of a Pair of Complex Eigenvalues:* In this case, the frequency nadir is linked with the overshoot of the second order system defined by the pair of complex eigenvalues, which is calculated as [150]:

$$\omega_{nadir} = \omega(0) - \Delta\omega_{COI}(\infty)e^{-\pi \tan \alpha}, \tag{4.14}$$

  where $\omega(0)$ is the frequency before the load variation and $\alpha = \arg(\lambda_i) - \pi/2$. Here, to reduce the nadir, α should increase (i.e., the damping of λ_i should be increased). This case is quite common in conventional power systems.

- *Application to the General Case:* In a general case where both real and complex eigenvalues participate in $\Delta\omega_{COI}$, it is more convenient to move real eigenvalues to the left and damp complex conjugated eigenvalues to reduce the nadir.

ROCOF

Qualitatively speaking, lower values of ROCOF can be obtained if GFMs converters provide a larger synthetic inertial response. However, the effect of control parameters on the ROCOF cannot be derived easily from eigenvalues (as in the case of the nadir). Therefore, to understand the effect of the control parameters on the ROCOF, the ROCOF expression has been rewritten in terms of the droop control parameters, as in (4.4). This representation of the ROCOF is equivalent to its standard definition, but adapted for power converters [146, 151]:

$$ROCOF = \frac{\Delta P_{Loss}\Omega_r}{2\sum_{i=1}^{n} S_i H_i} = \frac{\Delta P_{Loss}}{\sum_{i=1}^{n} \frac{1}{\omega_{ci} m_{pi}}}, \tag{4.15}$$

where ΔP_{Loss} is the power variation in the system that caused the frequency excursion, the denominator represents the kinetic energy of the system and n is the number of droop-controlled converters. In order to obtain an expression that considers parameter variations as variables like (4.11), ROCOF is presented as follows:

$$ROCOF = \frac{\Delta P_{Loss}}{\sum_{i=1}^{n} \frac{1}{\omega_{ci} m_{pi}}} = \frac{\Delta P_{Loss}}{\sum_{i=1}^{n} \frac{1}{\omega_{ci0} m_{pi0}}} \frac{1}{b}, \tag{4.16}$$

where ω_{ci}, m_{pi} correspond to the new droop parameters, ω_{ci0} and m_{pi0} correspond to the initial ones and b measures the change in the equivalent system inertia. Expression (4.16) can be linearised around the operating point to find a linear relation between

the new and the initial droop parameters. After the linearisation, the following expression is obtained:

$$Kb = \left[\Delta\omega_{c1}, \cdots, \Delta\omega_{ci}\right] \begin{bmatrix} \frac{K_1}{\omega_{c10}} \\ \vdots \\ \frac{K_i}{\omega_{ci0}} \end{bmatrix} + \left[\Delta m_{p1}, \cdots, \Delta m_{pi}\right] \begin{bmatrix} \frac{K_1}{m_{p10}} \\ \vdots \\ \frac{K_i}{m_{pi0}} \end{bmatrix}, \tag{4.17}$$

$$K_i = \frac{1}{\omega_{ci0} m_{pi0}}, \quad K = \sum_{i=1}^{n} K_i. \tag{4.18}$$

This equation is linear and explains how small changes of the droop parameters affect the ROCOF by means of b. As per (4.16), when b is greater than 1, ROCOF is reduced an vice versa. It can be used similarly to (4.11) to calculate control parameters.

4.2.4 Iterative Search of the Solution

When the MG power sharing conditions change, the controller parameters need to be recalculated to preserve the same frequency dynamics. Here, an iterative procedure is proposed to recalculate primary controllers. It combines all the tools presented above. A flowchart of the methodology is shown in Fig. 4.2. It is worth noting that the tools described above are widely used in the literature. The specific contribution of this chapter is in the proposed methodology, which combines all of them in order to control and set the dynamics of the MG. Nonetheless, equations (4.8) and (4.17) have been specially derived for that purpose. It has two main branches, one for setting the ROCOF and another one for setting the nadir. The steps are described below.

Small-Signal Modelling

First of all, a small-signal model of the MG is derived analytically [70, 152]. Since the adjustment of primary controllers to provide inertia is determined by the MG operator, it is reasonable to assume that device characteristics and the MG operating point are available for the parameter calculation. The MG operating point is calculated using a *Matlab-Simulink* model (alternative options for this task can be found in [153, 154]).

Selection of Target Eigenvalues

To adjust the nadir, the eigenvalues that define the transient of ω_{COI} should be modified, i.e., the eigenvalues with the largest participations in ω_{COI}. To this end, the participation factors of eigenvalues in ω_{COI} (P_{COI}) are calculated and normalised. Normalization consist on forcing that the sum of all elements in P_{COI} is 1 ($\sum^i P_{COIi} = 1$). That is, the sum of eigenvalue participations on ω_{COI} is 1. As explained in the previous sections eigenvalues with a low damping factor are also selected. More details on this implementation can be found when numerical results are presented.

Definition of Parameter Conditions

Equations (4.11) and (4.17) are used to modify the nadir and ROCOF, respectively. Sensitivities and the values of K and K_i (see (4.17)) are calculated in each iteration since they change with the operating point. For simplicity, sensitivities $\partial A/\partial p_j$ in (4.9) are calculated as $\Delta A/\Delta p_j$. Additional linear equations may be used to guarantee that certain parameters are modified simultaneously. For instance, in order to keep the same power sharing, the ratios between converter droops (m_{pi}) should be maintained (this will be explained later in more detail).

Calculation of Parameter Variations

In general, the number of variables to be calculated, which is the number of variables in (4.11) (or the number of variables in (4.17) for a design based on the ROCOF), will be larger than the number of equations. This means that the system will be underdetermined. To minimise the number of control parameters to be modified, the solution that minimises the least-square of solution Δp_j will be selected [155,156]. Also, since linearised models are used, only small variations of the control parameters will be used (1%).

Parameter Validation

After calculating the parameter variations, it must be verified that the system remains stable and that parameters remain within their technical limits. If the system is unstable, all parameters that were modified are fixed to their last feasible values. At this point, control parameter constraints may be introduced, for instance in primary controllers to guarantee sufficient bandwidth separation, to limit droop constants or restrict ω_{ci} range, among others. Constraints could be added to the original linear problem, although this would lead to a more complex formulation. Additionally, if one or more parameters are out of their permitted range, those parameters are also fixed to their last feasible value.

Iterating Condition

After updating the parameters, the algorithm must check whether the design goal (nadir or ROCOF) has been reached. This is done taking into consideration the new parameters in the small-signal model. As the variations of the parameters must be kept small, several iterations may be required until the solution is reached. Finally, the iterative process stops if either the nadir or the ROCOF reach their desired value, if there are no parameters that can be modified, or if the maximum number of iterations is reached.

4.3 Numerical Results

4.3.1 Case Study

The proposed methodology was applied to the MG shown in Fig. 4.1. The system parameters from the Cigré MG [37] were adapted to the lab facilities (see Appendix B and [143, 144, 157] for further information), resulting in the line and load parameter values provided in Table 4.1. The nominal apparent power of converters is 75 kVA for $C1$ and 15 kVA for the rest of them. The power reference of the GFL converter was set to 1 kW. Unless otherwise stated, current and voltage controllers of GFL and GFM converters have been designed with bandwidths of 250 Hz and 30 Hz, respectively. The PLL for GFL converters has a bandwidth of 1 Hz. Virtual impedances of 1 Ω and 10 mH were used to facilitate the parallel operation of GFM converters. Reactive power droop constants were adjusted to allow 2.5 % of voltage variation with an injection of the rated power. Low-pass filters (LPFs) of reactive power loops were designed so that they have the same cutoff frequency of those used for active power. The two different scenarios considered in this case study are shown in Table 4.2 together with the corresponding droop parameters of the active power controller. A load step change was applied to $L2$ to study the frequency dynamics of the MG.

The proposed methodology was applied to a case when a change of the power sharing between units is required while certain frequency characteristics should be retained at the same time. Initially, MG controllers are designed as in scenario SC1 where ω_{COI} exhibits the desired nadir and ROCOF. After a certain event, the power sharing between the units is readjusted and m_{pC1} is set to 5 %. The increment of m_{pC1} in this new scenario (SC2) increases the nadir and ROCOF of ω_{COI} with respect to those in SC1. Considering the new conditions, i.e., new power-sharing ratios between the units, the proposed methodology is applied to take the nadir and the ROCOF to their previous values. The application of the proposed methodology for SC2 is explained in detail in the following section, where the nadir will be adjusted and the modifications required to adjust the ROCOF will be explained. This case study has been defined to show how additional restrictions (while retaining the established power sharing) can be included in the methodology and to show their impact.

4.3.2 Application of the Proposed Methodology

Small-Signal Modelling

The small-signal model of the MG considered at a general operating point, has been derived analytically [70].

Table 4.1: Line and load parameters.

Line/Load	Nodes	R [Ω]	L [mH]
Line 1	B4-B6	0.075	0.3
Line 2	B6-B17	0.3	0.1
Line 3	B11-B4	1.075	0.3
Load 1	B11	17.78	–
Load 2	B4	26.67	–

Table 4.2: Definition of droop parameters and scenarios.

Conv.	Par.	SC1	SC2
$C1$	m_p (%)	0.25 % (75 kW)	0.5 % (75 kW)
	ω_c	5 Hz	5 Hz
$C2$	m_p (%)	0.5 % (15 kW)	0.5%(15 kW)
	ω_c	3 Hz	3 Hz
$C3$	m_p (%)	0.5 % (15 kW)	0.5 % (15 kW)
	ω_c	5 Hz	5 Hz
$C5$	m_p (%)	0.5 % (15 kW)	0.5 % (15 kW)
	ω_c	5 Hz	5 Hz

Selection of Eigenvalues to Modify

The participation factors of ω_{COI} are calculated by applying (4.8). For example, Fig. 4.3 shows their magnitude for SC2. Only the participation of the low-frequency eigenvalues is shown (lower than 7 Hz). Clearly, λ_{12} predominantly participates in ω_{COI}. To reduce the nadir, damping of poorly damped eigenvalues must be improved and real eigenvalues must be moved to the left. Fig. 4.4 (a) shows that the eigenvalues with lowest damping ($\zeta < 0,5$) are λ_6 and λ_8, and their conjugates. Therefore, the objective is to damp λ_6 and λ_8 and move λ_{12} to the left.

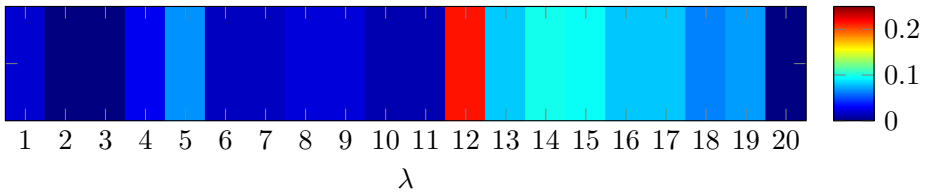

Figure 4.3: Eigenvalue participation on ω_{COI} in SC2.

Definition of Parameter Conditions

At this stage, (4.11) is used. The required λ'_{12}, λ'_6, λ'_8 are chosen to have a 1 % higher natural frequency and damping (if complex) than current λ_{12}, λ_6, λ_8. Furthermore, the

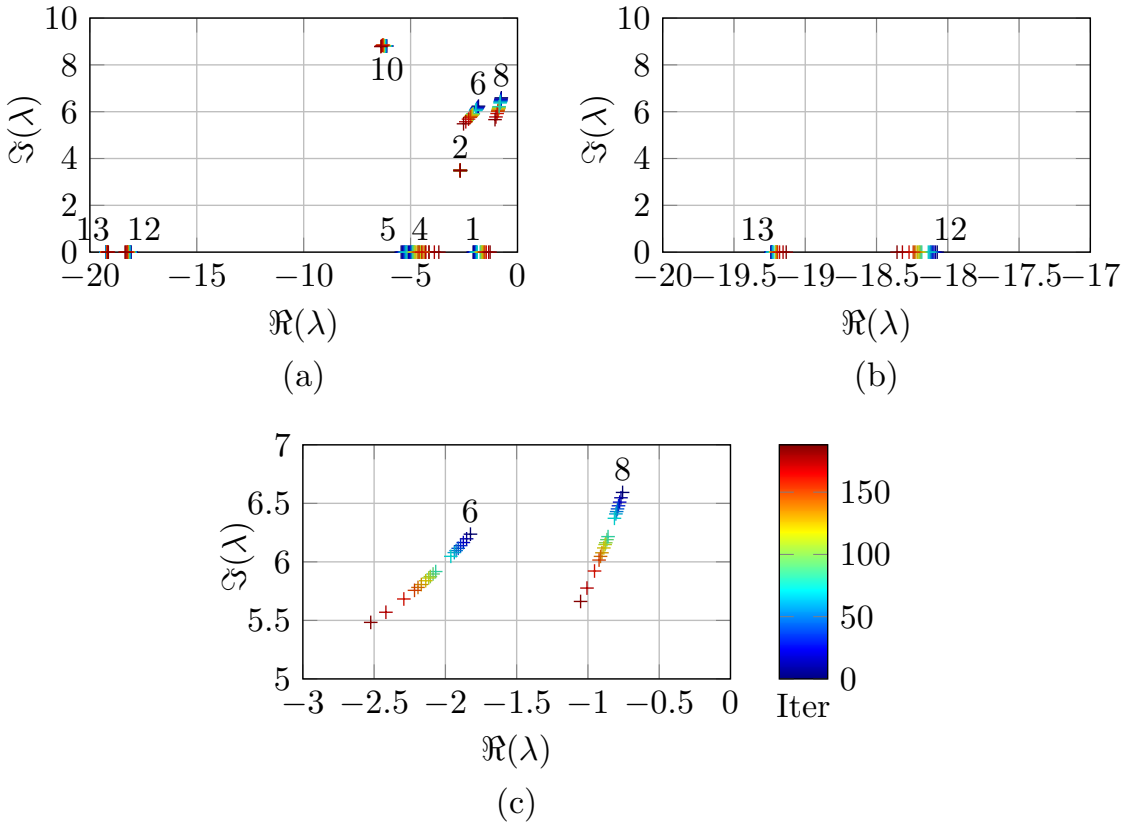

Figure 4.4: Eigenvalue loci for SC2 along the iterations when the nadir is reduced.(a) low frequency eigenvalues. (b) Zoom in eigenvalues λ_{12} and λ_{13}. (c) Zoom in eigenvalues λ_6 and λ_8.

following additional conditions are applied to maintain power-sharing ratios between units:

$$\begin{aligned} 5\Delta m_{pC1} - \Delta m_{pC2} &= 0, \\ 5\Delta m_{pC1} - \Delta m_{pC3} &= 0, \\ 5\Delta m_{pC1} - \Delta m_{pC5} &= 0. \end{aligned} \tag{4.19}$$

By adding these conditions, the ratio between the absolute droop coefficients is five despite the ratings of the units. In the case of ROCOF redesign, (4.17) must be applied considering the droop parameters and a value of b larger than one to reduce the ROCOF with each iteration. Since (4.17) represents a single equation, the least-square solution of (4.17) and (4.19) identifies the four droop parameters to modify. The parameter variations are calculated as detailed in the following section.

Calculation of Parameter Variations

Now, the system of equations formed by (4.11) and (4.19), that represent the relationship between eigenvalues and parameters, are solved to obtain the parameter variations. Fig. 4.5 shows the sensitivities of λ_{12}, λ_6 and λ_8 to droop (m_p, ω_c and n_q), virtual impedance (R_v and L_v), voltage controller (k_{pv} and k_{iv}) and current controller parameters (k_{pc} and k_{ic}). The parameters with the highest impact on the considered eigenvalues are droop and virtual impedance parameters. In some cases eigenvalues were also sensitive, to a lesser extent, to voltage-controller parameters but eigenvalues were not sensitive to current-controller parameters. Since the solution of (4.11) and (4.19) with the minimum norm is used, eigenvalues are relocated by modifying only droop and virtual impedance parameters (see Fig. 4.6).

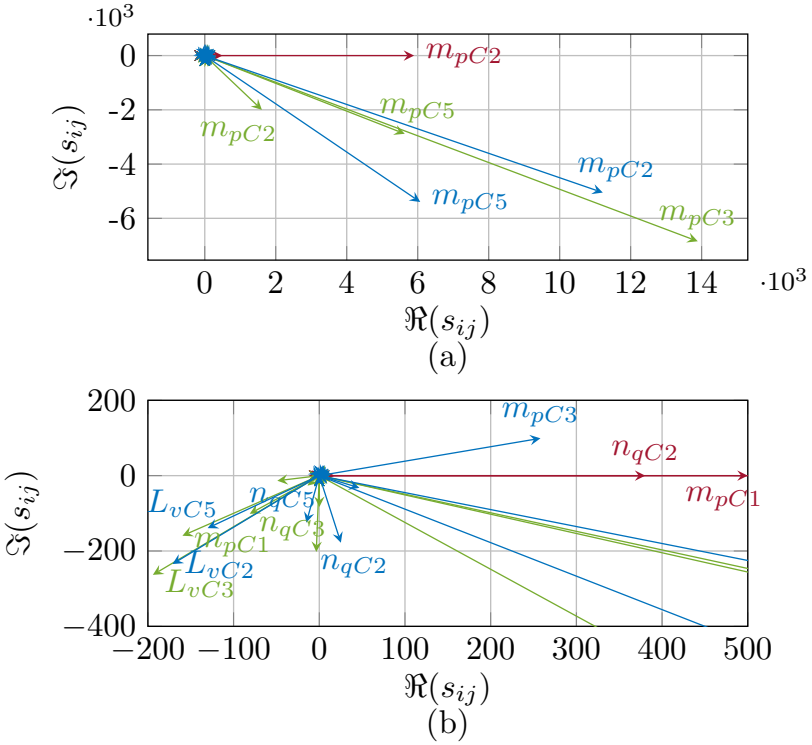

Figure 4.5: Parametric sensitivities of (red) λ_{12}, (green) λ_6 and (blue) λ_8, in SC2 at the first iteration expressed as vectors. (a) Parameters with the highest impact and (b) other parameters with high impact on λ_{12}, λ_6 and λ_8.

When the objective is to modify the ROCOF, (4.17) and (4.19) are solved and the four droop parameters are modified in each iteration. After the solution of (4.11) (or (4.17)) and (4.19) is found ($\Delta p_1, ..., \Delta p_o$), the new parameter values (p'_j) are calculated. A maximum variation of 1 % was considered to ensure the validity of the displacement prediction made by the sensitivities [108]. Firstly, per unit variations are calculated as $\Delta pu_j = \Delta p_j / p_j$. Then, the largest per unit variation ($\Delta pu_{max} = max(|\Delta pu_j|)$) is

computed and a variation of 1 % is assigned to that parameter. Finally, the values of all other parameters are calculated as follows:

$$p'_j = p_j \left(1 + \text{sign}(\Delta p_j) \frac{1}{100} \frac{|\Delta pu_j|}{\Delta pu_{max}}\right), \tag{4.20}$$

where p'_j denotes the new value for the current iteration of p_j and $|\Delta pu_j|$ is the modulus of the per unit variation of parameter p_j.

Fig. 4.6 shows the parameter values along the iterations for the studied case. Values higher than one indicate that the value of the parameter has increased and viceversa. The parameters that have been modified to change the nadir are m_{pC1}, m_{pC2}, m_{pC3}, m_{pC5}, n_{qC2}, n_{qC3}, n_{qC5}, L_{vC2}, L_{vC5} and kp_{vC3}. These are the parameters that affected λ_{12}, λ_6 and λ_8 the most, as shown in Fig. 4.5. Since (4.11) and (4.19) sum $5 + 3$ equations altogether, 8 parameters are modified simultaneously.

Parameter Validation

After calculation of the new parameter values in each iteration, their values are validated. If any of the parameters reaches its limit or if the MG becomes unstable for the new configuration, the parameters are blocked to their previous values. For example, in Fig. 4.6, when n_{qC3} reaches its lower limit at iteration number 70, its value is fixed to that value for the following iterations. From then on, the nadir is adjusted by modifying n_{qC5}, which had not been modified yet. Similarly, at iteration number 155, n_{qC5} hits its upper limit and kp_{vC3} is modified from then on.

Iterative Process

After each parameter modification, the small-signal model is recalculated to check if the design goals had been achieved. While there are parameters to be modified, the process

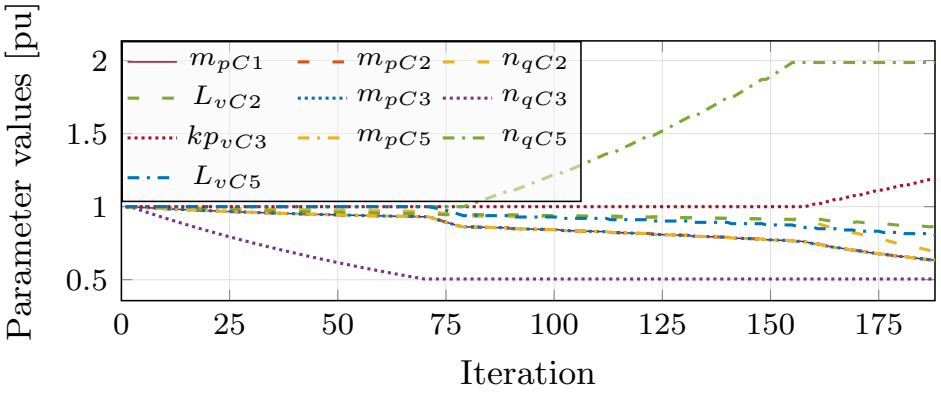

Figure 4.6: Per unit parameter values in SC2 when the objective is to reduce the nadir.

described is repeated until frequency dynamics metrics reach the required values. However, in order to avoid a long iterative process with too many parameters blocked, the maximum number of iterations was set to 500. The test carried out showed that the number of iterations to reach the desired nadir increases with the number of equations to solve. It is, therefore, recommended to avoid targeting too many eigenvalues.

4.3.3 Simulation Results

Fig. 4.7 shows the transient response of ω_{COI} for $SC1$ and $SC2$ when load-$L2$ was suddenly increased by 3 kW, before and after the recalculation of the control parameters. Fig. 4.7 shows that ω_{COI} features larger nadir and ROCOF in SC2 (in red) compared to SC1 (in green). After recalculating the controller parameters for adjusting the nadir (in orange), the nadir of ω_{COI} is the same as it was for SC1. This is mostly because of the change of the steady state frequency that is caused by the changes of droop parameters (m_{pi}). These were the parameters with the most significant impact on the selected eigenvalues.

Fig. 4.5 shows the polar representation of parametric sensitivities λ_{12}, λ_6 and λ_8. The direction of sensitivities is not the same as the required direction of movement of eigenvalues. Therefore, a combination of parameter adjustments is needed to move these eigenvalues. All this information is already taken into consideration in (4.11). Fig. 4.4 (b) and (c) show that λ_{12} moves to the left and that the damping of λ_6 and λ_8 increase. As a consequence, the nadir is reduced. Incidentally, other eigenvalues (apart from λ_{12}, λ_6 and λ_8) also move and, even though they have a low participation in ω_{COI}, they may become unstable. Thus, a minimum damping for all eigenvalues must

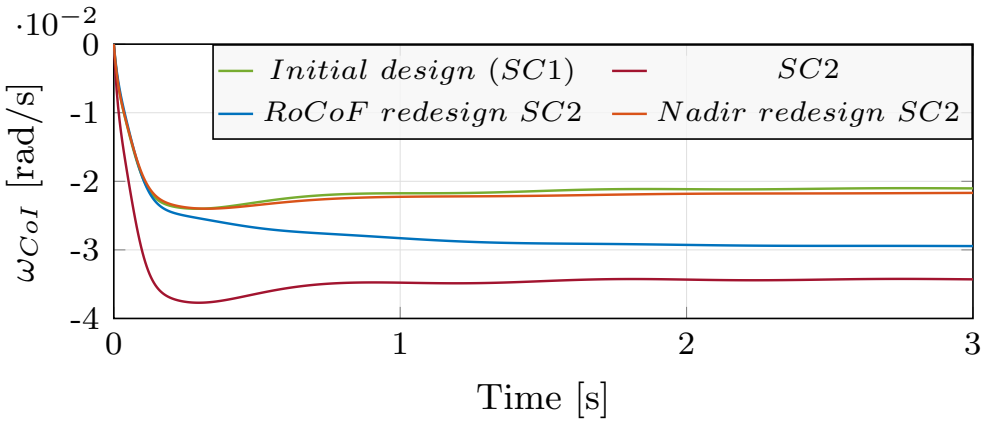

Figure 4.7: Transient response of ω_{COI} when there is variation of load L2. (green) Initial design of controllers in SC1. Results (red) with droop constrains applied (SC2), (blue) after modifying parameters to adjust ROCOF in SC2 and (orange) after modifying parameters to adjust nadir in SC2.

always be enforced. Furthermore, the power-sharing ratio between units is maintained constant along iterations since condition (4.19) is considered (see Fig. 4.6). The per unit variation of m_p is the same for all the GFM units. In this example, adding power-sharing restriction (4.19) simplifies the problem to solve by reducing the number of degrees of freedom. Nevertheless, this is not always the case.

Fig. 4.7 (blue) shows that the ROCOF of ω_{COI} (at $t = 0.1$ s), after the redesign, takes the original value of SC1. Since (4.17) and (4.19) sum $1 + 3$ equations, 4 parameters are changed in each iteration. Initially, m_{pC1} is reduced to increase the virtual inertia and (4.19) ensures that all droops are modified simultaneously to keep the same power-sharing ratio. One should notice that the reference frequency metrics might not be achievable with a feasible set of parameters. In that case, the algorithm will stop looking for a solution.

Effect of Inductive Loads

An additional test was conducted in order to test the algorithm under different types of loads. It was assumed, in particular, that all the loads in the system had an inductive part with $\cos\phi = 0.8$ in SC1 (instead of $\cos\phi = 1$). Then, the algorithm was executed and the objective was to set the nadir at 0.21 Hz. Fig. 4.8 shows the movement of the eigenvalues for $\cos\phi = 0.8$, marked with "o", and for $\cos\phi = 1$, marked with "+". It can be seen that for the scenario with $\cos\phi = 0.8$, the number of iterations needed is lower as the nadir was originally closer to the desired solution. Fig. 4.9 shows the transient response of the COI for the original case ($\cos\phi = 1$), before and after the redesign. In that figure, the results for the case of $\cos\phi = 0.8$ are also depicted. It can be seen that in both cases, the nadir after the redesign is 0.21 Hz.

Effect of the Operating Point

Variations of the operating point could lead to variations of the system eigenvalues (and then on the stability properties of the MG). In the proposed algorithm the system eigenvalues are placed far enough from the imaginary axis so that variations of the operating point do not substantially modify the system stability properties. Fig. 4.10 shows the system eigenvalues when the MG load changes between 8 kW and 26 kW with different zooms. Notice that the system eigenvalues remain far from the imaginary axis and then the system stability is not compromised. In addition, given that in all cases the algorithm places the eigenvalues in the stable half plane, we can trust that slow-enough changes will not make the system unstable [158].

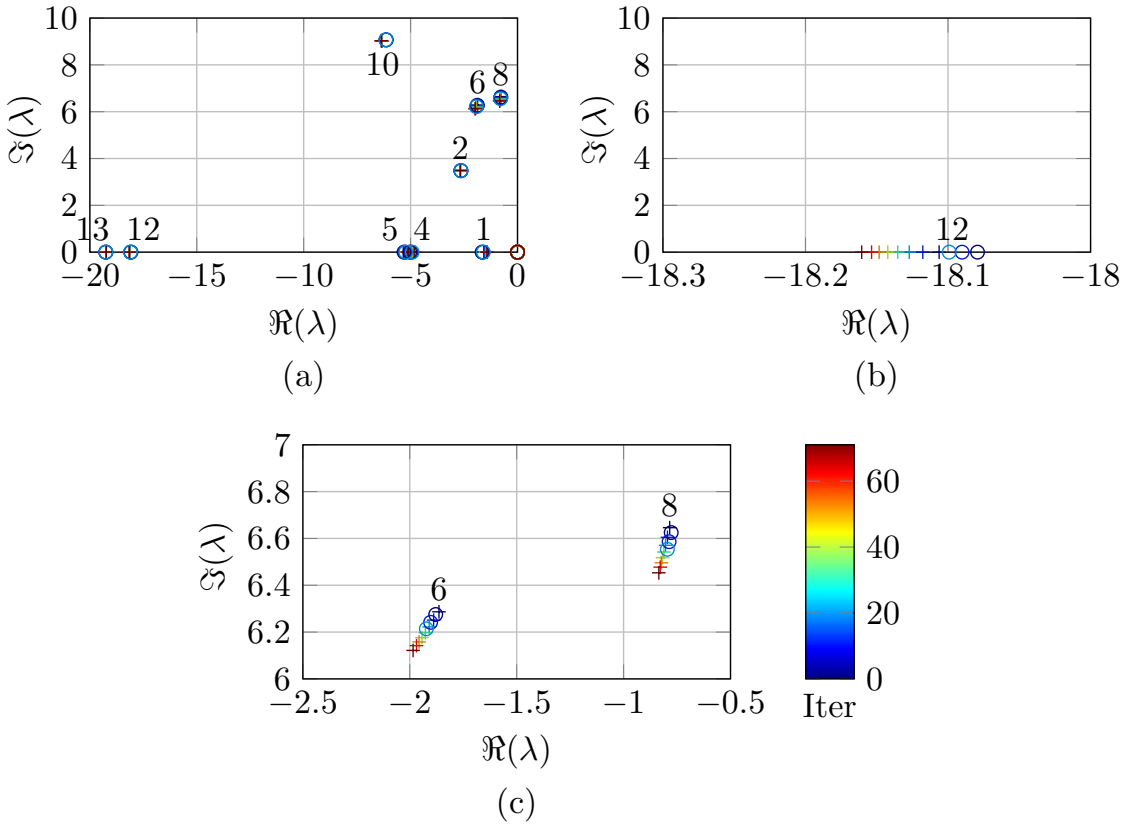

Figure 4.8: System eigenvalues of the MG for SC1, when load $\cos\phi = 0.8$ (o) and load $\cos\phi = 1$ (+).

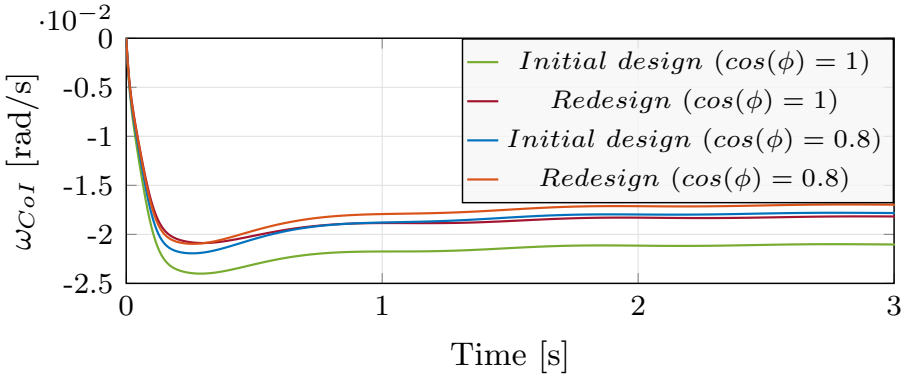

Figure 4.9: Transient response of the COI frequency in SC1, for load $\cos\phi = 1$ and load $\cos\phi = 0.8$.

4.3.4 Additional Considerations

Some extra features may be added to the algorithm presented above. For instance, if a specific ratio between controller parameters is required, additional expressions such as (4.19) could be implemented. In addition to that, if a simultaneous design of nadir

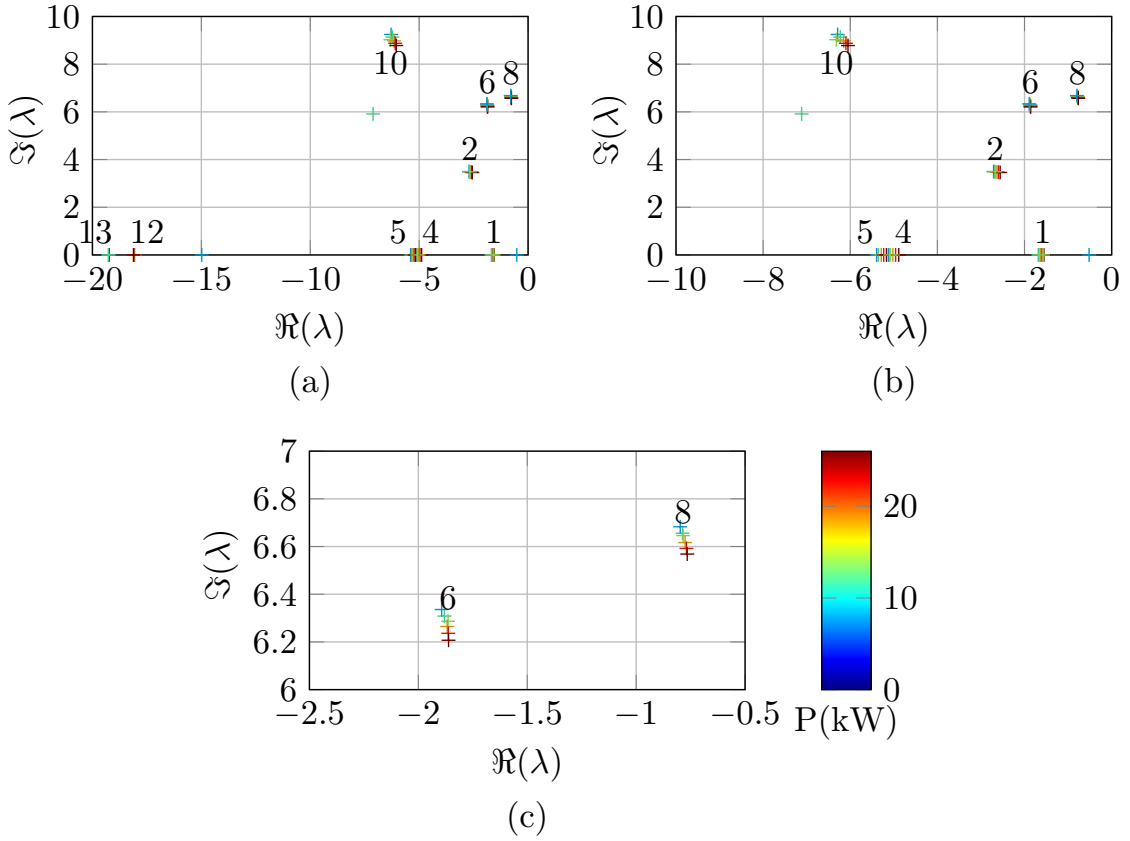

Figure 4.10: Eigenvalue loci when the load of the MG varies from 8 kW to 26 kW.

and ROCOF is required, (4.11) and (4.17) must be solved simultaneously. However, this objective might be difficult to achieve since these metrics might guide parameters in opposite directions. Therefore, in a case that the combined solution is not feasible, it is recommended to prioritise one of the metrics and tackle the design using only that metric. Results considering only one the metrics may be improved further using additional constrains as in (4.19).

The additional features described and the design of nadir and ROCOF simultaneously result in a system with a larger number of equations and the solution of the problem is more complicated. Accordingly, it is advised to limit the number of equations by limiting the number of eigenvalues to modify. When the nadir of ω_{COI} is redesigned in systems with second order dynamics, it is recommended to only modify the eigenvalue that participates the most in ω_{COI} and the lightly damped ones. Although this may change depending on the MG and its operating point, in a number of study cases used in this work, the algorithm found a solution to most of them. The only cases without a feasible solution were detected when an improvement of both nadir and ROCOF was attempted simultaneously.

4.4 Experimental Validation

4.4.1 Experimental Platform

Fig. 4.1 shows the implementation of the MG studied in this work in the smart energy integration lab (SEIL) [143, 144]. A 75 kVA voltage source converter (VSC) and four 15 kVA VSCs were used. One of the 15 kVA VSCs was used to implement the GFL control ($C4$). Two programmable resistive load banks were connected at nodes $B11$ ($L1$) and $B4$ ($L2$). L2 was configured to carry out a load step of 3 kW in order to measure frequency ROCOF (at $t = 0.1$ s) and nadir. Configurable impedances were used to replicate the MG topology. A diagram of the laboratory implementation is shown in Fig. 4.11.

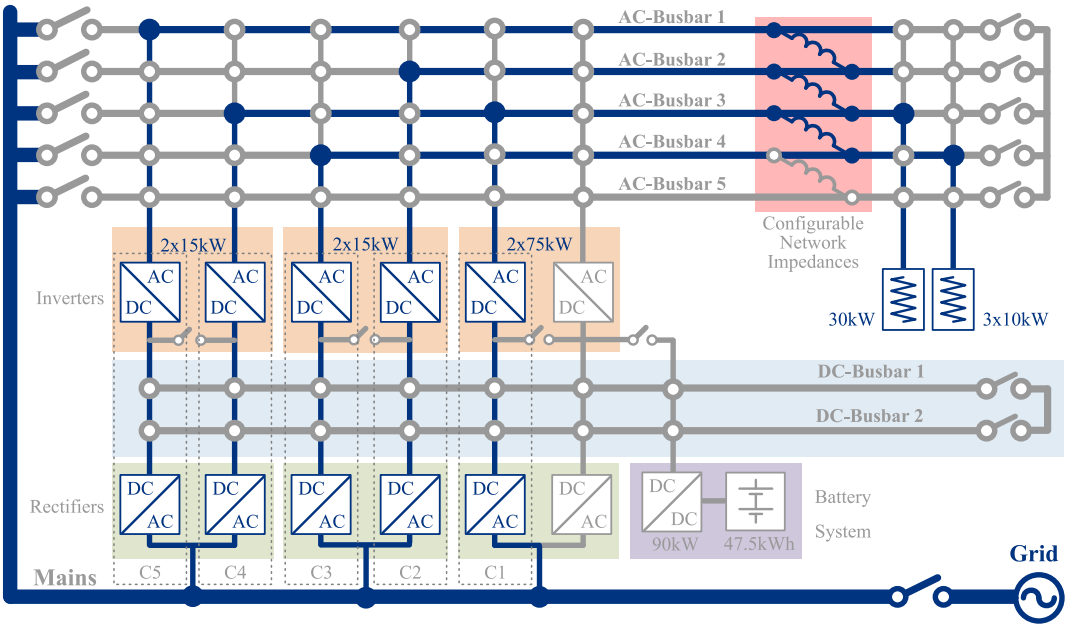

Figure 4.11: Electrical diagram of the connections made in the laboratory.

4.4.2 Experimental results

The analytical study was validated experimentally by performing the load steps described in Section 4.3.3 and by comparing the obtained experimental and analytical results for ω_{COI}. Fig. 4.12 shows the transient of ω_{COI} (both simulation and experimental results), for SC1 and SC2, before and after the recalculation for reducing (a) nadir and (b) ROCOF. The transient of ω_{COI} obtained in the experimental tests match well with the predicted results obtained from the analytical model. Fig. 4.12 (a) shows that after redesigning the controllers, the MG nadir for SC2 was reduced and it reached the original value obtained in SC1. Finally, Fig. 4.12 (b) shows the transient response

of ω_{COI}, for the case of ROCOF redesign. It clearly shows that the ROCOF was reduced and it now has the same value of SC1 although, understandably the shapes of the transients are not exactly the same. However, differences are relatively small.

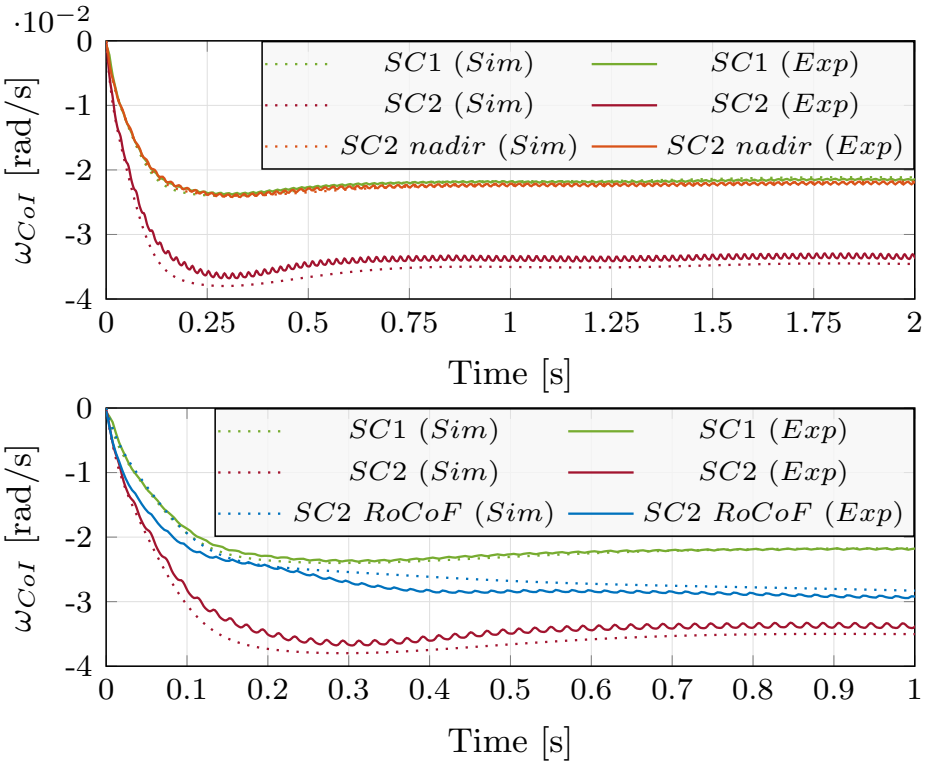

Figure 4.12: Transient responses of ω_{COI} obtained from (Sim) simulations and (Exp) experiments. A step variation is applied on the load $L2$. Test performed for the original scenario (SC1) (green), the scenario with droop constraints (SC2) (red), and SC2 with (orange) nadir and (blue) ROCOF redesigns.

4.5 Chapter Summary

This chapter has proposed a methodology for continuous management of two principal frequency stability parameters of a MG, namely ROCOF and nadir of frequency of centre of inertia (ω_{COI}). This is achieved by the recalculation of the controllers of the GFM converters in the MG. In the chapter, the methodology is applied only to converters with droop controller (for simplicity). However, it can also be applied to any other GFM controller type. When adjusting nadir, control parameters are modified by taking into consideration the parametric sensitivities of the eigenvalues that have most impact on ω_{COI}. In the case of adjusting ROCOF, control parameters are modified according to their contribution to ROCOF. The small signal tools used for the selection and tuning of parameters (eigenvalue analysis, participation factors and sensitivity)

illustrate the process of the control design in this chapter. Finally, analytical results of the proposed methodology were validated experimentally. It was demonstrated how the nadir and the ROCOF characteristics can be reestablished after a transient change of load.

The main contribution of this chapter is the proposed algorithm that ensures that both stability and operational constrains are met simultaneously. The algorithm uses an iterative search for the solution to meet the stability criteria. It has been found that parameters of droop and virtual impedance are the most important contributors to ω_{COI} according to the parametric sensitivities. Droop parameters have the highest impact on low frequency eigenvalues and, therefore, they are mainly used to adjust both ROCOF and nadir. In addition to that, the values of virtual impedances, that are typically omitted in frequency studies, were also used to modify nadir. For the ROCOF adjustment only droop parameters were used as they are directly linked with the system frequency response and the definition of ROCOF in the literature.

Another important remark is that despite the number of steps involved in the algorithm its computer implementation is rather simple. This is mostly because the algorithm mainly uses linear tools. Its main possible drawback is the complexity of the problem when a large number of restrictions is applied. It is, therefore, recommendable to set the number of restrictions to a minimum.

Chapter 5

Interaction between Primary and Secondary Controllers of Electronic Power Converters in Microgrids

In this chapter, interactions between primary and secondary controllers in microgrids (MGs) are studied by using participation factor and eigenvalue sensitivity analyses. The analysis conducted considers communication delays between primary and secondary control layers on the stability assessment of the MG. This chapter is organised as follows. The topology of the case study is described in Section 5.1. In Section 5.2, the small-signal analysis tools are presented. In Section 5.3, the eigenvalues and participation factors obtained for the test case are analysed. Finally, results are discussed in Section 5.4.

5.1 Application Overview

5.1.1 Application Description

The Cigré benchmark MG presented in Chapter 4 is also used in this study. Fig. 5.1 shows its single line diagram [37]. It is a low-voltage network operated as an islanded MG (with switch at $B0 - BG$ open). The system consists of a feeder originating from a transformer that feeds five resistive-inductive loads ($L1, L2, L3, L4$ and $L5$). Distributed energy resources (DERs) such as photovoltaic (PV), wind generation and storage are connected to the grid by either a grid-following (GFL) converter ($C4$) or grid-forming (GFM) converters ($C1, C2$ and $C3$). All the converters include an LCL filter. A secondary controller is applied to restore the frequency of the MG.

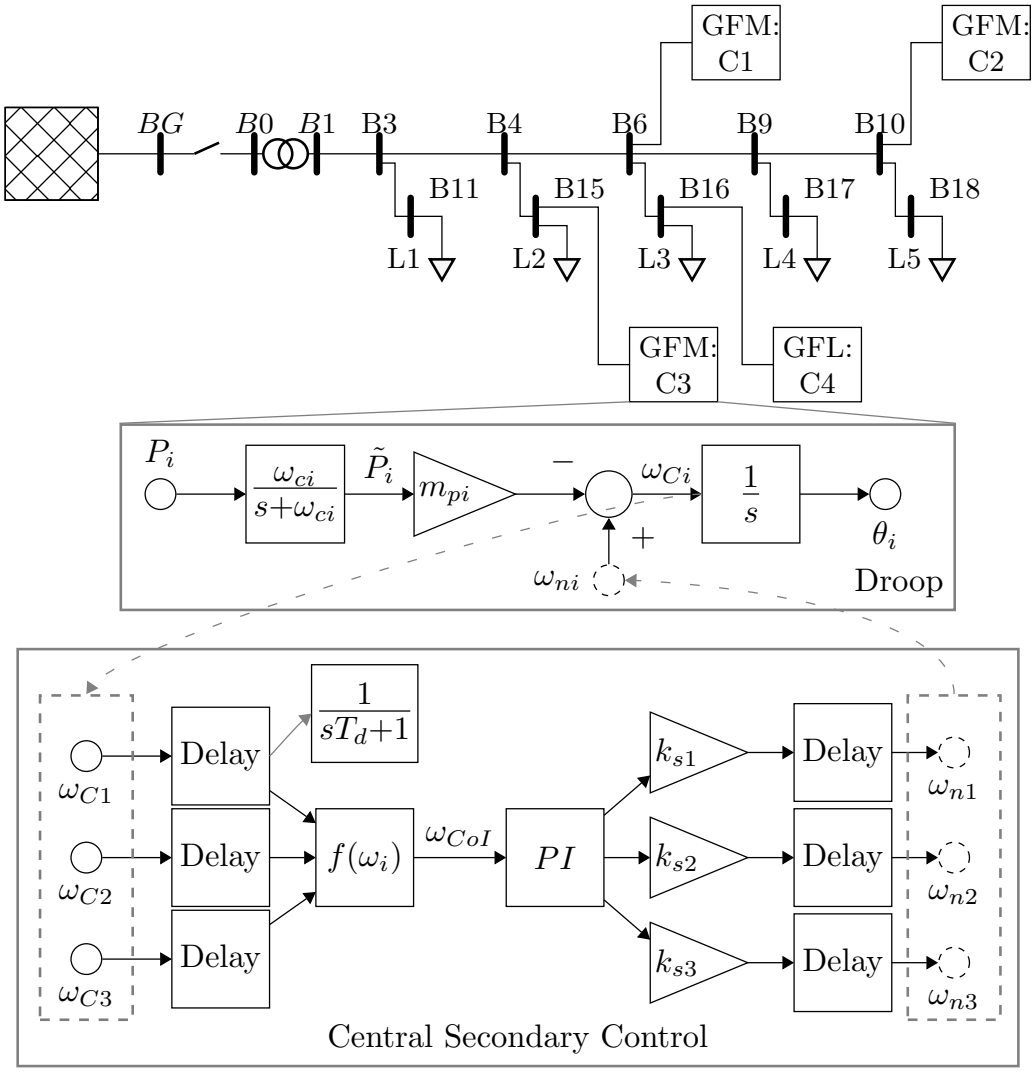

Figure 5.1: Single-line diagram of the MG and its control topology.

5.1.2 Control Overview

The GFL converter $C4$ manages the active and reactive power injected to the grid by using a closed-loop control of the current through the converter-side inductance (L_i) of the LCL filter [26]. A phase-locked loop (PLL) is used to synchronise the converter output voltage with voltage of the connection point [26]. The control topology of the GFM converter consists of an inner current control loop that controls the current of the converter-side inductance (L_i) and an outer voltage loop that controls the voltage across the ac capacitor (C_d) [70]. Frequency and voltage set points are internally calculated by using conventional active and reactive power droops that also ensure the power sharing between the units [14, 70]. Although they have been presented in previous chapters,

they are recalled here for convenience:

$$\omega_{Ci} = \omega_{ni} - m_{pi}\tilde{P}_i, \;\; V_i = V_{ni} - n_{qi}\tilde{Q}_i, \tag{5.1}$$

where ω_{ni} and V_{ni} are the no-load frequency and voltage magnitude of each droop, and m_{pi} and n_{qi} are the droop slopes. The signals $\tilde{P}$ and $\tilde{Q}$ represent the filtered versions of the active and reactive powers injected by the unit. In the Laplace domain, these signals can be represented as follows [70]:

$$\tilde{P}_i = \frac{1}{s/\omega_{ci}+1}P_i, \;\; \tilde{Q}_i = \frac{1}{s/\omega_{ci}+1}Q_i, \tag{5.2}$$

where ω_{ci} is the cutoff frequency of the low-pass filter (LPF) and P_i and Q_i are the measured active and reactive powers.

Droop controllers introduce voltage and frequency deviations in steady state. In this work, a central secondary controller is used to restore the frequency of the MG (Fig. 5.1). It consists of a proportional-integral (PI) controller that keeps the frequency of the center of inertia (ω_{CoI}) equal to 50 Hz. For calculating ω_{CoI}, the internal frequencies of the GFM converters (calculated by the droop controllers as indicated in Fig. 5.1) are sent to the secondary controller via communication channels. The command of the PI controller is multiplied by constants (k_{s1}, k_{s2} and k_{s3}) that are used to ensure an adequate power sharing during the frequency restoration process and the results are then sent to the GFM devices. The impact of these constants is studied later in this chapter. In this implementation, the secondary controller command adjusts the value of ω_{ni} of the droops (in (5.1)), thus shifting up or down the droop characteristics. The communication delays associated with the central secondary control are modelled using first-order LPFs for simplicity. For a more realistic representation of communication delays, stochastic models can be used [116]. For simplicity, both primary and secondary controllers have been presented as continuous-time control systems, however, in real applications they are typically implemented using discrete-time control systems. Controller sampling time in real applications depends on the required control speed and available communication bandwidth.

5.2 Small-Signal Modelling and Analysis Tools

In this study, the small-signal stability of the MG is studied as well as the impact of system parameters on it. The small signal model of the MG is represented as in [42,70]:

$$\Delta\dot{x} = A\Delta x + B\Delta u, \tag{5.3}$$

$$\Delta y = C\Delta x + D\Delta u, \tag{5.4}$$

where Δx, Δu and Δy are the state, input and output vectors, respectively, and A, B, C and D are the state-space matrices of the system. In this MG, Δx comprises

the states of the dynamic equations of the lines, loads, LCL filters, local controllers of the converters and the states of the secondary controller. In the GFM converters, the most important states are those related to the droop LPFs (p_s and q_s), the angle δ_i between converters and the states of the voltage and current controllers (ϕ_{dq} and γ_{dq} respectively). The secondary controller states are those of the LPFs that are used to model the delays (see Fig.5.1) and the state of the PI controller. They are denoted as m_{wsc} and c_{wsc} (measurement and command delay respectively) and w_{sc} (PI state). A detailed description of the system states can be found in Chapter 3 and in [152].

The MG small-signal model can be derived analytically from the non-linear equations that define the MG dynamics or by using software tools such as *Matlab*. In this case, it was derived following the methodology proposed in [70, 152].

MG small-signal stability has been investigated using eigenvalue and participation-factor analyses. These tools have been widely used to study the stability of both conventional power systems and power systems with high penetration of converter interfaced generation [42, 70]. The eigenvalues of the linearised model describe the oscillation modes of the power system, while participation factors (f_{ki}) measure the relationship between eigenvalues and the states of the MG [42]. Participation factors are defined as in Chapter 3, in (3.34). In the following sections, the eigenvalue loci and the participation factors are shown for different test cases.

5.3 Analytical Study

5.3.1 Test System Description

In this section, the parameters of the MG are provided. Line parameters are defined as in Cigré benchmark [37]. Loads $L1$, $L2$, $L3$ and $L5$ absorb 12 kVA ($\cos\phi = 0.9$). The nominal apparent power of the converters is 15 kVA. The LCL filter parameters are defined as in Chapter 3. The GFL converter power reference is 10 kW. Unless specified otherwise, the current controllers and voltage controllers (of the GFL and GFM converters) have been designed to have bandwidths of 350 Hz and 25 Hz, respectively. The PLL of the GFL-voltage source converter (VSC) has a bandwidth of 1 Hz. Unless otherwise indicated, droop LPFs are designed to have cutoff frequencies of 3 Hz and droop constants of 1 % for the frequency and 2.5 % for the voltage. Voltage and droop controller parameters are modified in the following section to study the interaction with the secondary controller. The secondary controller is designed to have a bandwidth of 0.5 Hz. The cutoff frequency of the LPFs that emulate the delays is 10 Hz and the constants for power sharing between units are all set equal ($k_{s1} = k_{s2} = k_{s3} = 1$). The impact of these constants on the stability is studied in this chapter. Their impact on the power sharing, the coordination of devices and the operation of the MG is addressed in Chapter 6.

5.3.2 Participation Factor and Eigenvalue Analyses

Fig. 5.2, Fig. 5.3 and Fig. 5.4 show the moduli of participation factors of the MG under study. Participation factors are multiplied by 100 so they show the participation in percentage. The scale has been adjusted to have a maximum of 50% in order to have a better view of participation factors with smaller values. Eigenvalues are ordered according to their natural frequency. High-frequency eigenvalues (higher than 110 Hz) and states with high-frequency dynamics (electrical states of lines, loads and LCL filters) are not shown in the figures since the chapter focuses on the low frequency dynamics of the secondary controller. Fig. 5.2 corresponds to the scenario described in the previous section. Fig. 5.3 corresponds to a scenario where the secondary controller is faster than in the initial case (bandwidth is 3 Hz while cutoff frequency of the LPFs that model the delays is 65 Hz). The secondary controller is designed in this way to study its interaction with primary controllers when they all work in similar ranges of frequency. Fig. 5.4 corresponds to the scenario in Fig. 5.2, but the secondary controller parameters that shape power sharing are different ($k_{s_1} = 1,\ k_{s_2} = 1.25,\ k_{s_3} = 1.5$).

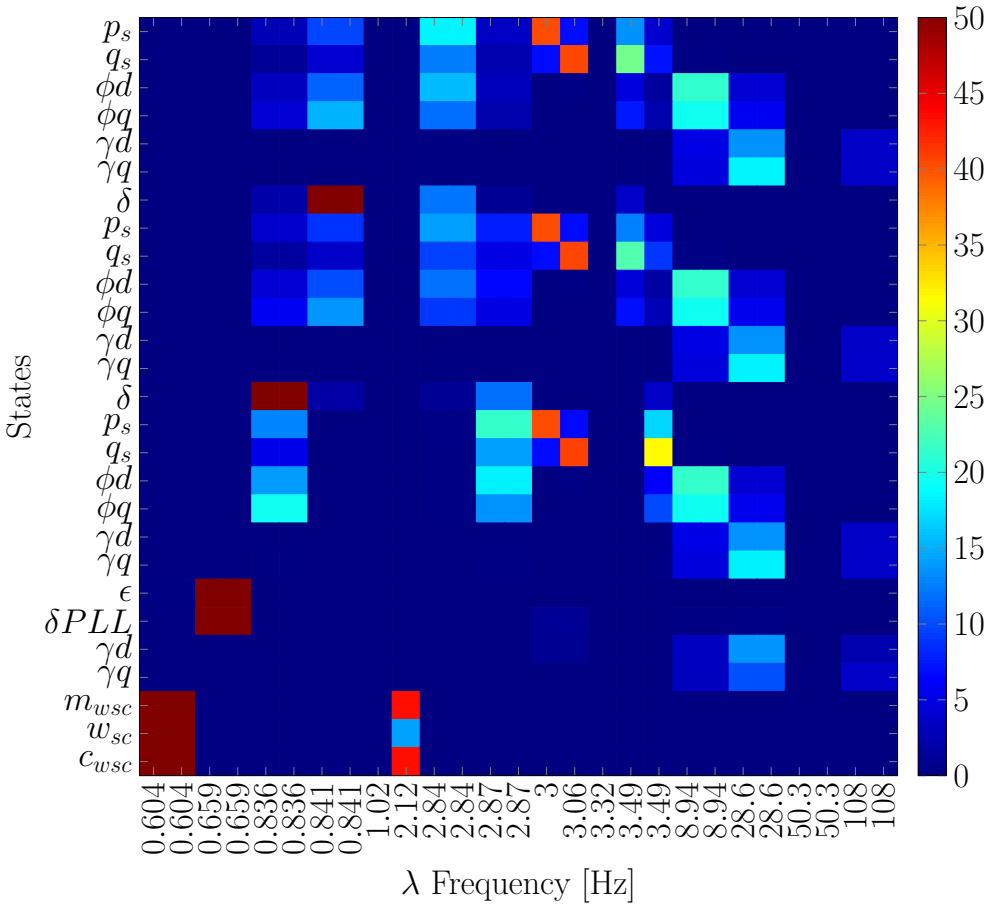

Figure 5.2: Participation factors of the MG under nominal conditions.

Fig. 5.2 shows that the modes that participate in the states of the secondary controller (m_{wsc}, c_{wsc} and w_{sc}) have frequencies of 0.604 Hz and 2.12 Hz, approximately. These modes do not participate in any other state in the MG. In addition, the modes related to the primary controllers like PLL, droop, voltage and current controllers ($0.659 - 0.841$ Hz, and $2.84 - 108$ Hz) do not participate in the secondary-controller states. This means that, in this case, primary and secondary controllers are decoupled. That is, in general, a desired feature of cascaded controllers. In the following part of this section, the effect of different design options for primary and secondary controllers are studied.

Fig. 5.3 shows the participation factors of the MG when the bandwidth of the secondary controller is 3 Hz. A comparison with the previous scenario shows that primary and secondary controllers are more coupled. The eigenvalues that participate in the states of the secondary controller (3.99 Hz and 14 Hz) also participate, to a lower extent, in the states of primary controllers as explained in the following lines. Modes with natural frequency of 3.99 Hz participate slightly in state p_s (0.5 %). Eigenvalue with natural frequency of 3.12 Hz mainly participates (15-20 %) in states p_s and q_s of the droop, but it also participates (3-9 %) in the states of the secondary controller.

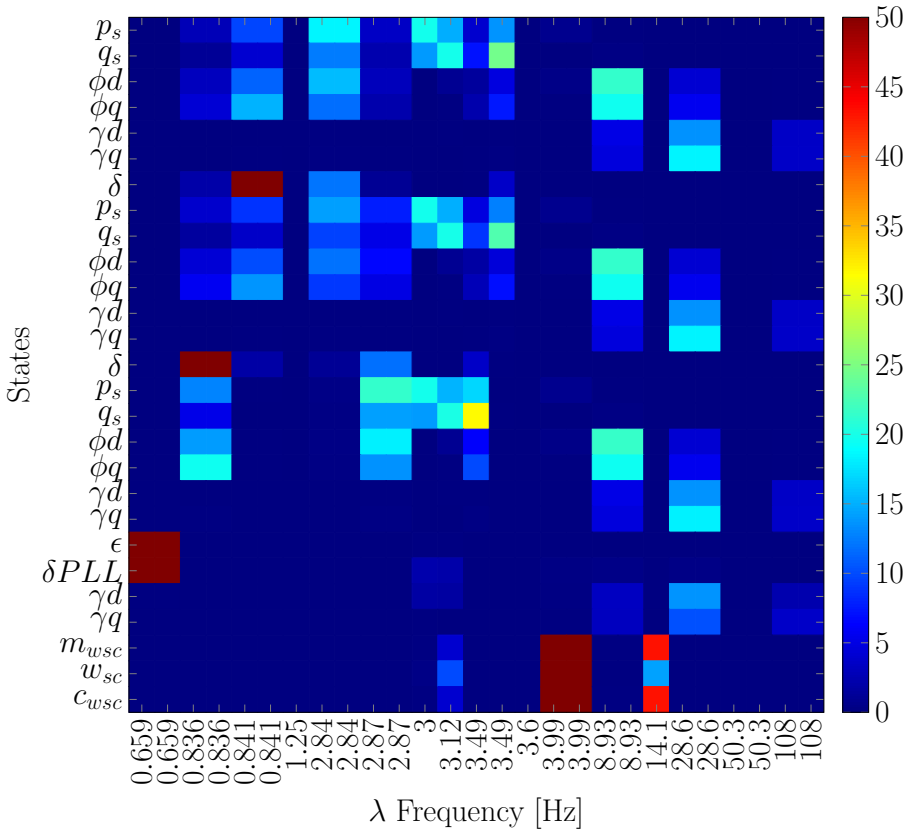

Figure 5.3: Participation factors considering primary and secondary controllers with similar speeds. Bandwidth of secondary controller is 3 Hz and cutoff frequency of droop filters is 3 Hz.

Therefore, it seems that the proposed secondary controller only interacts with the droop controllers if both are designed using similar speeds, that is, the bandwidth of the secondary controller is similar to the cutoff frequency of the droop filter. Moreover, voltage controllers and secondary controllers did not exhibit any interaction for the secondary controller speeds studied.

In the scenario presented in Fig. 5.4, different values were selected for the parameters k_{si} of the secondary controller. This resulted in primary and secondary controllers being now more coupled than in the previous cases. The 0.672 Hz eigenvalues mainly participate in the states of the secondary controller (m_{wsc}, c_{wsc} and w_{sc}) to a 50-90 %, in the droop states (p_s, q_s and δ) to a 4 % and in the voltage controller states (ϕ_d and ϕ_q) to 2 %. It should be pointed out that the participation factors sum more than 100. This is due to the fact that participation factors sum (not their moduli) was forced to be one as they were normalised. Also, 2.17 Hz eigenvalues participate in the states of the secondary controller (15-42 %), in the droop states (2 %) and in the voltage-controller states (0.3 %). Moreover, the eigenvalues with a frequency of 0.776 Hz that are highly related to the droops have a small participation in the states related to the

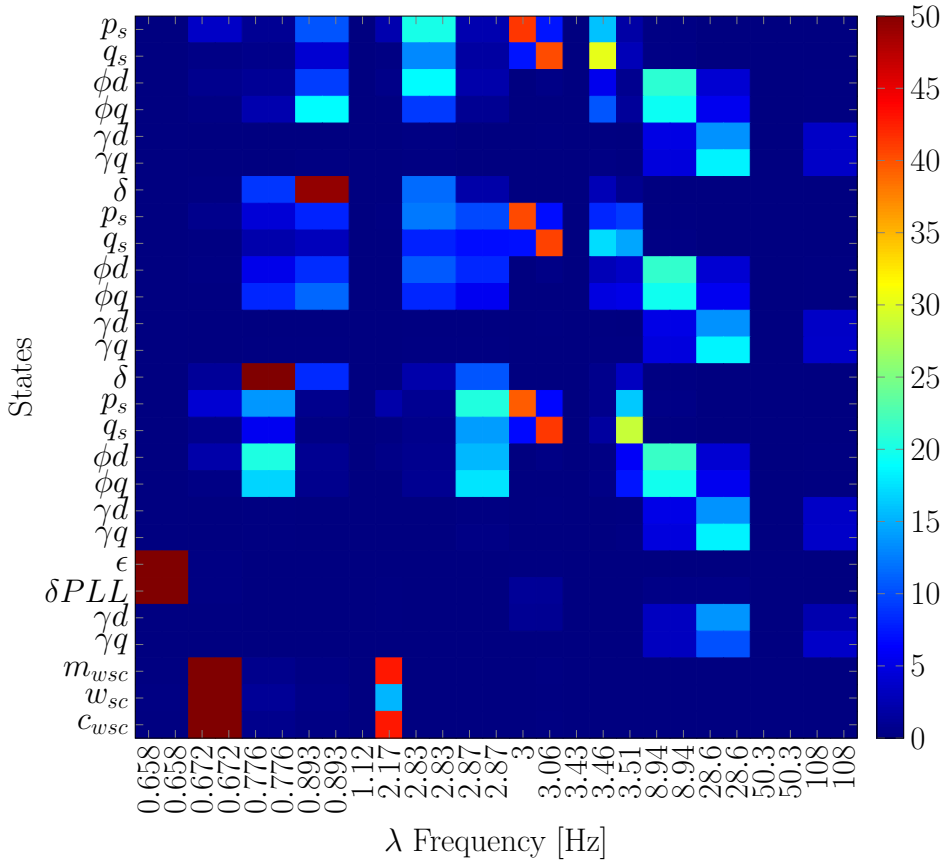

Figure 5.4: Participation factors considering unequal power-sharing parameters ($k_{s1} \neq k_{s2} \neq k_{s3}$).

secondary controller. This shows that the selection of the k_{si} plays an important role in the design of secondary controllers. The more similar the values of these parameters are, the weaker the interaction between primary and secondary control is. For very different k_{si}, the small-signal model is not valid since the angle deviations δ_i of local reference frames are not close to those of the operating point. Therefore, this scenario is not studied, but it may be of interest for further research.

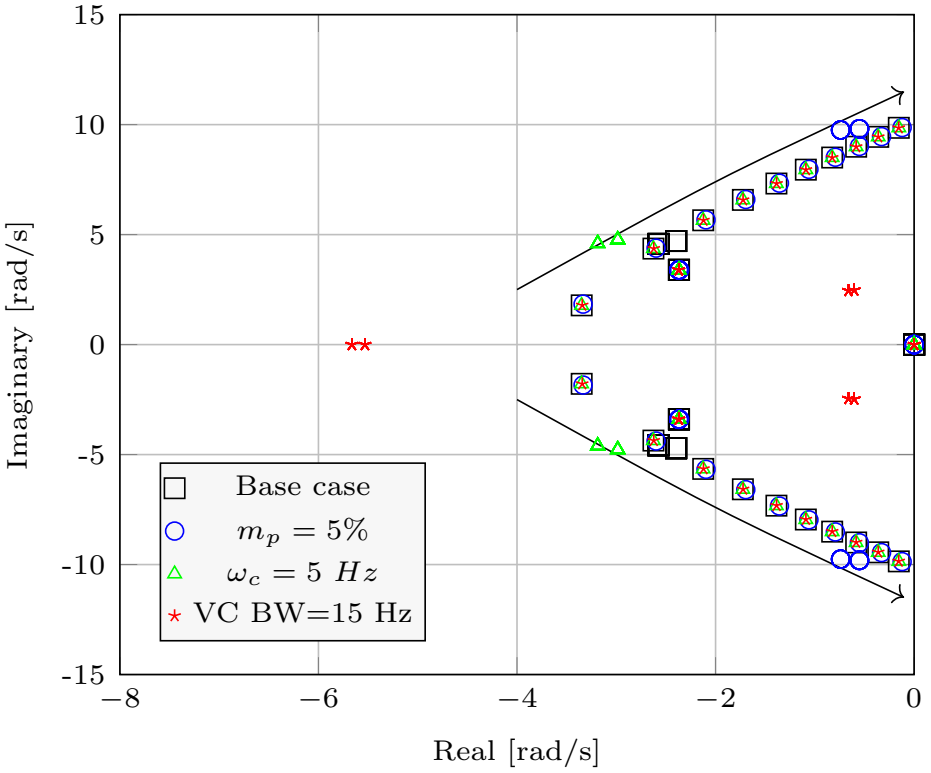

Figure 5.5: Low-frequency eigenvalue loci when k_i increases, for different primary controller designs ($m_p = 5\%, \omega_c = 5Hz$ and voltage control bandwidth of 15Hz). VC BW meaning "voltage control bandwidth".

Coupling between primary and secondary controllers will now be discussed using eigenvalue analysis. Fig. 5.5 shows the trajectory of the MG low-frequency eigenvalues (eigenvalue loci) when the secondary controller is designed faster by increasing its integral constant (k_i), for different design alternatives (see figure caption) of primary controllers. The Base case corresponds to the design presented in Section 5.3.1. In the remaining cases, only some specific primary controller parameters are changed. Results reinforce the idea that primary and secondary controllers are not coupled (in this design) since the trajectory of eigenvalues linked to the secondary controller (those that move when the secondary controller is changed) is the same regardless of the design of primary controllers. Loci of the rest of the eigenvalues (linked to the primary controllers) change for the different primary control designs, but are not affected by the design of the secondary controller (for all the changes of k_i).

Fig. 5.6 shows MG eigenvalue loci when communication delays increase from $T_d = T_{d0}$ to $T_d = 10T_{d0}$, for different designs of the secondary control. In the three secondary-control scenarios presented, T_{d0} is selected to keep the same ratio with the bandwidth of the secondary controller. As expected, the eigenvalues move to the right when the communication delay increases. In all three scenarios studied eigenvalues are poorly damped ($\zeta < 0.1$) when $T_d > 7T_{d0}$ (approximately) and the MG becomes unstable when $T_d > 10T_{d0}$. That means that secondary control modes feature similar damping values for similar values of the product $BW_s \cdot T_{d5}$. This fact can be used to accurately design the secondary controller according to the actual value of the communication delay.

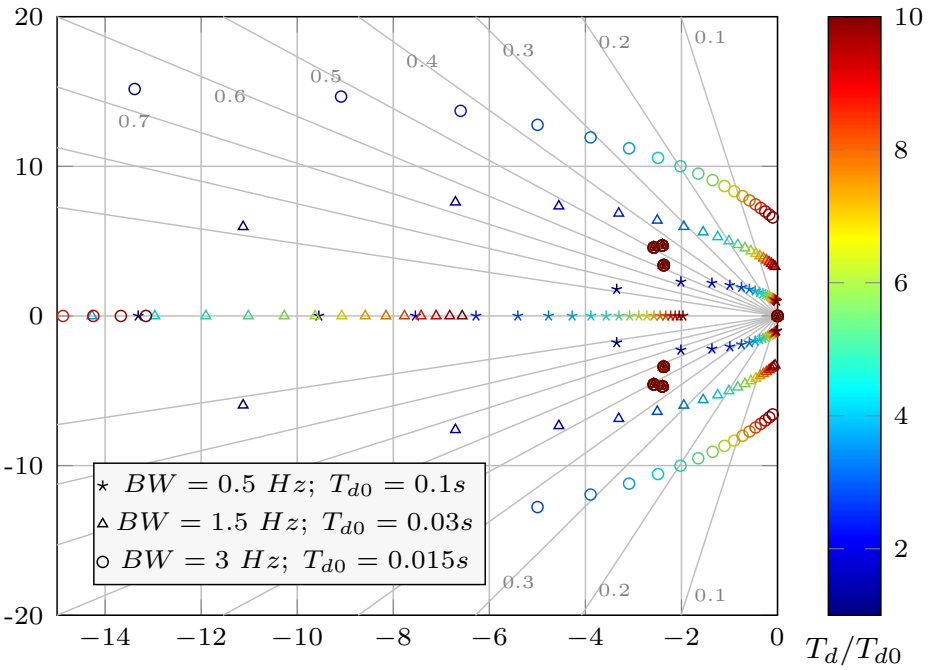

Figure 5.6: Eigenvalue loci when T_d increases from (blue) $T_d = T_{d0}$ to (red) $T_d = T_{d0}$, for different secondary controller designs.

5.4 Discussion

Participation-factor analysis has revealed little interaction between primary and secondary controllers in MGs for a range of different controller design solutions. This decoupling of the controllers is due to the specific implementation of the secondary controller. In the studied MG, all frequency droops were identical and also $k_{s1} = k_{s2} = k_{s3}$. When communication delays are identical for all converters and k_{si} parameters are equal, power sharing is maintained during frequency restoration. This is due to the fact that the secondary controller changes ω_{ni} with a similar ratio for all converters.

Therefore, the relative angles δ_i do not exhibit large disturbances. This could explain the decoupling of the controllers and why they seem to be more coupled when k_{si} parameters are not identical. It is likely some dynamic properties are difficult to see or are cancelled out by considering only the case of identical control parameters. Therefore, this aspect should be studied in detail to guarantee the decoupling of control layers with diverse droop designs.

This chapter has shown that secondary controller can be designed to be as fast as primary control, at least for the studied primary and secondary control designs. This aspect could help the design of faster secondary controllers. However, the application of this finding to a variety of control designs has to be investigated in more detail. Nevertheless, droop controllers and the secondary controller showed a weak interaction when they have similar time scales. This is most likely because the measurements acquired by the secondary controller depend directly on the active power LPFs of the droop controllers. Consequently, frequency restoration must not be configured faster than the droop because frequency dynamics also depend on droop LPFs. In this regard, it is recommended to design the secondary controller and the droops using similar time scales.

Apart from the design constraints derived from the primary control speed, communication delays also play an important role in the design of secondary controllers. Based on Fig. 5.6, secondary controller bandwidths can be designed with a maximum of $BW_s \approx 1/3T_{d5}$, where T_{d5} represents the communication delay. With this design, the oscillating modes linked with the secondary control feature a damping of approximately 5 %.

In any case, further research on this topic is necessary. In particular, non-linear analysis tools may need to be used to help explain the dynamics of the MG when large angle deviations between converters (δ_i) are expected. Also, deterministic time delays were considered in this study. However, communication delays can be more accurately modelled using stochastic variables. The study of the impact of stochastic time delays on secondary-control design is also of interest for further research.

5.5 Chapter Summary

This chapter illustrates the interactions between primary and secondary controllers by using eigenvalue and participation factor analyses applied to a test case. The effect of communication delays on the stability of MGs has also been studied, however, only up to a certain extent. An islanded MG with a central controller was studied. The central controller, based on a PI regulator, is used to restore the MG frequency.

Contrary to common believe, results show that, for the proposed control topology, primary and secondary controllers do not interact even when they are designed with similar speeds. In this chapter, different parametrisations of traditional $P - f$ droop

and internal voltage controllers were considered. MG stability characteristics remained unaltered when primary controllers were made slower and secondary control faster.

Only small interaction between the states related to the droops and the states related to the secondary controller was revealed when primary and secondary control were designed with similar speeds and when power sharing parameters k_{si} were different in each unit. In the study, time invariant deterministic communication delays were considered. Eigenvalue analysis showed that MG stability is deteriorated when communication delays increase. A relationship between communication delays, secondary control bandwidth and its associated eigenvalue was established. Based on these results, some recommendations have been made regarding the design of fast secondary controllers for frequency restoration. Those recommendations consider controllers topology and design and the expected communication delays.

Chapter 6

Coordination of Grid-Forming Devices for Seamless Transitions and Safe Operation of Microgrids

This chapter presents a secondary controller that coordinates batteries and distributed energy resources (DERs) in microgrids (MGs) to achieve seamless synchronisation with an external grid and transition between operating modes. During this process, grid-forming (GFM) interfaced batteries supply the energy required for the transition while the rest of GFM and grid-following (GFL) devices keep their operating point unaltered. The chapter is structured as follows. The MG topology considered for this study, the control and the proposed methodology overview are presented in Section 6.1. In Section 6.2, the proposed control is explained in detail. Simulation results are presented and discussed in Section 6.3. Finally, conclusions are drawn in Section 6.4.

6.1 Overview

6.1.1 Application Description

In a similar manner to Chapters 4 and 5, the Cigré's low-voltage distribution benchmark network for the integration of DERs [37] is used in this chapter. Fig. 6.1 shows a diagram of the MG while Fig. 6.3 depicts the structure the secondary controller used to coordinate the GFM converters. The MG can be connected to the main grid via the point of common coupling (PCC) and node BG of the grid. The system consists of a feeder and a transformer that feeds two loads ($L1$ and $L2$). In this MG scenario, it is assumed several that DERs and batteries are connected. Batteries are connected by using GFM converters ($C2$, $C3$ and $C5$) while DERs are connected by using either GFM ($C1$) or GFL ($C4$) converters. All the converters have an LCL filter.

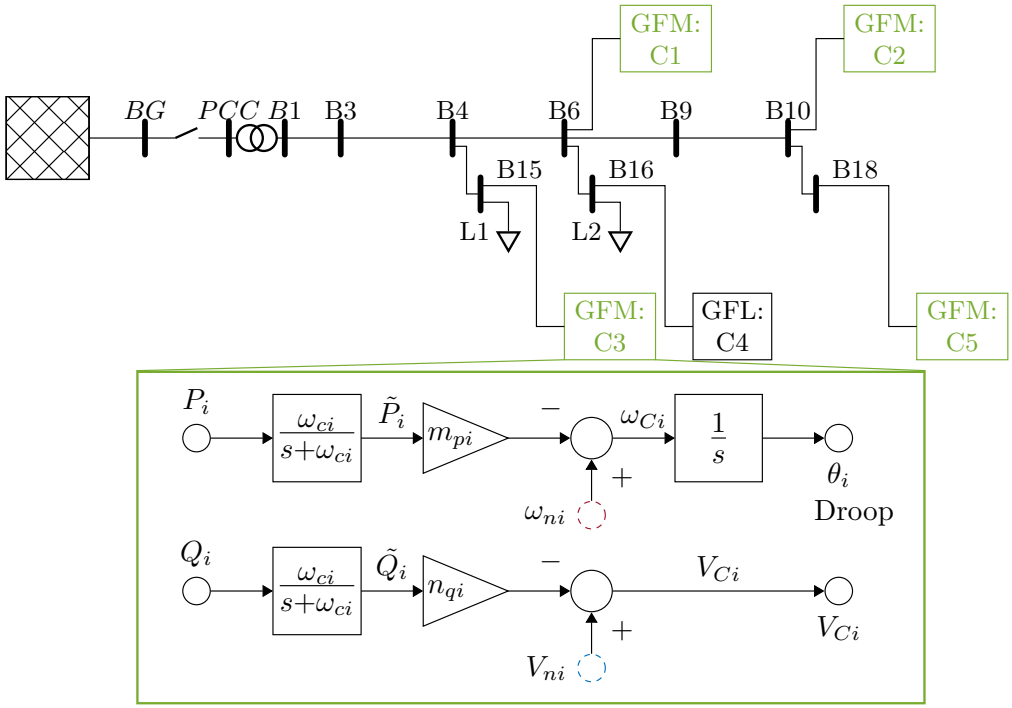

Figure 6.1: Single line diagram of the MG studied in this chapter, including the droop controllers of the GFM devices.

6.1.2 Control Overview

The basic control structure for GFL converters presented and analysed in Chapter 3 is used here. GFL converters inject the desired active and reactive powers by means of $d-q$ proportional-integral (PI) controllers that regulate the current through the inner inductance of the LCL filter. The converter is synchronised with the MG voltage using a phase-locked loop (PLL).

The GFM strategy presented in previous chapters is also applied here. It consists of conventional voltage and frequency droops and cascaded voltage and current controllers. In addition, quasi-stationary virtual impedances are used in GFM converters to facilitate their parallel operation [16]. Droop equations are repeated here for convenience [70]:

$$\omega_i = \omega_{ni} - m_{pi}\tilde{P}_i, \quad V_i = V_{ni} - n_{qi}\tilde{Q}_i, \tag{6.1}$$

where ω_{ni} and V_{ni} are the no-load frequency and voltage magnitude, respectively, and m_{pi} and n_{qi} are the droop characteristics of each device. The equivalent block diagram is depicted in Fig. 6.1. In that diagram, $\tilde{P}_i$ and $\tilde{Q}_i$ are the filtered values of the active and reactive powers injected by the unit. Therefore, using Laplace Transform:

$$\tilde{P}_i = \frac{1}{s/\omega_c + 1}P_i, \quad \tilde{Q}_i = \frac{1}{s/\omega_c + 1}Q_i, \tag{6.2}$$

where ω_c is the cut-off frequency of the first-order filter used. An example of the effect of the active power-frequency characteristics for different converters is depicted in Fig. 6.2. The droop characteristic (m_{pi}) and ω_{ni} define how the demand power is shared between GFM units. The total power supplied by the GFM units ($\tilde{P}_i$) defines the MG frequency (ω_{MG}).

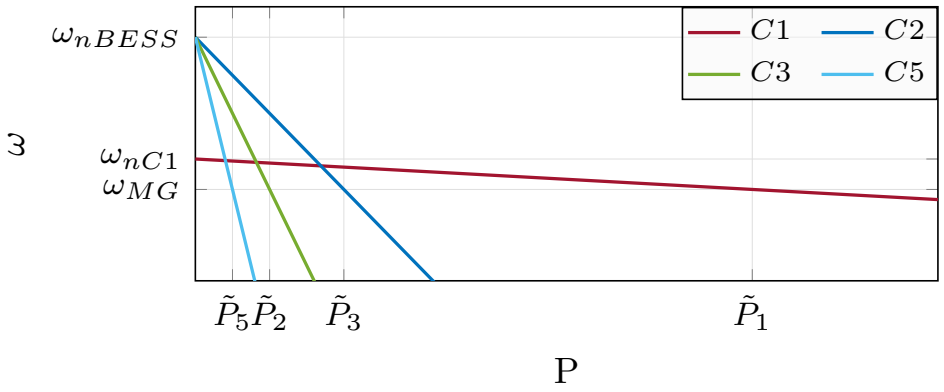

Figure 6.2: Example of droop curves for a MG with different GFM units. ω_{MG} is the MG frequency in steady state.

6.1.3 Battery Storage Systems Modelling and Control

In the MG under study, converters $C2$, $C3$ and $C5$ are used to interface battery energy storage systems (BESSs). Batteries are represented as constant voltage sources defined by their open circuit voltage. This assumption stands, in general, for lithium-ion batteries when state of charge (SOC) is between 20 %-80 % [159]. The SOC of the batteries is estimated by using the basic Coulomb counting method [64, 65]:

$$SOC_i(t) = SOC_{0i} - \frac{1}{C_i}\int i_{DCi}(t)dt, \tag{6.3}$$

where $SOC_i(t)$ is the SOC of the battery at a given time instant, SOC_{0i} is its initial value, C_i is the capacity of the battery and $i_{DCi}(t)$ is the current extracted from it.

The electronic interface for each battery is configured to be GFM. The droop coefficients for the batteries (m_{pi}) are updated according to the SOC of each unit [64, 160]:

$$m_{pi} = \frac{m_{p0}}{SOC_i^n}, \tag{6.4}$$

where m_{p0} is the initial value of m_p and n is selected based on the desired speed of SOC equalisation [64, 160].

6.1.4 Methodology Overview

Certain MG operations such as synchronistion with an external grid, update of control parameters or load changes may change the operating point of certain GFM units in

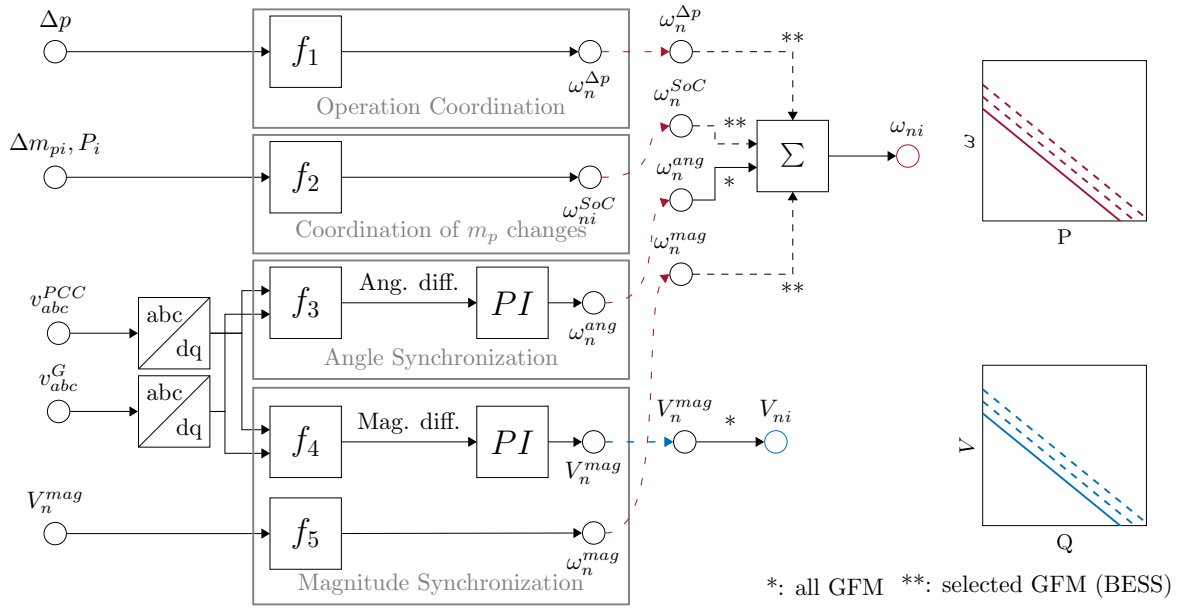

Figure 6.3: Proposed secondary controller. Generation of voltage and frequency set-points and adjustment of droop curves.

an undesired way. The proposed secondary controller maintains the operating point of selected GFM units and distributes the additional active power requirements among the batteries (that are GFM units) according to their SOC. The proposed secondary control is performed by changing the values of ω_{ni} and V_{ni} of the units (see Fig. 6.1) as commonly done in the literature [63]. The value of ω_{ni} and V_{ni} is calculated depending on the objective of secondary control as described in Fig. 6.3 and the following section. This constitutes the main contribution of the chapter. The adjustments in ω_{ni} are used to change the MG frequency and PCC voltage angle and the active power sharing of the grid. Meanwhile, V_{ni} is mainly modified to change MG voltage at the PCC during the synchronisation process.

6.2 Proposed Control

In this section, the control algorithm proposed to coordinate the MG devices is presented. This algorithm is depicted in Fig. 6.3. It must be noticed that the proposed secondary controller can be used to maintain the operating conditions of GFM units under three conditions: load changes, changes in droop parameters and during the synchronisation with an external grid. First, the coordination of converters when there are load changes will be explained. Secondly, the method to adapt the value of m_{pi} according to the SOC without changing the operating point will be depicted. Thirdly, the angle synchronisation will be explained. Finally, the method used to equalise the voltage will be presented. Some general explanations regarding power sharing in droop

based MGs are given before presenting the proposed controllers.

6.2.1 Coordination of BESSs for Power Sharing

In order to share load variations between several BESSs, the values of ω_{ni} are adjusted. As in Fig. 6.4, the initial total power delivered by the GFM converters ($\tilde{P}_t$) results in a determined value of the MG frequency (ω_{MG}). However, when the power demand changes, BESSs (GFM_b and GFM_c) have to shift up or down droop curves (dashed) to compensate for the power variation in order to retain the MG frequency and the GFM_a operating point. For simplicity, only the demand increase case is considered here. The droop curves describing this situation are depicted in Fig. 6.4. When there is a demand increase in the MG ($\Delta p = \tilde{P}'_t - \tilde{P}_t$), the frequency naturally drops. To maintain the same MG frequency (ω_{MG}), a shift in ω_{ni} ($\omega_n^{\Delta p}$) is applied. In a MG with a single droop (m_p), $\omega_n^{\Delta p}$ is calculated as:

$$\omega_n^{\Delta p} = m_p \Delta p. \tag{6.5}$$

In this case, with several droop units (m_{pi}) $\omega_n^{\Delta p}$ is calculated as:

$$\omega_n^{\Delta p} = f_1(\Delta p) = \frac{1}{\sum_i \frac{1}{m_{pi}}} \Delta p, \tag{6.6}$$

where m_{pi} are the droop slopes of all GFM units, not only BESS.

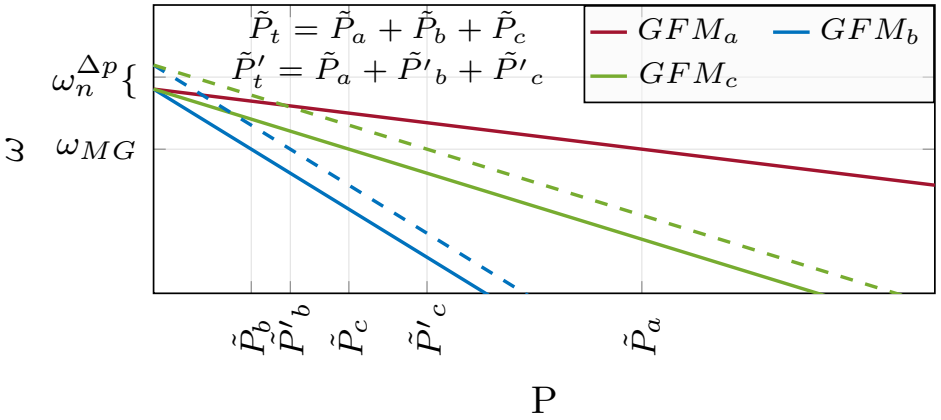

Figure 6.4: Adjustment of droop curves to share power variations between units and keep the same MG frequency. Only three GFM converters are considered here for the sake of simplicity.

When this criteria is applied, the batteries absorb the power variations without altering the operating point of the remaining GFM units. This strategy can be applied when changes in load or generation are scheduled, or when the MG is being synchronised. If a controllable load is connected/disconnected, $\omega_n^{\Delta p}$ is applied simultaneously

to all the battery units. Similarly, when the MG consumption is constant, but the generation varies because the set-point variations are known, that change can be used to calculate Δp and $\omega_n^{\Delta p}$, instantaneously. This strategy will be applied in the following sections to keep the same operating point while the MG is being operated.

6.2.2 Adjustment of m_{pi} According to BESS SOC

In this work, the droop parameters (m_{pi}) of BESSs are adjusted according to the SOC of their batteries. When these parameters are modified, the equilibrium point of the MG may change as well, causing a variation in the power delivered/absorbed by the GFM devices. Thus, in order to maintain the frequency and power equilibrium, it is necessary to change both m_{pi} and ω_{ni}, simultaneously. For each BESS, the frequency before the change in m_{pi} can be calculated as in (6.7). After updating the value of m_{pi} with m'_{pi}, the frequency is calculated as in (6.8), which includes the additional term ω_n^{SOC}. Considering that the MG frequency before and after adjusting the parameters is the same (6.9), and operating with (6.7) and (6.8), the required value of ω_n^{SOC} is obtained using (6.10):

$$\omega_i = \omega_{ni} - m_{pi}P_i, \tag{6.7}$$

$$\omega_i = \omega_{ni} - m'_{pi}P_i + \omega_{ni}^{SOC}, \tag{6.8}$$

$$m_{pi}P_i = m'_{pi}P_i + \omega_{ni}^{SOC}, \tag{6.9}$$

$$\omega_{ni}^{SOC} = f_2(\Delta m_{pi}, P_i) = P_i(m'_{pi} - m_{pi}). \tag{6.10}$$

The use of these expressions ensures that, when the control parameters are changed, the operation point of the units does not change. Nonetheless, afterwards the MG load variations are shared between the BESSs according to the newly defined m_{pi} parameters.

6.2.3 PCC Voltage Angle Synchronisation

Angle synchronisation is achieved when the angles of the PCC voltage and the voltage at the grid connection point (BG) are the same, in steady state. In this case, the MG frequency will be equal to the grid frequency. Angle synchronisation is carried out by accelerating or decelerating the MG frequency (i.e., adjusting ω_{ni}).

Fig. 6.5 (b) and (c) show two different ways to adjust ω_{ni} in order to change MG frequency from ω_{MG} (in Fig. 6.5 (a)) to ω_G. In Fig. 6.5 (b), only one ω_{ni} parameter (ω_{nb}) is changed to synchronise ω_{MG}. After the change in ω_{nb} (dashed), the GFM devices inject the same total amount of power as before the synchronisation ($\tilde{P}_t$). Moreover, the value of the MG frequency has increased up to ω_G. Since the frequency of only one device (ω_{nb}) was changed, the power sharing between GFM units changes. In contrast, when all GFM units are adjusted simultaneously (i.e., by changing the values of all ω_{ni}) and uniformly, the power sharing between units is kept constant. The curves

representing this operating mode are depicted in Fig. 6.5 (c) where, as expected, the MG frequency is now ω_G and all operating points are maintained. The strategy depicted in Fig. 6.5 (c) is proposed in this chapter to synchronise the voltage angles at both sides of the connection switch.

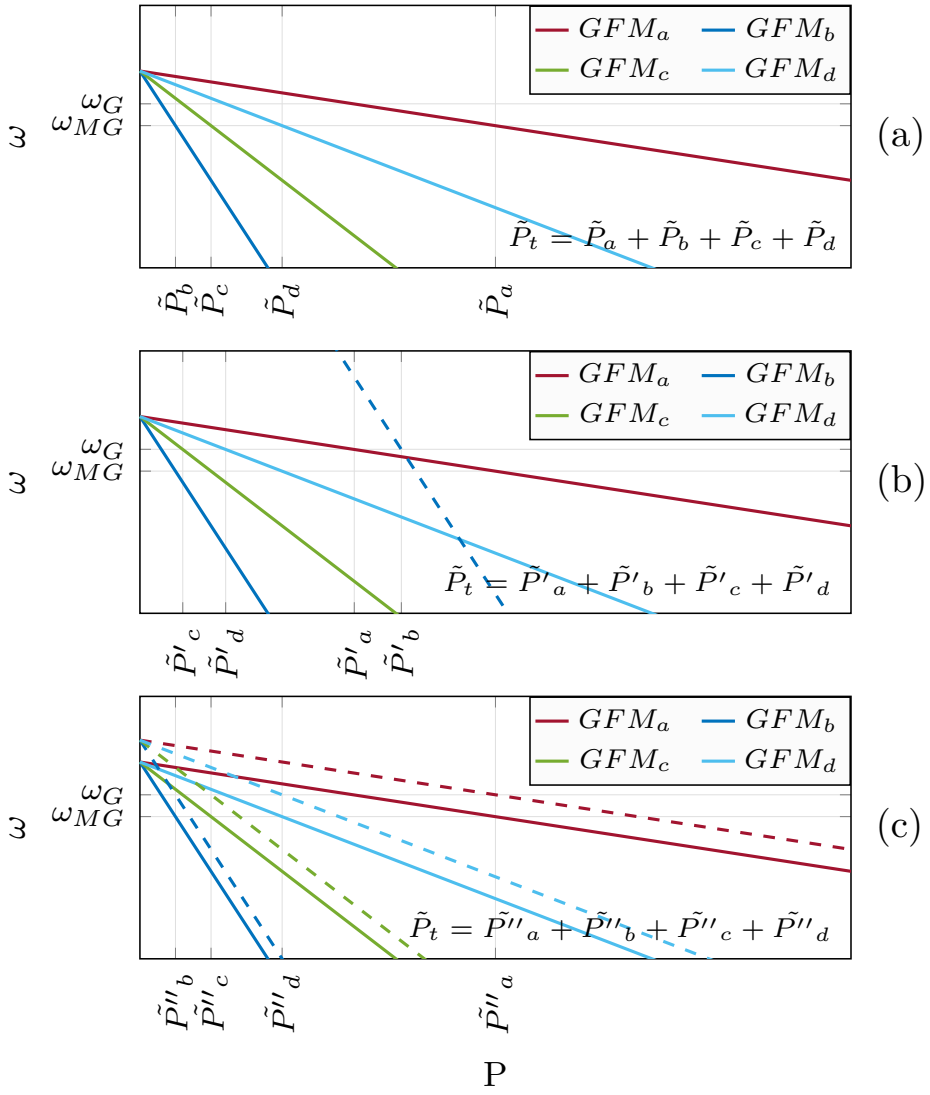

Figure 6.5: MG frequency adjustment by modifying ω_{ni}. (a) Initial case: at operating point GFM units deliver $\tilde{P}_t$ and MG frequency is ω_{MG}. (b) Frequency is adjusted to ω_G by changing the droop of a single device (GFM_b). (c) Frequency is adjusted to ω_G by changing all the droops.

In the alternative proposed here, the set values of ω_{ni} are sent via communications from the secondary controller. For that purpose, a PI was applied over the angle difference between the PCC and the grid voltage, as shown in Fig. 6.3. The angles can

be calculated as follows:

$$\theta_G = \arctan \frac{v_q^G}{v_d^G}, \quad \theta_{PCC} = \arctan \frac{v_q^{PCC}}{v_d^{PCC}}, \tag{6.11}$$

while the angle difference is defined as:

$$\delta = f_3(v_{dq}^G, v_{dq}^{PCC}) = \theta_G - \theta_{PCC}. \tag{6.12}$$

Park transformations can be carried out by using the angle of any reference frame since the angle difference between BG and PCC voltage space vectors does not depend on the reference frame selected.

The approach proposed here for the MG synchronisation with the grid does not change the operating point significantly. However, slight changes in the operating point may occur as some loads or MG elements change their outputs according to the grid frequency. These changes are relatively small and, therefore, the MG stability indicators should not be affected.

6.2.4 PCC Voltage Equalisation

In order to synchronise the voltage magnitude of BG and PCC and share the responsibility between all GFM units, all GFM nodes must vary their voltage value. This is achieved by modifying V_{ni} values as indicated in Fig. 6.3. Grid and MG voltages at the PCC are measured and transformed to dq reference frame as explained before. Then the voltage magnitude difference between BG and PCC is calculated as:

$$\Delta U = f_4(v_{dq}^G, v_{dq}^{PCC}) = U^G - U^{PCC}, \tag{6.13}$$

where

$$U^G = \sqrt{v_d^{G2} + v_q^{G2}}, \quad U^{PCC} = \sqrt{v_d^{PCC2} + v_q^{PCC2}}. \tag{6.14}$$

A PI controller is applied on the secondary level over ΔU. The output of this PI controller (V_n^{mag}) changes the voltage setting of all the droop (V_{ni}). Incidentally, there might be more advanced criteria to change the set points for the droop. For example, to improve the reactive power sharing during the transient. This is not studied in this work, but it is of interest for future research.

The change in bus voltages in the MG will vary the power absorbed by loads. If this is not compensated, the load changes will be shared among all GMF units according to their droop constants. To guarantee that all BESSs inject or absorb the power variation, ω_{ni} must be adjusted. In the following sections, a method to estimate and share this extra power among the battery units is presented.

Estimation of Power Variation

The variation in the power consumed by the MG is mainly caused by the variation in the MG voltage. In order to calculate and compensate that term, an expression that links the voltage variation with the power consumption is derived here. For that purpose, it is assumed that the voltage magnitude and its variation is equal in all the nodes. Under these considerations, a linearised expression that links the power absorbed by the loads and the MG voltage can be obtained:

$$p_i = \frac{v_i^2}{r_i}, \quad \Delta p_i \approx \frac{dp_i}{dv_i}\Delta v_i, \tag{6.15}$$

where p_i is the active power consumed by load i, v_i is the voltage at which load i is connected, and r_i is its resistance. By manipulating (6.15), then

$$\Delta p_i \approx \frac{2v_{io}}{r_{io}}\Delta v_i, \quad \text{and} \quad \Delta p_i \approx \frac{2p_{io}}{v_{io}}\Delta v_i, \tag{6.16}$$

where sub-index o denotes an initial value. The total power variation, that is, the addition of all the power variations of all the loads is:

$$\Delta p = \sum_i p_i \approx \sum_i \left(\frac{2p_{io}}{v_{io}}\Delta v_i \right), \tag{6.17}$$

Finally, (6.17) can be simplified as follows:

$$\Delta p \approx \frac{2\sum_i \Delta p_{io}}{v_o^{PCC}}\Delta v^{PCC}. \tag{6.18}$$

Since the internal voltage controllers of the converters are much faster than secondary controller, it is assumed that V_{ni} is applied directly to the MG. Then:

$$\Delta p \approx \frac{2\sum_i p_{io}}{v_o^{PCC}} V_n^{mag}. \tag{6.19}$$

The accuracy of this estimation depends on the voltage controller implemented and the measurement point of the active power at each converter. If the voltage is controlled at the point where the power variations are expected, the error will be small, but the estimation error increases as more resistance is placed between these two points. The power estimation presented in (6.19) is combined with the expression in (6.6) in order to update the battery droops. Then, the extra power need would be compensated:

$$\omega_n^{mag} = f_5(V_n^{mag}) = \frac{1}{\sum_i \frac{1}{m_{pi}}} \frac{2\sum_i p_{io}}{v_o^{PCC}} V_n^{mag}. \tag{6.20}$$

6.2.5 Summary

As explained before, the proposed secondary controller coordinates the operation of BESSs to adjust to changes in the MG without changing the operating point of some selected GFM units. Under commanded load changes, ω_{ni} is adjusted using (6.6). When droop parameters are changed according to SOC, (6.10) should be used to adjust ω_{ni}. And finally, for the synchronisation with an external grid, droop parameters ω_{ni} and V_{ni} can be changed by using PI controllers on the voltage magnitude (6.13) and angle (6.12) differences between BG and the PCC. In this case, ω_{ni} needs an extra adjustment defined by (6.20).

To summarise, the voltage droop is adjusted in all GFM devices by using the following expression if synchronisation is the objective (6.13):

$$V_n^{BESSi} = V_n^{geni} = V_n^{mag}. \tag{6.21}$$

However, for the case of the frequency, ω_{ni} takes different values depending on the type of GFM device and the objective of the secondary controller. In generator units, ω_{ni} only depends on the angle synchronisation loop. Meanwhile, in BESS units ω_{ni} depends on the coordination controller (6.6), the controller that updates m_{pi} according to the actual SOC (6.10), the angle synchronisation loop (6.12) and the voltage synchronisation loop (6.20) whenever they apply:

$$\begin{aligned} \omega_n^{geni} &= \omega_n^{ang}. \\ \omega_n^{BESSi} &= \omega_n^{\Delta p} + \omega_{nSOC} + \omega_n^{ang} + \omega_n^{mag}. \end{aligned} \tag{6.22}$$

6.2.6 PI Secondary Controllers and Droop Controller Design

Effect of Droop Coefficients on Stability

The proposed secondary control strategy actively changes the droop gains of GFM devices while the operating point remains almost constant. Then, this variation in the droop coefficients would lead to a variation in the MG stability properties, as the droop is one the factors with the strongest influence on the MG stability [70]. In this chapter, conservative values of the droop gains will be used so the stability is not jeopardised (see Chapter 3).

Adjusting the Synchronisation Speed

Synchronisation speed can be modified by adjusting the proportional and integral gains of the corresponding PI controllers. For angle synchronisation, the $PI - f$ controller can be designed to have similar bandwidth to that of the primary controllers since they are decoupled (as indicated in Chapter 5). In contrast, fast voltage controllers result in

low accuracy of power estimations. Therefore, it is recommended to limit their speed. A more detailed analysis is of interest, but it will not be carried out out for brevity.

6.3 Secondary Controller Validation

6.3.1 Description of the Case Study

The proposed controller was applied to the MG presented in Fig. 6.1. As a reminder, there are five converters: $C2$, $C3$ and $C5$ are GFM converters and interface batteries, $C1$ is also a GFM converter and ($C4$) is a GFL converter. The main objective was to perform a seamless transition when the MG conditions change and when the MG is synchronised with an external grid. The coordination process when load and power generation conditions change is presented in Section 6.3.2. Update of droop slopes is presented in Section 6.3.3 and synchronisation is explained in Sections 6.3.4, 6.3.5 and 6.3.6.

The case study has been analysed in a simulator that was developed in Matlab/Simulink and the simPowerSystems toolbox. This simulator included averaged models of the converters. The results obtained in this simulation were validated in an OPAL-RT 2130 platform. A discrete time solver with a simulation step time of 100 μs was used on that platform. The MG data can be found in [37] and Chapter 4 (Table 4.1 and Table 4.2 SC1).

6.3.2 MG Coordination. Simulation Results

Fig. 6.6 and Fig. 6.7 show the transient response of the active and reactive powers injected by each device under different conditions. Fig. 6.6 shows the power transients when a change in the load of 3 kW is applied at $t = 5$ s and the proposed controller is applied. Clearly, all GFM devices present an inertial response after the load change. This means that all the GFM converters are injecting power at $t = 5$ s. However, after few seconds the batteries (C2, C3 and C5) inject all the active power demanded by the load while C1 (GFM) returns to its original operating point in terms of active power.

A ramp change in the power provided by the GFL unit is presented in Fig. 6.7. In this case, the command sent to the GFL unit is used by the secondary controller to adapt the battery droops. In this way, batteries inject the additional energy needed by the MG and remaining GFM units maintain their operating point. Since the change in the generation conditions is gradual, there is not a sudden active power change when the generation conditions change ($t = 5s$) as in the previous case.

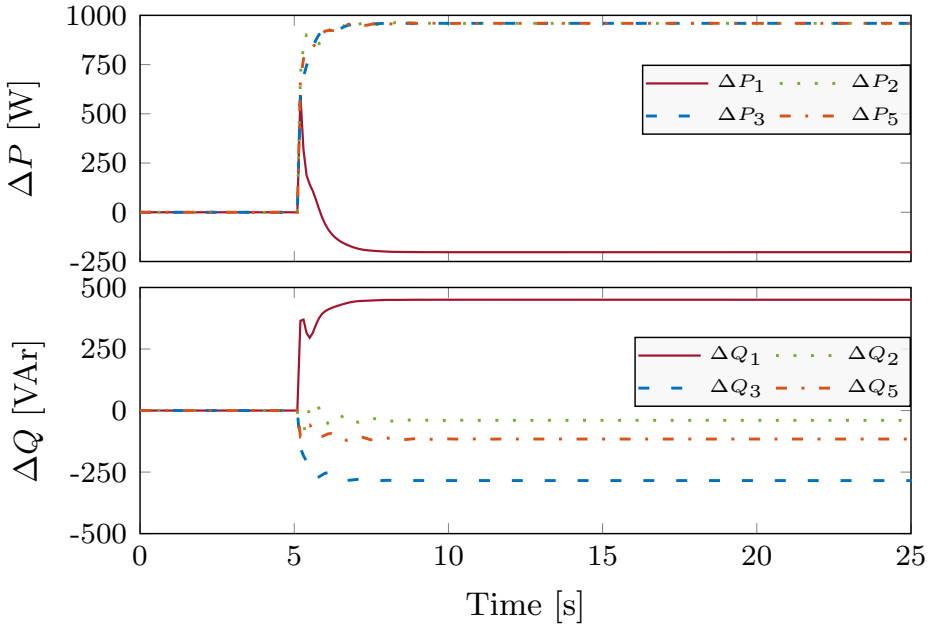

Figure 6.6: Active and reactive power variations when a 3 kW load is connected.

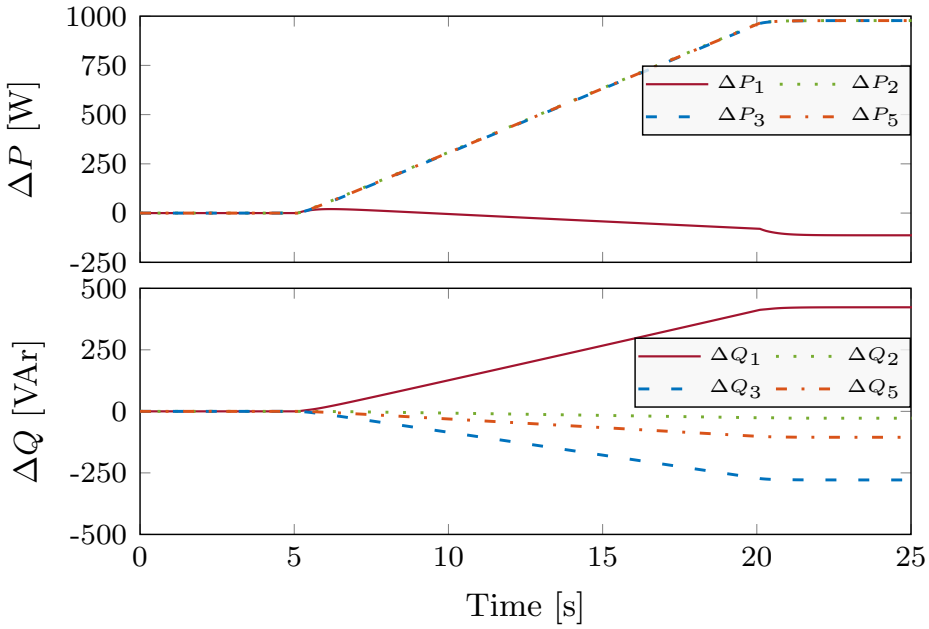

Figure 6.7: Active and reactive power variations when a GFL unit decreases 3 kW its power output, following a ramp.

6.3.3 Updating m_{pi} Terms According to SOC

In Fig. 6.6 and Fig. 6.7, the extra power absorbed by the loads is equally shared between all batteries. In order to share that power according to their SOC, the parameters m_{pi} can be selected to be different in each unit. However, a sudden change of these parameters may change the operating point, as previously discussed.

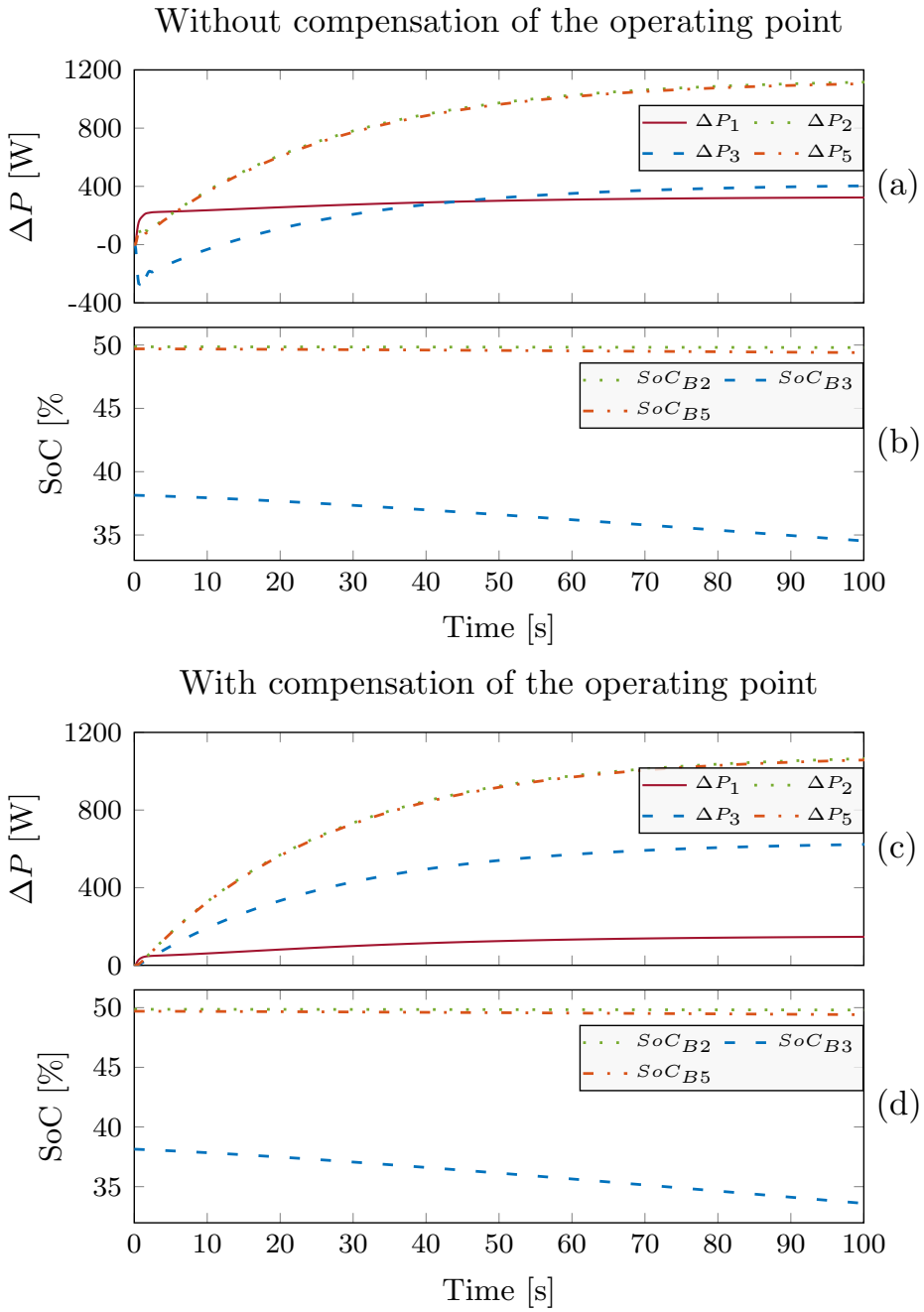

Figure 6.8: Transient of the SOCs and the power when the MG demand increases. m_{pi} parameters are changed at $(t = 0)$ according to the SOCs of batteries (a) and (b) without and (c) and (d) with compensation of the operating point.

Fig. 6.8 (a) shows that, when m_{pi} parameters are changed (at $t = 0$), there is a sudden change of the operating point. That is, the power deviation (ΔP) of the GFM units at $t = 0$ is not zero. This is corrected by adding an additional term to ω_{ni} (6.10). Fig. 6.8 (c) shows the response of the MG when the values of m_{pi} are changed according to the SOC and the additional term ω_{nSOC} is included. In this case, the operating point

at $t = 0s$ is almost unchanged and the power is shared according to the SOC of each battery (see Fig. 6.8 (d)). Therefore, it can be concluded that the term ω_{nSOC} avoids large modifications in the operating point when the droops are modified.

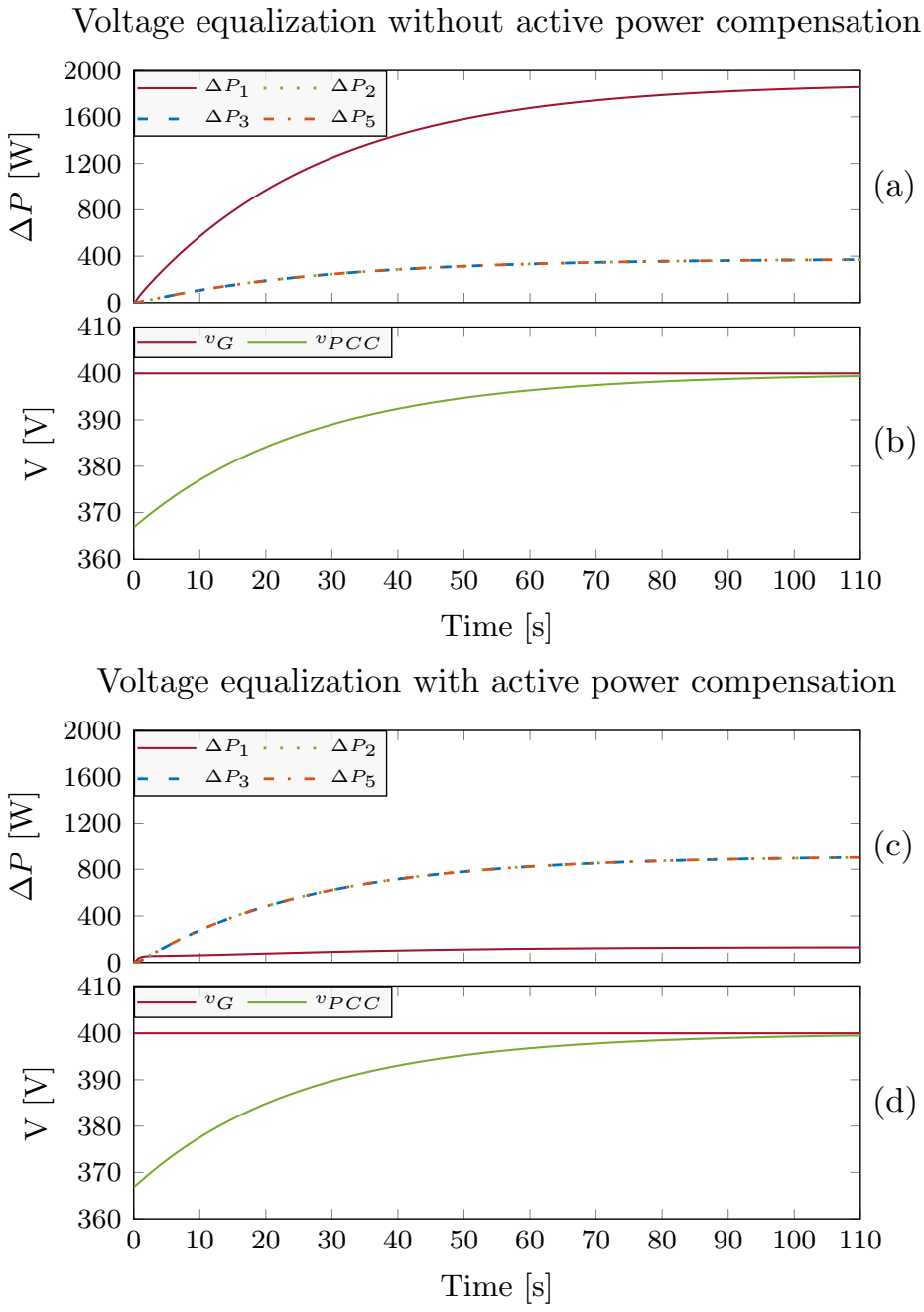

Figure 6.9: Voltage magnitude synchronisation process. In (a) and (b), synchronisation without compensating the power variation. In (c) and (d), with compensation of the power variation in order to maintain the operating point of C1.

6.3.4 Voltage Magnitude Synchronisation and Power Sharing

Fig. 6.9 (a) and (b) show the voltage magnitude synchronisation process without any load compensation. The magnitude of the PCC voltage is accurately synchronised with the voltage of the grid. However, as the $P - f$ droop is not corrected during the transition, the power injected by each one of the GFM units changes along the synchronisation process. In Fig. 6.9 (c) and (d), the additional term used to correct the power sharing is applied and only the batteries inject the extra power that the loads absorb due to the change of the MG voltage. The power injected by the GFM unit without a BESS decreases from 1.9 kW to 0.2 kW. Therefore, the power required from this unit is significantly reduced. The active power injected by the GFM unit is not exactly zero due to the approximations considered to calculate demand variations.

6.3.5 Voltage Angle Synchronisation

The process of angle synchronisation is shown in Fig. 6.10. Fig. 6.10 (c) shows that angle synchronisation is achieved after 40 s, approximately. Fig. 6.10 (a) shows that the

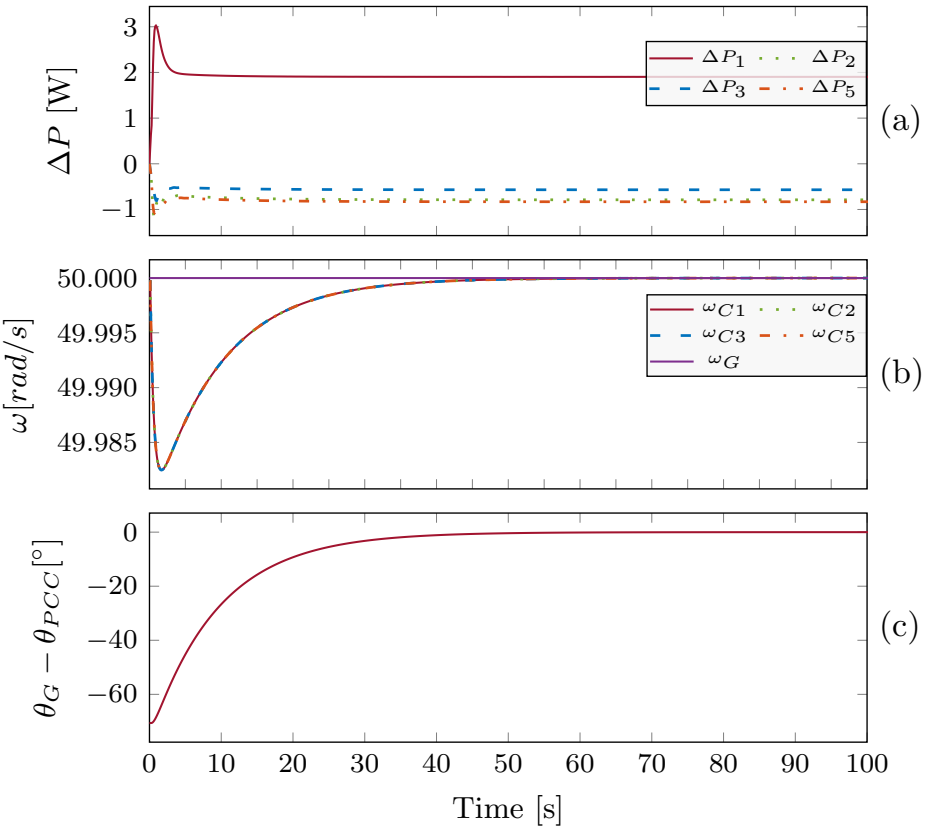

Figure 6.10: Voltage angle synchronisation process. (a) Power variation in each of the GFM units, (b) local frequency of each of the GFM units compared to the grid frequency, and (c) voltage angle difference between the PCC and the grid.

variations of the output powers of the GFM units during the synchronisation process are negligible (few watts) compared to the power needed for the voltage synchronisation (thousands of watts). This happens because the values of ω_{ni} are updated in all the GFM units simultaneously, as calculated by (6.12) and shown in Fig. 6.10 (b).

6.3.6 Microcrid Syncronization

Fig. 6.11 shows the synchronisation process of the PCC voltage (both magnitude and angle) with the grid voltage. Both the magnitude and angle are synchronised simultaneously (Fig. 6.11 (a) and (b)). Compared to the results presented before, PI con-

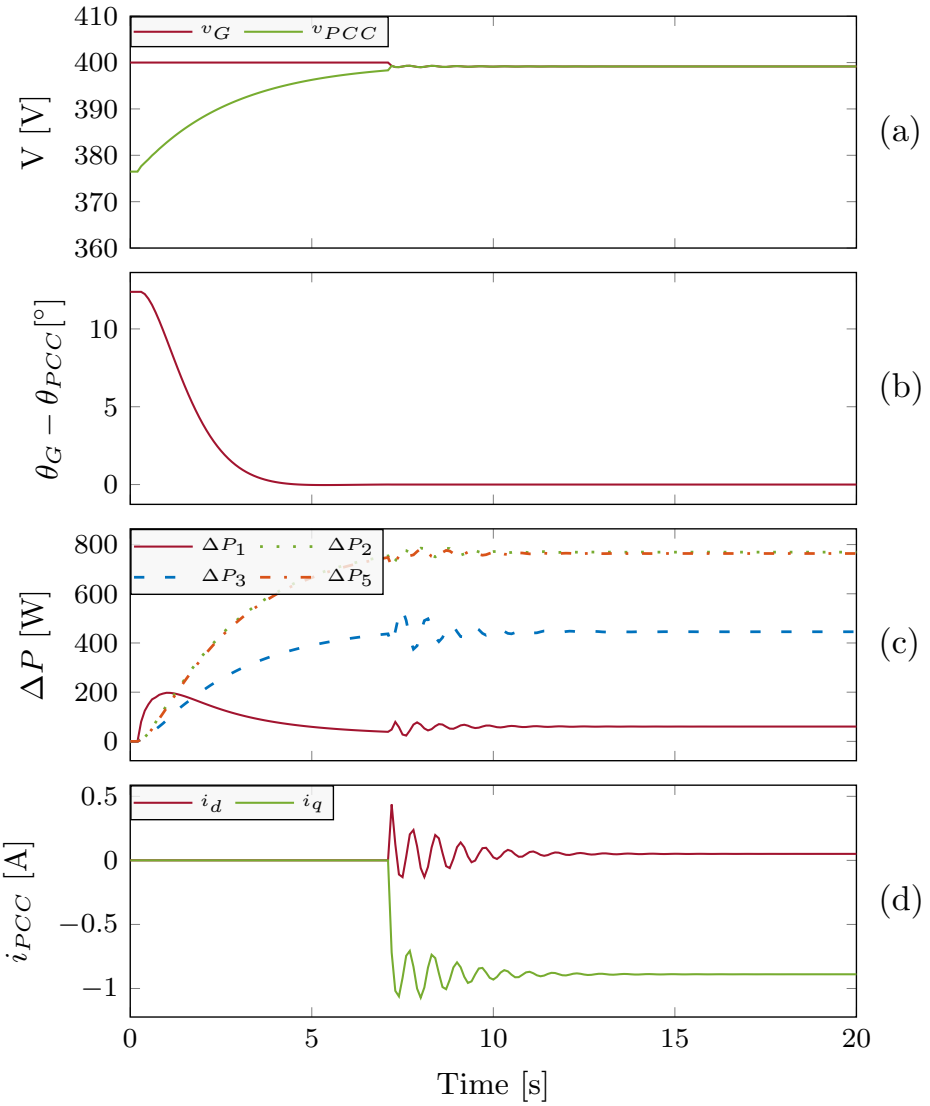

Figure 6.11: Transient showing the synchronisation of PCC voltage with the grid voltage. (a) voltage magnitude, (b) angle difference, (c) power variation of GFM converters and (d) current exchanged with the grid.

trollers have been designed to be faster and synchronisation is achieved within 10 s. In addition, the resistive part of the virtual impedance has been reduced to the lowest possible value that enables a stable operation of the MG. This allows the power injected/absorbed by the GFM converter C1 to be constrained during the synchronisation process. Fig. 6.11 (c) shows that the power estimation method only accounts for the steady state power variation. Therefore, as the speed of the synchronisation process increases, some dynamics are not captured by the estimation and GFM units may have some undesired power exchanges within the MG during the synchronisation process.

Once the PCC and the grid voltage are synchronised (at $t = 7$ s, approximately), the MG is connected to the grid by closing the main switch. Fig. 6.11 (d) shows the transient of the current through the line that links the MG with the grid. The exchange of energy at the connection point and the transient response depend on the strength of the main grid and the design of primary controllers of the MG. However, as the MG is well synchronised with the main grid, the power exchanged is negligible.

6.4 Chapter Summary

In this chapter, a controller that enables the coordinated operation of several GFM units in a MG has been presented. The proposed secondary controller enables to maintain the operating point of selected GFM units during MG operations that involve changes in active power sharing or operating points. The operations considered in the study are: the commanded active power change in load or generation, the change of droop parameters according to the SOC of the BESS and the MG synchronisation with an external grid. This chapter only focuses on active power sharing, and therefore reactive power sharing may change during certain operations such as MG synchronization. The controller coordinates the GFM units so that batteries absorb/inject the necessary energy while the other GFM generation does not change its operating point (in terms of active power).

The proposed secondary controller modifies the no-load characteristics of the GFM units droops to achieve the desired power sharing. This implementation is well known in the literature. However, to the authors knowledge, it has not been used to this purpose until now. In general terms the proposed algorithm calculates the active power variation involved in a MG operation and modifies droops to facilitate that BESS provide the extra energy.

Theoretical and simulation results have shown that the proposed controller maintains the active power operating point of the desired GFM converters during load variations and when the MG is synchronised with the main grid. Only small changes in the active power were observed, which happen due to the approximations done to calculate the power involved in the transition and due to unforeseen losses of the system. It has also been shown that the design of internal controllers can have a relevant impact

on the secondary controller performance, specially if the dynamics of the primary and secondary controllers are too close. The results were replicated with OPAL-RT, being identical to those obtained with simPowerSystems.

Chapter 7

Conclusions and Suggestions for Further Research

In this work, primary and secondary controllers of microgrids (MGs) have been modelled, analysed and designed. Different small-signal tools have been used to evaluate the impact of these controllers on the system stability. Based on these analyses, guidelines to assist designers in choosing the control parameters of MGs are presented. Finally, different primary and secondary controllers have been proposed to facilitate the coordination of grid-forming (GFM) converters. Realistic effects of communication systems have also been analysed. Studies related to primary control have been validated by using numerical simulations and experiments in a laboratory. Secondary control studies have been validated by using detailed simulations. This chapter presents the summary, conclusions and contributions of this thesis together with suggestions for further research.

7.1 Summary and Conclusions

This section summarises the work presented in this document and the conclusions drawn from it.

- The work carried out has shown that the design of phase-locked loop (PLL) controllers in weak grids is highly affected by the loading conditions, and that controllers (e.g., voltage and current) of a power converter interact with controllers of other converters and synchronous generators (SGs). This aspect has most often been disregarded in conventional bulk power systems. However, in the future, this issue could become relevant in those systems, as the penetration of converter-interfaced resources is rapidly increasing. Therefore, grid operators should evaluate the situation carefully and counteract, as appropriate. For example, they

could enforce the use of certain bandwidth ranges for controllers in order to avoid those interactions. Tools such as those applied in this work could be used.

- This work has demonstrated that coordinated design of primary controllers such as droops and virtual impedances of several GFM converters facilitates the participation of small distributed resources on frequency ancillary services. This type of services will probably play a more important role in future grids as SGs are being replaced by renewable generation. However, the design of primary controllers on its own is insufficient to guarantee the provision of frequency services as the energy required should be obtained from a primary source that is not always fully dispatchable. In this respect, constraints associated with droop constants may be used to limit the power injected by certain units, as discussed in Chapter 4. Frequency services could be provided, more flexibly, if energy storage systems are used. Nonetheless, if these services must be provided by renewable generation, it is necessary to guarantee some degree of power reserve. This could be achieved by operating renewable sources below their maximum power points, or by implementing hybrid solutions with storage.

- Contrary to popular belief, secondary controllers for frequency restoration can be designed to be as fast as primary controllers without causing instabilities, as demonstrated in Chapter 5. This conclusion, valid when secondary control simultaneously changes the zero-load frequency of all droops used as primary controllers, could boost the design of faster secondary controllers. Although promising, this study presents some limitations since implementation aspects of secondary controllers were not considered and simple models of delays were used. It was found that commands sent from the secondary controller to the primary controller produce slight changes in the MG operating point. As a consequence, small-signal stability is affected to a minor extent. However, for other control implementations, the conclusions drawn in Chapter 5 would not be valid. Regarding communication delays, the model used was simple. For example, the same delay was used for all the converters, and this helped to keep the operating point constant during transitions. However, in real applications, delays are commonly variable and of a stochastic nature. This may result in variations of the operating point during frequency restoration. As a consequence, primary and secondary controllers could be more coupled than in the MG studied in this thesis.

- Although power sharing in droop dominated MGs is defined by droop slopes, secondary control can be used to alter the predetermined power sharing. A simple secondary controller that simultaneously changes the zero-load frequency of droops was used in Chapter 5 and Chapter 6 to restore MG frequency and synchronise it with an external grid. With this controller, it is possible to synchronise

the MG without altering the operating point of some selected GFM converters. Due to its simplicity, with minor modifications, this controller can also be used to support other operations that involve active power variations. The results obtained in these chapters are valid in MGs when active power is strongly related to frequency while reactive power is related to voltage. This is a property of grids with high X/R ratio, but can also be applied in grids with low X/R ratio if the equivalent output impedance of generators (real plus virtual) is mainly inductive, like it was in this case. However, these results cannot be directly applied to secondary voltage controllers or MGs where active power is strongly related to voltage because voltage is not a global variable and internal voltage controllers may be different for each unit. Tackling voltage problems requires additional work.

7.2 Original Contributions

The main contributions of this work are listed in the following paragraphs:

- **A novel eigenvalue analysis that revealed the interactions between the PLL and the voltage and current controllers of GFM and grid-following (GFL) converters in MGs was presented.** This analysis demonstrated that the stability region of the PLL is reduced when the power injected by GFL converters increases. Also, the PLL stability region is reduced when the outer control layers of GFM and GFL converters are slow. Finally, it was shown that the design of the inner current controllers of GFM converters affect the stability in the opposite direction (faster controllers lead to a smaller stability region).

- **A design guide for the primary controllers that avoids interactions between PLLs and controllers of other devices has been proposed.** This guide was based on the analytical studies presented in this work. Given an initial design of controllers, the proposed methodology recalculates them in order to fulfill the specifications of the designer. In this methodology, current, voltage and frequency controllers of GFL and GFM converters, and SGs, are considered.

- **A design methodology of primary controllers that enables the aggregation of distributed resources to provide frequency support services has been presented.** Thanks to this methodology, frequency dynamics of MGs are kept constant when operating conditions change. The methodology is based on a small-signal model of the MG. Based on this model, the control parameters of GFM devices are adjusted selectively in order to preserve the MG stability margins. The methodology can be applied with any type of GFM control strategy. In addition, this methodology takes into consideration all primary controllers that

affect the MG frequency dynamics (it does not disregard primary controllers such as virtual impedance that are often omitted).

- **To best of the author's knowledge, this work is the first time in which parametric sensitivities have been used to relocate several eigenvalues simultaneously to define frequency dynamics.** In the existing literature, parametric sensitivities are commonly used to relocate a single eigenvalue or a pair of complex eigenvalues. Few references can be found where parametric sensitivities are used to relocate several eigenvalues simultaneously. In those cases parametric sensitivities are used to damp power system oscillations. Moreover, both components of the sensitivity (real and imaginary) were used, unlike in the common approach, in which only the real parts of sensitivities are used. Here parametric sensitivities were used to shape the dynamics of a specific variable, MG frequency. The use of the two components of the sensitivity facilitates the reallocation of eigenvalues to specific points in the complex plane (instead of just moving them to the left). Relocating the most important eigenvalues that define certain dynamics (in this case frequency) helps to achieve the desired response more easily.

- **Recommendations for the design of fast frequency secondary controllers were made in Chapter 5.** Recommendations were based on the eigenvalue analysis that characterised interactions between primary and secondary controllers and the influence of time delays on secondary controllers. Guidelines consider the topology of primary and secondary controllers, the speed of primary controllers and the expected communication delays.

- **A simple and original secondary controller that preserves the operating point of selected GFM converters during MG transitions thanks to GFM converters for battery energy storage systems (BESSs) has been proposed.** The controller allows GFM generators short of reserves to maintain their operating point constant during transitions (e.g., renewable energy sources operating at the maximum-power point). This controller is specifically designed to allow a seamless synchronisation with an external grid and the coordination of all MG devices needed during its operation. In the proposed secondary control, BESSs inject the extra energy needed for the transitions while the power injected by other GFM units is maintained approximately constant. Since droop constants are not altered, the inertial response of all GFM units is preserved and all GFM units experiment only small power deviations. After the transient, BESSs reach a new operating point while other units return to the initial operating point.

The research presented in this thesis improves the integration of renewable resources in power grids from several points of view. Firstly, the analysis and design guide of pri-

mary controllers should allow a safer integration of renewable resources to weak grids by avoiding possible instabilities. Secondly, the aggregation of distributed resources has been simplified and the overall power system stability improved as this aggregation (and not only large power plants) can participate in the provision of ancillary services, once adequately designed and operated. Thirdly, this work also contributes in simplifying the operation of aggregated distributed resources by harnessing the potential of batteries. Finally, this thesis should contribute to a better understanding of the dynamics of MGs and to improving their safety, integration and operational capacities. These aspects should eventually result in a more reliable integration of renewable resources in power systems and a better access to electricity in remote areas. Nonetheless, there are still several aspects that should be addressed. The following section spells out some suggestions for future research derived from the research carried out so far.

7.3 Suggestions for Further Research

1. The study conducted in Chapter 3 could be enriched with more advanced control structures since the ones used were rather simple.

    - The voltage controller of the diesel gen-set was simplified for the study. However, there is a variety of automatic voltage regulator (AVR) implementations that could lead to more interactions with PLLs of GFL converters.
    - Different GFM strategies and inner control loops such as virtual impedances and admittances could affect frequency dynamics and, therefore, the performance of PLLs of GFL converters connected to the same grid.
    - Furthermore, advanced synchronisation strategies like dual second order generalized integrator (DSOGI) may present improved stability margins as briefly depicted in Chapter 3.
    - In large power systems, it has been demonstrated that the design of direct current (DC)-voltage controllers of GFL converters is related to the performance of PLLs. Despite being of interest, this aspect was not studied in detail in this work.

2. As the integration of renewable resources in power grids increases, services that were traditionally provided by large generators could be now provided by smaller plants. To make this work, academia and industry (including grid operators) should jointly redefine grid services and how they should be provisioned. In aggregations such as the one presented in Chapter 4, the uncertainties of renewable generation, the differences of available resources and technologies, and the variety of controllers used should be taken into account to offer adequate grid services. Of

course, the portfolio of services required should be made realistic via a thorough understanding of available technologies.

3. Regarding the future of secondary control, it would be of interest to study interactions between secondary controllers for frequency restoration and different implementations of droops and other primary controllers. As secondary control design is highly dependant on communication systems, more accurate delay models should be considered in the stability studies for these controllers. Hereof, stochastic functions seem to better characterise communication delays, as proposed by some authors. In addition, speed limitations of voltage secondary controllers should also be studied in more detail.

4. Even though the focus of this work was not on secondary voltage control, some findings of this work could inspire future work in this field. For example, in the coordination of MG resources. In this regard, the nodal (instead of global) nature of voltage dynamics should be considered. Possible solutions to this problem include the use of optimization tools.

Bibliography

[1] T. Morstyn, B. Hredzak, and V. G. Agelidis, "Control strategies for microgrids with distributed energy storage systems: An overview," *IEEE Transactions on Smart Grid*, vol. 9, no. 4, pp. 3652–3666, July 2018.

[2] Y. Chen, R. Hesse, D. Turschner, and H.-P. Beck, "Improving the grid power quality using virtual synchronous machines," in *2011 International Conference on Power Engineering, Energy and Electrical Drives*, 2011, pp. 1–6.

[3] S. D'Arco, J. A. Suul, and O. B. Fosso, "A virtual synchronous machine implementation for distributed control of power converters in smartgrids," *Electric Power Systems Research*, vol. 122,, pp. 180–197, 2015.

[4] R. Teodorescu, M. Liserre, and P. Rodriguez, *Grid converters for photovoltaic and wind Power Systems*. Wiley-IEEE Press, 2011.

[5] N. Hatziargyriou, J. Milanovic, C. Rahmann, V. Ajjarapu, C. Canizares, I. Erlich, D. Hill, I. Hiskens, I. Kamwa, B. Pal, P. Pourbeik, J. Sanchez-Gasca, A. Stankovic, T. Van Cutsem, V. Vittal, and C. Vournas, "Definition and classification of power system stability – revisited & extended," *IEEE Transactions on Power Systems*, vol. 36, no. 4, pp. 3271–3281, 2021.

[6] F. Milano, F. Dörfler, G. Hug, D. J. Hill, and G. Verbič, "Foundations and challenges of low-inertia systems (invited paper)," in *2018 Power Systems Computation Conference (PSCC)*, 2018, pp. 1–25.

[7] D. Infield and L. Freris, *Renewable energy in power systems*. John Wiley & Sons, 2020.

[8] D. Wang, L. Liu, H. Jia, W. Wang, Y. Zhi, Z. Meng, and B. Zhou, "Review of key problems related to integrated energy distribution systems," *CSEE Journal of Power and Energy Systems*, vol. 4, no. 2, pp. 130–145, 2018.

[9] "Commission regulation (eu) 2016/631 of 14 april 2016 establishing a network code on requirements for grid connection of generators," *Official Journal of the European Union*, vol. L 112, pp. 1–68, 2016-04-27.

[10] M. Braun, *Provision of ancillary services by distributed generators: Technological and economic perspective*. kassel university press GmbH, 2009, vol. 10.

[11] N. Hatziargyriou, *Microgrids: architectures and control*. John Wiley & Sons, 2014.

[12] D. E. Olivares, A. Mehrizi-Sani, A. H. Etemadi, C. A. Cañizares, R. Iravani, M. Kazerani, A. H. Hajimiragha, O. Gomis-Bellmunt, M. Saeedifard, R. Palma-Behnke, G. A. Jiménez-Estévez, and N. D. Hatziargyriou, "Trends in microgrid control," *IEEE Transactions on Smart Grid*, vol. 5, no. 4, pp. 1905–1919, 2014.

[13] A. Ogunjuyigbe, T. Ayodele, and O. Akinola, "Optimal allocation and sizing of pv/wind/split-diesel/battery hybrid energy system for minimizing life cycle cost, carbon emission and dump energy of remote residential building," *Applied Energy*, vol. 171, pp. 153–171, 2016.

[14] J. M. Guerrero, J. C. Vasquez, J. Matas, L. G. de Vicuna, and M. Castilla, "Hierarchical control of droop-controlled ac and dc microgrids—a general approach toward standardization," *IEEE Transactions on Industrial Electronics*, vol. 58, no. 1, pp. 158–172, 2011.

[15] A. Bidram and A. Davoudi, "Hierarchical structure of microgrids control system," *IEEE Transactions on Smart Grid*, vol. 3, no. 4, pp. 1963–1976, 2012.

[16] X. Wang, Y. W. Li, F. Blaabjerg, and P. C. Loh, "Virtual-impedance-based control for voltage-source and current-source converters," *IEEE Transactions on Power Electronics*, vol. 30, no. 12, pp. 7019–7037, 2015.

[17] H. Bevrani, T. Ise, and Y. Miura, "Virtual synchronous generators: A survey and new perspectives," *International Journal of Electrical Power and Energy Systems*, vol. 54, pp. 244–254, 2014.

[18] A. Tayyebi, D. Groß, A. Anta, F. Kupzog, and F. Dörfler, "Frequency stability of synchronous machines and grid-forming power converters," *IEEE Journal of Emerging and Selected Topics in Power Electronics*, vol. 8, no. 2, pp. 1004–1018, 2020.

[19] Q.-C. Zhong and G. Weiss, "Synchronverters: Inverters that mimic synchronous generators," *IEEE Transactions on Industrial Electronics*, vol. 58, no. 4, pp. 1259–1267, 2011.

[20] C. Arghir, T. Jouini, and F. Dörfler, "Grid-forming control for power converters based on matching of synchronous machines," *Automatica*, vol. 95, pp. 273–282, 2018.

[21] M. Colombino, D. Groß, J.-S. Brouillon, and F. Dörfler, "Global phase and magnitude synchronization of coupled oscillators with application to the control of grid-forming power inverters," *IEEE Transactions on Automatic Control*, vol. 64, no. 11, pp. 4496–4511, 2019.

[22] S. D'Arco and J. A. Suul, "Virtual synchronous machines — classification of implementations and analysis of equivalence to droop controllers for microgrids," in *2013 IEEE Grenoble Conference*, 2013, pp. 1–7.

[23] B. B. Johnson, S. V. Dhople, A. O. Hamadeh, and P. T. Krein, "Synchronization of parallel single-phase inverters with virtual oscillator control," *IEEE Transactions on Power Electronics*, vol. 29, no. 11, pp. 6124–6138, 2014.

[24] "IEEE standard for the specification of microgrid controllers," *IEEE Std 2030.7-2017*, pp. 1–43, 2018.

[25] R. Rosso, X. Wang, M. Liserre, X. Lu, and S. Engelken, "Grid-Forming Converters: Control Approaches, Grid-Synchronization, and Future Trends—A Review," *IEEE Open Journal of Industry Applications*, vol. 2, no. April, pp. 93–109, 2021.

[26] A. Yazdani and R. Iravani, *Voltage-Sourced Converters in Power Systems: Modeling, Control, and Applications*. Wiley, 2010.

[27] Y. Lin, B. Johnson, V. Gevorgian, V. Purba, and S. Dhople, "Stability assessment of a system comprising a single machine and inverter with scalable ratings," in *2017 North American Power Symposium (NAPS)*, 2017, pp. 1–6.

[28] L. Meng, J. Zafar, S. K. Khadem, A. Collinson, K. C. Murchie, F. Coffele, and G. M. Burt, "Fast Frequency Response from Energy Storage Systems - A Review of Grid Standards, Projects and Technical Issues," *IEEE Transactions on Smart Grid*, vol. 11, no. 2, pp. 1566–1581, 2020.

[29] E. N. of Transmission System Operators for Electricity (ENTSO-E), "Need for synthetic inertia (SI) for frequency regulation," 2017, https://consultations.entsoe.eu/system-development/entso-e-connection-codes-implementation-guidance-d-3/user_uploads/igd-need-for-synthetic-inertia.pdf, accessed 2023-01-13.

[30] I. R. E. A. (IRENA), "Grid codes for renewable powered systems," 2022, https://www.irena.org/-/media/Files/IRENA/Agency/Publication/2022/Apr/IRENA_Grid_Codes_Renewable_Systems_2022.pdf, accessed 2023-01-13.

[31] W. Zhong, M. A. A. Murad, M. Liu, and F. Milano, "Impact of Virtual Power Plants on Power System Short-Term Transient Response," *Electric Power Systems Research*, vol. 189, no. February, p. 106609, 2020.

[32] V. Haberle, M. W. Fisher, E. Prieto Araujo, and F. Dorfler, "Control design of dynamic virtual power plants: An adaptive divide-and-conquer approach," *IEEE Transactions on Power Systems*, pp. 1–1, 2021.

[33] Y. Khayat, Q. Shafiee, R. Heydari, M. Naderi, T. Dragičević, J. W. Simpson-Porco, F. Dörfler, M. Fathi, F. Blaabjerg, J. M. Guerrero, and H. Bevrani, "On the secondary control architectures of ac microgrids: An overview," *IEEE Transactions on Power Electronics*, vol. 35, no. 6, pp. 6482–6500, 2020.

[34] R. Heydari, Y. Khayat, A. Amiri, T. Dragicevic, Q. Shafiee, P. Popovski, and F. Blaabjerg, "Robust high-rate secondary control of microgrids with mitigation of communication impairments," *IEEE Transactions on Power Electronics*, vol. 35, no. 11, pp. 12 486–12 496, 2020.

[35] C. Cho, J.-H. Jeon, J.-Y. Kim, S. Kwon, K. Park, and S. Kim, "Active synchronizing control of a microgrid," *IEEE Transactions on Power Electronics*, vol. 26, no. 12, pp. 3707–3719, 2011.

[36] J. M. Eyer and G. P. Corey, "Energy storage for the electricity grid: benefits and market potential assessment guide: a study for the DOE energy storage systems program." *Sandia National Laboratories*, 2 2010.

[37] K. Strunz, E. Abbasi, C. Abbey, C. Andrieu, U. Annakkage, S. Barsali, R. C. Campbell, R. Fletcher, F. Gao, T. Gaunt, A. Gole, N. Hatziargyriou, R. Iravani, G. Joos, H. Konishi, M. Kuschke, E. Lakervi, C.-C. Liu, J. Mahseredjian, F. Mosallat, D. Muthumuni, A. Orths, S. Papathanassiou, K. Rudion, Z. Styczynski, and S. C. Verma, "Benchmark Systems for Network Integration of Renewable and Distributed Energy Resources," CIGRE, Tech. Rep., 2014.

[38] B. Wu, Y. Lang, N. Zagari, and S. Kouro, *Power conversion and control of wind energy systems*. Wiley IEEE Press, 2011.

[39] J. Roldán-Pérez, E. J. Bueno, R. Peña-Alzola, and A. Rodríguez-Cabero, "All-pass-filter-based active damping for vscs with LCL filters connected to weak grids," *IEEE Transactions on Power Electronics*, vol. 33, no. 11, pp. 9890–9901, 2018.

[40] K. Vatta Kkuni, S. Mohan, G. Yang, and W. Xu, "Comparative assessment of typical control realizations of grid forming converters based on their voltage source behaviour," *Energy Reports*, vol. 9, pp. 6042–6062, 2023.

[41] X. Wang, Y. W. Li, F. Blaabjerg, and P. C. Loh, "Virtual-impedance-based control for voltage-source and current-source converters," *IEEE Transactions on Power Electronics*, vol. 30, no. 12, pp. 7019–7037, 2015.

[42] P. Kundur, N. Balu, and M. Lauby, *Power system stability and control*, ser. EPRI power system engineering series. McGraw-Hill, 1994.

[43] S. Golestan, M. Monfared, and F. D. Freijedo, "Design-oriented study of advanced synchronous reference frame phase-locked loops," *IEEE Transactions on Power Electronics*, vol. 28, no. 2, pp. 765–778, Feb 2013.

[44] J. M. Guerrero, L. Hang, and J. Uceda, "Control of distributed uninterruptible power supply systems," *IEEE Transactions on Industrial Electronics*, vol. 55, no. 8, pp. 2845–2859, 2008.

[45] O. Mo, S. D. Arco, and J. A. Suul, "Evaluation of Virtual Synchronous Machines with Dynamic or Quasi-Stationary Machine Models," *IEEE Transactions on Industrial Electronics IEEE*, vol. 0046, no. c, 2016.

[46] S. A. Aghdam and M. Agamy, "Adaptive virtual inertia synthesis via enhanced dispatchable virtual oscillator controlled grid-tied inverters," in *IECON 2021 – 47th Annual Conference of the IEEE Industrial Electronics Society*, 2021, pp. 1–6.

[47] S. A. Aghdam and M. A. Agamy, "Virtual oscillator-based methods for grid-forming inverter control: A review," *IET Renewable Power Generation*, vol. 16, no. 5, pp. 835–855, 2022.

[48] M. E. Adabi and B. Marinescu, "Direct participation of dynamic virtual power plants in secondary frequency control," *Energies*, vol. 15, no. 8, p. 2775, 2022.

[49] B. Marinescu, O. Gomis-Bellmunt, F. Dörfler, H. Schulte, and L. Sigrist, "Dynamic virtual power plant: A new concept for grid integration of renewable energy sources," *IEEE Access*, vol. 10, pp. 104 980–104 995, 2022.

[50] T. Dragicevic, J. M. Guerrero, J. C. Vasquez, and D. Škrlec, "Supervisory control of an adaptive-droop regulated dc microgrid with battery management capability," *IEEE Transactions on Power Electronics*, vol. 29, no. 2, pp. 695–706, Feb 2014.

[51] J. Xiao, P. Wang, and L. Setyawan, "Hierarchical control of hybrid energy storage system in DC microgrids," *IEEE Transactions on Industrial Electronics*, vol. 62, no. 8, pp. 4915–4924, Aug 2015.

[52] C. Dong, H. Jia, Q. Xu, J. Xiao, Y. Xu, P. Tu, P. Lin, X. Li, and P. Wang, "Time-delay stability analysis for hybrid energy storage system with hierarchical control in dc microgrids," *IEEE Transactions on Smart Grid*, vol. 9, no. 6, pp. 6633–6645, Nov 2018.

[53] F. L. Lewis, H. Zhang, K. Hengster-Movric, and A. Das, *Cooperative Control of Multi-Agent Systems*. Springer, 2014.

[54] Y. Han, H. Li, L. Xu, X. Zhao, and J. M. Guerrero, "Analysis of washout filter-based power sharing strategy—an equivalent secondary controller for islanded microgrid without LBC lines," *IEEE Transactions on Smart Grid*, vol. 9, no. 5, pp. 4061–4076, 2018.

[55] Y. Sun, X. Hou, J. Yang, H. Han, M. Su, and J. M. Guerrero, "New perspectives on droop control in ac microgrid," *IEEE Transactions on Industrial Electronics*, vol. 64, no. 7, pp. 5741–5745, 2017.

[56] M. Yazdanian and A. Mehrizi-Sani, "Washout filter-based power sharing," *IEEE Transactions on Smart Grid*, vol. 7, no. 2, pp. 967–968, 2016.

[57] Y. Khayat, M. Naderi, Q. Shafiee, Y. Batmani, M. Fathi, J. M. Guerrero, and H. Bevrani, "Decentralized optimal frequency control in autonomous microgrids," *IEEE Transactions on Power Systems*, vol. 34, no. 3, pp. 2345–2353, 2019.

[58] J. M. Rey, P. Martí, M. Velasco, J. Miret, and M. Castilla, "Secondary switched control with no communications for islanded microgrids," *IEEE Transactions on Industrial Electronics*, vol. 64, no. 11, pp. 8534–8545, 2017.

[59] Z. Karami, Q. Shafiee, Y. Khayat, M. Yaribeygi, T. Dragičević, and H. Bevrani, "Decentralized model predictive control of dc microgrids with constant power load," *IEEE Journal of Emerging and Selected Topics in Power Electronics*, vol. 9, no. 1, pp. 451–460, 2021.

[60] W. Gu, G. Lou, W. Tan, and X. Yuan, "A nonlinear state estimator-based decentralized secondary voltage control scheme for autonomous microgrids," *IEEE Transactions on Power Systems*, vol. 32, no. 6, pp. 4794–4804, 2017.

[61] Y. Khayat, R. Heydari, M. Naderi, T. Dragicevic, Q. Shafiee, M. Fathi, H. Bevrani, and F. Blaabjerg, "Decentralized frequency control of ac microgrids: An estimation-based consensus approach," *IEEE Journal of Emerging and Selected Topics in Power Electronics*, vol. 9, no. 5, pp. 5183–5191, 2021.

[62] Y. Wang, Z. Chen, X. Wang, Y. Tian, Y. Tan, and C. Yang, "An estimator-based distributed voltage-predictive control strategy for AC islanded microgrids," *IEEE Transactions on Power Electronics*, vol. 30, no. 7, pp. 3934–3951, 2015.

[63] J. C. Vasquez, J. M. Guerrero, A. Luna, P. Rodriguez, and R. Teodorescu, "Adaptive droop control applied to voltage-source inverters operating in grid-connected and islanded modes," *IEEE Transactions on Industrial Electronics*, vol. 56, no. 10, pp. 4088–4096, 2009.

[64] X. Lu, K. Sun, J. M. Guerrero, J. C. Vasquez, and L. Huang, "State-of-charge balance using adaptive droop control for distributed energy storage systems in DC microgrid applications," *IEEE Transactions on Industrial Electronics*, vol. 61, no. 6, pp. 2804–2815, June 2014.

[65] ——, "Double-quadrant state-of-charge-based droop control method for distributed energy storage systems in autonomous DC microgrids," *IEEE Transactions on Smart Grid*, vol. 6, no. 1, pp. 147–157, Jan 2015.

[66] J. M. Guerrero, J. C. Vasquez, J. Matas, M. Castilla, and L. Garcia de Vicuna, "Control strategy for flexible microgrid based on parallel line-interactive ups systems," *IEEE Transactions on Industrial Electronics*, vol. 56, no. 3, pp. 726–736, 2009.

[67] D. Wu, F. Tang, T. Dragicevic, J. C. Vasquez, and J. M. Guerrero, "A control architecture to coordinate renewable energy sources and energy storage systems in islanded microgrids," *IEEE Transactions on Smart Grid*, vol. 6, no. 3, pp. 1156–1166, May 2015.

[68] ——, "Autonomous active power control for islanded ac microgrids with photovoltaic generation and energy storage system," *IEEE Transactions on Energy Conversion*, vol. 29, no. 4, pp. 882–892, Dec 2014.

[69] H. Mahmood and J. Jiang, "Autonomous coordination of multiple PV/battery hybrid units in islanded microgrids," *IEEE Transactions on Smart Grid*, vol. 9, no. 6, pp. 6359–6368, Nov 2018.

[70] N. Pogaku, M. Prodanović, and T. C. Green, "Modeling, analysis and testing of autonomous operation of an inverter-based microgrid," *IEEE Transactions on Power Electronics*, vol. 22, no. 2, pp. 613–625, March 2007.

[71] A. Mehrizi-Sani and R. Iravani, "Potential-function based control of a microgrid in islanded and grid-connected modes," *IEEE Transactions on Power Systems*, vol. 25, no. 4, pp. 1883–1891, 2010.

[72] K. De Brabandere, K. Vanthournout, J. Driesen, G. Deconinck, and R. Belmans, "Control of microgrids," in *2007 IEEE Power Engineering Society General Meeting*, 2007, pp. 1–7.

[73] M. Savaghebi, A. Jalilian, J. C. Vasquez, and J. M. Guerrero, "Secondary control for voltage quality enhancement in microgrids," *IEEE Transactions on Smart Grid*, vol. 3, no. 4, pp. 1893–1902, 2012.

[74] A. Micallef, M. Apap, C. Spiteri-Staines, J. M. Guerrero, and J. C. Vasquez, "Reactive power sharing and voltage harmonic distortion compensation of droop controlled single phase islanded microgrids," *IEEE Transactions on Smart Grid*, vol. 5, no. 3, pp. 1149–1158, 2014.

[75] M. Savaghebi, A. Jalilian, J. C. Vasquez, and J. M. Guerrero, "Secondary control scheme for voltage unbalance compensation in an islanded droop-controlled microgrid," *IEEE Transactions on Smart Grid*, vol. 3, no. 2, pp. 797–807, 2012.

[76] Y. Guan, J. C. Vasquez, and J. M. Guerrero, "Coordinated secondary control for balanced discharge rate of energy storage system in islanded AC microgrids," *IEEE Transactions on Industry Applications*, vol. 52, no. 6, pp. 5019–5028, Nov 2016.

[77] H. Bevrani, F. Habibi, P. Babahajyani, M. Watanabe, and Y. Mitani, "Intelligent frequency control in an AC microgrid: Online PSO-based fuzzy tuning approach," *IEEE Transactions on Smart Grid*, vol. 3, no. 4, pp. 1935–1944, 2012.

[78] H. Bevrani and S. Shokoohi, "An intelligent droop control for simultaneous voltage and frequency regulation in islanded microgrids," *IEEE Transactions on Smart Grid*, vol. 4, no. 3, pp. 1505–1513, 2013.

[79] D. Moutevelis, J. Roldan–Perez, and M. Prodanović, "Virtual admittance control for providing voltage support using converter interfaced generation," in *2021 IEEE PES Innovative Smart Grid Technologies Europe (ISGT Europe)*, 2021, pp. 01–06.

[80] D. Moutevelis, J. Roldan-Perez, N. Jankovic, and M. Prodanović, "Recursive secondary controller for voltage profile improvement based on primary virtual admittance control," *IEEE Transactions on Smart Grid*, pp. 1–1, 2023.

[81] T. R. Oliveira, W. W. A. Gonçalves Silva, and P. F. Donoso-Garcia, "Distributed secondary level control for energy storage management in DC microgrids," *IEEE Transactions on Smart Grid*, vol. 8, no. 6, pp. 2597–2607, Nov 2017.

[82] A. Bidram, V. Nasirian, A. Davoudi, and F. L. Lewis, *Cooperative Synchronization in Distributed Microgrid Control*. Springer, 2017.

[83] Y. Guan, L. Meng, C. Li, J. C. Vasquez, and J. M. Guerrero, "A dynamic consensus algorithm to adjust virtual impedance loops for discharge rate balancing

of AC microgrid energy storage units," *IEEE Transactions on Smart Grid*, vol. 9, no. 5, pp. 4847–4860, Sep. 2018.

[84] C. Li, T. Dragicevic, J. C. Vasquez, J. M. Guerrero, and E. A. A. Coelho, "Multi-agent-based distributed state of charge balancing control for distributed energy storage units in AC microgrids," in *2015 IEEE Applied Power Electronics Conference and Exposition (APEC)*, 2015, pp. 2967–2973.

[85] A. M. Shotorbani, B. Mohammadi-Ivatloo, L. Wang, S. Ghassem-Zadeh, and S. H. Hosseini, "Distributed secondary control of battery energy storage systems in a stand-alone microgrid," *IET Generation, Transmission Distribution*, vol. 12, no. 17, pp. 3944–3953, September 2018.

[86] T. Morstyn, B. Hredzak, and V. G. Agelidis, "Cooperative multi-agent control of heterogeneous storage devices distributed in a dc microgrid," *IEEE Transactions on Power Systems*, vol. 31, no. 4, pp. 2974–2986, July 2016.

[87] R. Lozano, M. Spong, J. A. Guerrero, and N. Chopra, "Coordination and trajectory tracking of multiple agent systems," *Automatica*, vol. 44, no. 8, pp. 2142–21–48, 2008.

[88] W. Yang, X. Wang, and H. Shi, "Optimal control nodes selection for consensus in multi-agent systems," *IFAC Proceedings Volumes*, vol. 47, no. 3, pp. 11 697–11 702, 2014.

[89] B. Wen, D. Boroyevich, R. Burgos, P. Mattavelli, and Z. Shen, "Analysis of d-q small-signal impedance of grid-tied inverters," *IEEE Transactions on Power Electronics*, vol. 31, no. 1, pp. 675–687, 2016.

[90] J. Z. Zhou, H. Ding, S. Fan, Y. Zhang, and A. M. Gole, "Impact of short-circuit ratio and phase-locked-loop parameters on the small-signal behavior of a VSC-HVDC converter," *IEEE Transactions on Power Delivery*, vol. 29, no. 5, pp. 2287–2296, 2014.

[91] L. Harnefors, X. Wang, A. G. Yepes, and F. Blaabjerg, "Passivity-Based Stability Assessment of Grid-Connected VSCs—An Overview," *IEEE Journal of Emerging and Selected Topics in Power Electronics*, vol. 4, no. 1, pp. 116–125, 2016.

[92] F. Katiraei, M. R. Iravani, and P. W. Lehn, "Small-signal dynamic model of a micro-grid including conventional and electronically interfaced distributed resources," *IET Gen, Tran. & Dis.*, vol. 1, no. 3, pp. 369–378, 2007.

[93] F. Katiraei, "Dynamic analysis and control of distributed energy resources in a micro-grid," Ph.D. dissertation, University of Toronto, 2005.

[94] X. Tang, W. Deng, and Z. Qi, "Investigation of the dynamic stability of microgrid," *IEEE Transactions on Power Systems*, vol. 29, no. 2, pp. 698–706, 2014.

[95] D. P. Morán-Río, J. Roldán-Pérez, M. Prodanović, and A. García-Cerrada, "Influence of PLL parameters on small-signal stability of microgrids with synchronous generators," in *2020 IEEE Energy Conversion Congress and Exposition (ECCE)*, 2020, pp. 2451–2458.

[96] J. Guo, T. Chen, B. Chaudhuri, and S. Y. R. Hui, "Stability of isolated microgrids with renewable generation and smart loads," *IEEE Transactions on Sustainable Energy*, vol. 11, no. 4, pp. 2845–2854, 2020.

[97] Y. Huang, X. Yuan, J. Hu, and P. Zhou, "Modeling of VSC Connected to Weak Grid for Stability Analysis of DC-Link Voltage Control," *IEEE Journal of Emerging and Selected Topics in Power Electronics*, vol. 3, no. 4, pp. 1193–1204, 2015.

[98] D. Wang, L. Liang, L. Shi, J. Hu, and Y. Hou, "Analysis of Modal Resonance between PLL and DC-Link Voltage Control in Weak-Grid Tied VSCs," *IEEE Transactions on Power Systems*, vol. 34, no. 2, pp. 1127–1138, 2019.

[99] V. Skiparev, R. Machlev, N. R. Chowdhury, Y. Levron, E. Petlenkov, and J. Belikov, "Virtual inertia control methods in islanded microgrids," *Energies*, vol. 14, no. 6, pp. 1–20, 2021.

[100] W. Zhong, J. Chen, M. Liu, M. A. A. Murad, and F. Milano, "Coordinated Control of Virtual Power Plants to Improve Power System Short-Term Dynamics," *Energies*, vol. 14, no. 4, p. 1182, 2021.

[101] J. Alipoor, Y. Miura, and T. Ise, "Stability assessment and optimization methods for microgrid with multiple vsg units," *IEEE Transactions on Smart Grid*, vol. 9, no. 2, pp. 1462–1471, 2018.

[102] U. Markovic, Z. Chu, P. Aristidou, and G. Hug, "Lqr-based adaptive virtual synchronous machine for power systems with high inverter penetration," *IEEE Transactions on Sustainable Energy*, vol. 10, no. 3, pp. 1501–1512, 2019.

[103] J. Liu, Y. Miura, H. Bevrani, and T. Ise, "A unified modeling method of virtual synchronous generator for multi-operation-mode analyses," *IEEE Journal of Emerging and Selected Topics in Power Electronics*, vol. 9, no. 2, pp. 2394–2409, 2021.

[104] J. Chen, M. Liu, and F. Milano, "Aggregated Model of Virtual Power Plants for Transient Frequency and Voltage Stability Analysis," *IEEE Transactions on Power Systems*, vol. 36, no. 5, pp. 4366–4375, 2021.

[105] A. González-Cajigas, J. Roldán-Pérez, and E. J. Bueno, "Design and Analysis of Parallel-Connected Grid-Forming Virtual Synchronous Machines for Island and Grid-Connected Applications," *IEEE Transactions on Power Electronics*, vol. 37, no. 5, pp. 5107–5121, 2022.

[106] M. Legry, J.-Y. Dieulot, F. Colas, C. Saudemont, and O. Ducarme, "Non-linear primary control mapping for droop-like behavior of microgrid systems," *IEEE Transactions on Smart Grid*, vol. 11, no. 6, pp. 4604–4613, 2020.

[107] E. Barklund, N. Pogaku, M. Prodanović, C. Hernandez-Aramburo, and T. C. Green, "Energy management in autonomous microgrid using stability-constrained droop control of inverters," *IEEE Transactions on Power Electronics*, vol. 23, no. 5, pp. 2346–2352, 2008.

[108] S. D'Arco, J. A. Suul, and O. B. Fosso, "Automatic Tuning of Cascaded Controllers for Power Converters Using Eigenvalue Parametric Sensitivities," *IEEE Transactions on Industry Applications*, vol. 51, no. 2, pp. 1743–1753, 2015.

[109] L. Rouco and F. Pagola, "An eigenvalue sensitivity approach to location and controller design of controllable series capacitors for damping power system oscillations," *IEEE Transactions on Power Systems*, vol. 12, no. 4, pp. 1660–1666, 1997.

[110] L. Rouco, "Coordinated design of multiple controllers for damping power system oscillations," *International Journal of Electrical Power & Energy Systems*, vol. 23, no. 7, pp. 517–530, 2001.

[111] J. Renedo, A. Garcia-Cerrada, L. Rouco, and L. Sigrist, "Coordinated design of supplementary controllers in vsc-hvdc multi-terminal systems to damp electromechanical oscillations," *IEEE Transactions on Power Systems*, vol. 36, no. 1, pp. 712–721, 2021.

[112] F. Milano and M. Anghel, "Impact of time delays on power system stability," *IEEE Transactions on Circuits and Systems I: Regular Papers*, vol. 59, no. 4, pp. 889–900, 2012.

[113] D. Muyizere, L. K. Letting, and B. B. Munyazikwiye, "Effects of communication signal delay on the power grid: A review," *Electronics*, vol. 11, no. 6, 2022.

[114] J. Lai, H. Zhou, X. Lu, X. Yu, and W. Hu, "Droop-based distributed cooperative control for microgrids with time-varying delays," *IEEE Transactions on Smart Grid*, vol. 7, no. 4, pp. 1775–1789, 2016.

[115] S. Liu, X. Wang, and P. X. Liu, "Impact of communication delays on secondary frequency control in an islanded microgrid," *IEEE Transactions on Industrial Electronics*, vol. 62, no. 4, pp. 2021–2031, 2015.

[116] M. Liu, I. Dassios, G. Tzounas, and F. Milano, "Stability Analysis of Power Systems With Inclusion of Realistic-Modeling WAMS Delays," *IEEE Transactions on Power Systems*, vol. 34, no. 1, pp. 627–636, 2019.

[117] M. Mottaghizadeh, F. Aminifar, T. Amraee, and M. Sanaye-Pasand, "Distributed robust secondary control of islanded microgrids: Voltage, frequency, and power sharing," *IEEE Transactions on Power Delivery*, vol. 36, no. 4, pp. 2501–2509, 2021.

[118] R. Heydari, T. Dragicevic, and F. Blaabjerg, "High-Bandwidth Secondary Voltage and Frequency Control of VSC-Based AC Microgrid," *IEEE Transactions on Power Electronics*, vol. 34, no. 11, pp. 11 320–11 331, 2019.

[119] T. Dragicevic, "Model predictive control of power converters for robust and fast operation of ac microgrids," *IEEE Transactions on Power Electronics*, vol. 33, no. 7, pp. 6304–6317, 2018.

[120] O. Babayomi, Z. Zhang, T. Dragicevic, R. Heydari, Y. Li, C. Garcia, J. Rodriguez, and R. Kennel, "Advances and opportunities in the model predictive control of microgrids: Part ii–secondary and tertiary layers," *International Journal of Electrical Power & Energy Systems*, vol. 134, p. 107339, 2022.

[121] E. A. Coelho, D. Wu, J. M. Guerrero, J. C. Vasquez, T. Dragicevic, C. Stefanović, and P. Popovski, "Small-signal analysis of the microgrid secondary control considering a communication time delay," *IEEE Transactions on Industrial Electronics*, vol. 63, no. 10, pp. 6257–6269, 2016.

[122] A. Micallef, M. Apap, C. Spiteri-Staines, and J. M. Guerrero, "Single-phase microgrid with seamless transition capabilities between modes of operation," *IEEE Transactions on Smart Grid*, vol. 6, no. 6, pp. 2736–2745, 2015.

[123] F. Tang, J. M. Guerrero, J. C. Vasquez, D. Wu, and L. Meng, "Distributed active synchronization strategy for microgrid seamless reconnection to the grid under unbalance and harmonic distortion," *IEEE Transactions on Smart Grid*, vol. 6, no. 6, pp. 2757–2769, 2015.

[124] D. Shi, X. Chen, Z. Wang, X. Zhang, Z. Yu, X. Wang, and D. Bian, "A distributed cooperative control framework for synchronized reconnection of a multi-bus microgrid," *IEEE Transactions on Smart Grid*, vol. 9, no. 6, pp. 6646–6655, 2018.

[125] T. M. L. Assis and G. N. Taranto, "Automatic reconnection from intentional islanding based on remote sensing of voltage and frequency signals," *IEEE Transactions on Smart Grid*, vol. 3, no. 4, pp. 1877–1884, 2012.

[126] C.-T. Lee, R.-P. Jiang, and P.-T. Cheng, "A grid synchronization method for droop controlled distributed energy resources converters," in *2011 IEEE Energy Conversion Congress and Exposition*, 2011, pp. 743–749.

[127] Y. Du, H. Tu, and S. Lukic, "Distributed control strategy to achieve synchronized operation of an islanded mg," *IEEE Transactions on Smart Grid*, vol. 10, no. 4, pp. 4487–4496, 2019.

[128] Y. Han, H. Li, P. Shen, E. A. A. Coelho, and J. M. Guerrero, "Review of active and reactive power sharing strategies in hierarchical controlled microgrids," *IEEE Transactions on Power Electronics*, vol. 32, no. 3, pp. 2427–2451, 2017.

[129] S.-J. Ahn, J.-W. Park, I.-Y. Chung, S.-I. Moon, S.-H. Kang, and S.-R. Nam, "Power-sharing method of multiple distributed generators considering control modes and configurations of a microgrid," *IEEE Transactions on Power Delivery*, vol. 25, no. 3, pp. 2007–2016, 2010.

[130] W. Yao, M. Chen, J. Matas, J. M. Guerrero, and Z. M. Qian, "Design and analysis of the droop control method for parallel inverters considering the impact of the complex impedance on the power sharing," *IEEE Transactions on Industrial Electronics*, vol. 58, no. 2, pp. 576–588, Feb 2011.

[131] J. He, Y. W. Li, J. M. Guerrero, F. Blaabjerg, and J. C. Vasquez, "An islanding microgrid power sharing approach using enhanced virtual impedance control scheme," *IEEE Transactions on Power Electronics*, vol. 28, no. 11, pp. 5272–5282, 2013.

[132] A. Sunjaq, P. Chen, M. Bongiorno, R. Majumder, and J. Svensson, "Frequency control by bess for smooth island transition of hydro-powered microgrid," *IET Smart Grid (In Press)*, 2022.

[133] J.-Y. Choi and D. Won, "Advanced active power control considering the characteristics of distributed energy resources in microgrid," *Journal of Electrical Engineering & Technology*, vol. 11, pp. 1100–1107, 2016.

[134] J. V. Knudsen, "Modeling, Control, and Optimization for Diesel-Driven Generator Sets," Ph.D. dissertation, Aalborg Univ., 2017.

[135] I. Boldea, *Synchronous Generators*. Taylor & Francis Group, 2006.

[136] P. C. Krause, O. Wasynczuk, and S. D. Sudhoff, *Analysis of Electric Machinery and Drive Systems*, 2nd ed. Wiley-IEEE Press, Feb. 2002.

[137] "IEEE 421.5-2016: Recommended Practice for Excitation System Models for Power System Stability Studies," IEEE, Standard, Aug 2016.

[138] A. Rodríguez-Cabero, M. Prodanović, and J. Roldán-Perez, "Analysis of dynamic properties of vscs connected to weak grids including the effects of dead time and time delays," *IEEE Transactions on Sustaible Energy*, vol. 10, no. 3, pp. 1066–1075, July 2019.

[139] A. Monti, F. Milano, E. Bompard, and X. Guillaud, *Converter-Based Dynamics and Control of Modern Power Systems*. Academic Press, 2020.

[140] L. Harnefors, "Implementation of resonant controllers and filters in fixed-point arithmetic," *IEEE Transactions on Industrial Electronics*, vol. 56, no. 4, pp. 1273–1281, 2009.

[141] "Regulations for grid connection - Energinet," https://en.energinet.dk/Electricity/Rules-and-Regulations/Regulations-for-grid-connection, accessed: 2021-03-25.

[142] "Simulink control design toolbox," https://es.mathworks.com/products/simcontrol.html, accessed: 2021-03-31.

[143] M. Prodanović, A. Rodríguez-Cabero, M. Jiménez-Carrizosa, and J. Roldán-Pérez, "A rapid prototyping environment for DC and AC microgrids: Smart Energy Integration Lab (SEIL)," in *2017 IEEE Second Int. Conf. on DC Microgrids (ICDCM)*, June 2017, pp. 421–427.

[144] F. Huerta, J. K. Gruber, M. Prodanović, and P. Matatagui, "Power-hardware-in-the-loop test beds: evaluation tools for grid integration of distributed energy resources," *IEEE Industry Applications Magazine*, vol. 22, no. 2, pp. 18–26, March 2016.

[145] P. Vorobev, P. H. Huang, M. A. Hosani, J. L. Kirtley, and K. Turitsyn, "High-Fidelity Model Order Reduction for Microgrids Stability Assessment," *IEEE Transactions on Power Systems*, vol. 33, no. 1, pp. 874–887, 2018.

[146] S. D'Arco and J. A. Suul, "Equivalence of virtual synchronous machines and frequency-droops for converter-based microgrids," *IEEE Transactions on Smart Grid*, vol. 5, no. 1, pp. 394–395, Jan 2014.

[147] F. Milano and Á. Ortega, "Frequency Divider," *IEEE Transactions on Power Systems*, vol. 32, no. 2, pp. 1493–1501, 2017.

[148] P. W. Sauer and M. A. Pai, *Power system dynamics and stability.* Pearson, 1997.

[149] F. Garofalo, L. Iannelli, and F. Vasca, *Participation factors and their connections to residues and relative gain array.* IFAC, 2002, vol. 15, no. 1.

[150] K. Ogata, *Modern Control Engineering, 4th edition.* Prentice Hall, 2002.

[151] NERC Inverter-Based Resource Performance Task Force (IRPTF), "Fast Frequency Response Concepts and Bulk Power System Reliability Needs," North American Electric Reliability Corporation (NERC), Tech. Rep. March, 2020.

[152] D. P. Morán-Río, J. Roldán-Pérez, M. Prodanović, and A. García-Cerrada, "Influence of the phase-locked loop on the design of microgrids formed by diesel generators and grid-forming converters," *IEEE Transactions on Power Electronics*, vol. 37, no. 5, pp. 5122–5137, 2022.

[153] I. The MathWorks, "Linearize Simulink Model at Model Operating Point," https://es.mathworks.com/help/slcontrol/ug/linearize-simulink-model.html, accessed 2022-05-31.

[154] B. Miao, R. Zane, and D. Maksimovic, "System identification of power converters with digital control through cross-correlation methods," *IEEE Transactions on Power Electronics*, vol. 20, no. 5, pp. 1093–1099, 2005.

[155] I. The MathWorks, "Systems of Linear Equations," https://uk.mathworks.com/help/matlab/math/systems-of-linear-equations.html, accessed 2022-08-22.

[156] ——, " mldivide Function ," https://uk.mathworks.com/help/matlab/ref/mldivide.html, accessed 2022-08-22.

[157] J. Roldán-Pérez, D. P. Morán-Rio, D. Moutevelis, P. Rodríguez-Ortega, N. Jankovic, M. E. Zarei, and M. Prodanović, "Emulation of complex grid scenarios by using power hardware in the loop (phil) techniques," in *IECON 2021 – 47th Annual Conference of the IEEE Industrial Electronics Society*, 2021, pp. 1–6.

[158] D. Liberzon, *Switching in Systems and Control.* Springer, 2003.

[159] N. Omar, M. A. Monem, Y. Firouz, J. Salminen, J. Smekens, O. Hegazy, H. Gaulous, G. Mulder, P. Van den Bossche, T. Coosemans, and J. Van Mierlo, "Lithium iron phosphate based battery – assessment of the aging parameters and development of cycle life model," *Applied Energy*, vol. 113, pp. 1575–1585, 2014.

[160] R. Wang, Q. Sun, W. Hu, Y. Li, D. Ma, and P. Wang, "SoC-Based Droop Coefficients Stability Region Analysis of the Battery for Stand-Alone Supply Systems With Constant Power Loads," *IEEE Transactions on Power Electronics*, vol. 36, no. 7, pp. 7866–7879, 2021.

Appendix A

State Space Modelling of a Microgrid

This appendix presents the state space models of the devices presented in Chapter 3. These are some of the conventions used in this chapter:

X_i^j is the value of variable x_i^j at the operating point.
x_i^{*j} is the set-point of the variable x_i^j.
x^{dq} is variable x represented in the $d-q$ axis.
x^{DQ} is variable x represented in the $D-Q$ axis.
k_{pC} and k_{iC} are the proportional and integral constants of the controller C.
A, B, C, D are state-space matrices.

A.1 State-Space Matrices of the SG

A.1.1 State-Space Matrices of the Electromechanical Model

The equations linking DQ stator and rotor flux linkages in a SG with damper windings are [42]:

$$v_{sg}^D = \frac{d\psi^D}{dt} - \omega_r \psi^Q - r_a i^D, \tag{A.1}$$

$$v_{sg}^Q = \frac{d\psi^Q}{dt} + \omega_r \psi^D - r_a i^Q, \tag{A.2}$$

$$v_f = \frac{d\psi_f}{dt} + r_f i_f, \tag{A.3}$$

$$0 = \frac{d\psi_k^D}{dt} + r_{kd} i_k^D, \tag{A.4}$$

$$0 = \frac{d\psi_k^Q}{dt} + r_{kq} i_k^Q, \tag{A.5}$$

where the stator and rotor flux linkages are defined as [42]:

$$\psi^D = -l_d i_{sg}^D + l_{afd} i_f + l_{akd} i_k^D, \tag{A.6}$$
$$\psi^Q = -l_q i_{sg}^Q + l_{akq} i_k^Q, \tag{A.7}$$
$$\psi_f = l_{ff} i_f + l_{fkd} i_k^D - l_{afd} i_{sg}^D, \tag{A.8}$$
$$\psi_k^D = l_{fkd} i_f + l_{kkd} i_k^D - l_{akd} i_{sg}^D, \tag{A.9}$$
$$\psi_k^Q = l_{kkq} i_k^Q - l_{akq} i_Q. \tag{A.10}$$

Please note that r_a is the armature resistance per phase in pu, r_f, r_{kd}, r_{kq} are the rotor circuit resistances in pu, l_d, l_q are the self-inductances of stator circuits, l_{ff}, l_{kkd}, l_{kkq} are the self-inductances of rotor circuits, l_{afd}, l_{akd}, l_{akq} are the mutual inductances stator-rotor, l_{fkd} is the mutual inductance field-damping windings and l_{ad}, l_{aq} are the stator mutual inductances. The linearization of the previous equations yields the following state-space matrices:

$$A_{EM} = M_R M_L^{-1} + M_\omega, \tag{A.11}$$

$$M_R = \begin{bmatrix} r_a & 0 & 0 & 0 & 0 \\ 0 & -r_f & 0 & 0 & 0 \\ 0 & 0 & -r_{kd} & 0 & 0 \\ 0 & 0 & 0 & r_a & 0 \\ 0 & 0 & 0 & 0 & -r_{kq} \end{bmatrix}, \tag{A.12}$$

$$M_\omega = \begin{bmatrix} 0 & 0 & 0 & \Omega_r & 0 \\ 0 & 0 & 0 & 0 & 0 \\ 0 & 0 & 0 & 0 & 0 \\ -\Omega_r & 0 & 0 & 0 & 0 \\ 0 & 0 & 0 & 0 & 0 \end{bmatrix}, \tag{A.13}$$

where M_L^{-1} is the inverse of M_L which is derived from (A.6)−(A.10) as follows:

$$\begin{bmatrix} \Delta\psi^D \\ \Delta\psi_f \\ \Delta\psi_k^D \\ \Delta\psi^Q \\ \Delta\psi_k^Q \end{bmatrix} = M_L \begin{bmatrix} \Delta i_{sg}^D \\ \Delta i_f \\ \Delta i_k^D \\ \Delta i_{sg}^Q \\ \Delta i_k^Q \end{bmatrix}, \tag{A.14}$$

where

$$M_L^{-1} = \begin{bmatrix} K_{id\_fd} & K_{id\_ff} & K_{id\_fkd} & 0 & 0 \\ K_{if\_fd} & K_{if\_ff} & K_{if\_fkd} & 0 & 0 \\ K_{ikd\_fd} & K_{ikd\_ff} & K_{ikd\_fkd} & 0 & 0 \\ 0 & 0 & 0 & K_{iq\_fq} & K_{iq\_fkq} \\ 0 & 0 & 0 & K_{ikq\_fq} & K_{ikq\_fkq} \end{bmatrix}. \tag{A.15}$$

The rest of the matrices of the electromagnetic model are:

$$B_{EM1} = \begin{bmatrix} 0 \\ 1 \\ 0 \\ 0 \\ 0 \\ 0 \end{bmatrix}, \; B_{EM2} = \begin{bmatrix} 1 & 0 \\ 0 & 0 \\ 0 & 0 \\ 0 & 1 \\ 0 & 0 \end{bmatrix}, \; B_{EM3} = \begin{bmatrix} 0 \\ \Psi^Q \\ 0 \\ 0 \\ -\Psi^D \\ 0 \end{bmatrix}, \tag{A.16}$$

$$C_{EM1} = \begin{bmatrix} (K_{iq\_fq} - K_{id\_fd})\Psi^Q + K_{iq\_fkq}\Psi_k^Q \\ -K_{id\_ff}\Psi^Q \\ -K_{id\_fkd}\Psi^Q \\ (K_{iq\_fq} - K_{id\_fd})\Psi^D - K_{id\_fd}\Psi_f - K_{id\_fkd}\Psi_k^D \\ K_{iq\_fkq}\Psi^D \end{bmatrix}^T, \tag{A.17}$$

$$C_{EM2} = \begin{bmatrix} K_{id\_fd} & K_{id\_ff} & K_{id\_fkd} & 0 & 0 \\ 0 & 0 & 0 & K_{iq\_fq} & K_{iq\_fkq} \end{bmatrix}, \tag{A.18}$$

$$C_{EM3} = \begin{bmatrix} K_{if\_fd} & K_{if\_ff} & K_{if\_fkd} & 0 & 0 \end{bmatrix}, \tag{A.19}$$

where parameters inside matrices are defined here:

$$K_{id\_fd} = \frac{-{l_{fkd}}^2 + l_{ff}l_{kkd}}{K_{id\_f}}, \; K_{id\_ff} = \frac{(l_{fkd} - l_{kkd})l_{ad}}{K_{id\_f}}, \tag{A.20}$$

$$K_{id\_fkd} = \frac{(-l_{ff} + l_{fkd})l_{ad}}{K_{id\_f}}, K_{if\_fd} = \frac{(-l_{fkd} + l_{kkd})l_{ad}}{K_{id\_f}}, \tag{A.21}$$

$$K_{if\_ff} = \frac{{l_{ad}}^2 - l_d l_{kkd}}{K_{id\_f}}, \;\; K_{if\_fkd} = \frac{-{l_{ad}}^2 + l_d l_{fkd}}{K_{id\_f}}, \tag{A.22}$$

$$K_{ikd\_fd} = \frac{(l_{ff} - l_{fkd})l_{ad}}{K_{id\_f}}, \;\; K_{ikd\_ff} = \frac{-{l_{ad}}^2 + l_d l_{fkd}}{K_{id\_f}}, \tag{A.23}$$

$$K_{ikd\_fkd} = \frac{{l_{ad}}^2 - l_d l_{ffd}}{K_{id\_f}}, \tag{A.24}$$

$$K_{id\_f} = {l_{ad}}^2(l_{ff} + l_{kkd} - 2l_{fkd}) + l_d {l_{fkd}}^2 - l_d l_{ff} l_{kkd}, \tag{A.25}$$

$$K_{iq\_f} = {l_{aq}}^2 - l_{kkq} l_q, \; K_{iq\_fq} = \frac{l_{kkq}}{K_{iq\_f}}, \tag{A.26}$$

$$K_{iq\_fkq} = \frac{-l_{aq}}{K_{iq\_f}}, \; K_{ikq\_fq} = \frac{l_{aq}}{K_{iq\_f}}, \; K_{ikq\_fkq} = \frac{-l_q}{K_{iq\_f}}. \tag{A.27}$$

A.1.2 State-Space Matrices of the Shaft

The matrices that define the linear model of the shaft are:

$$B_{S1} = \begin{bmatrix} 1/2H \end{bmatrix}, \;\; B_{S2} = \begin{bmatrix} -1/2H \end{bmatrix}, \tag{A.28}$$

being H the per unit inertia constant of the synchronous generator (SG) shaft.

A.1.3 State-Space Matrices of the Excitation Model

The following matrices are used in the excitation model:

$$A_E = \left[-(S_E + K_E)/T_E\right], \quad B_{E1} = \left[1/T_E\right], \quad C_E = \left[1\right]. \tag{A.29}$$

A.1.4 State-Space Matrices of the Diesel Engine

The model of the diesel engine is linearised around the operating point, yielding the following state-space matrices:

$$A_D = \left[\frac{-(\sigma + F)}{\tau_m(\sigma + T_m)^2}\right], \quad B_D = \left[\frac{1}{\tau_m(\sigma + T_m)}\right]. \tag{A.30}$$

A.1.5 State-Space Matrices of the AVR

The matrices below represent the state-space model of the linearised automatic voltage regulator (AVR):

$$B_{AVR1} = \left[1\right], \; B_{AVR2} = \left[\frac{-V_{sg}^D}{\sqrt{V_{sg}^{D\,2} + V_{sg}^{Q\,2}}} \quad \frac{-V_{sg}^Q}{\sqrt{V_{sg}^{D\,2} + V_{sg}^{Q\,2}}}\right], \tag{A.31}$$

$$C_{AVR} = \left[k_{iAVR}\right], \quad D_{AVR1} = \left[k_{pAVR}\right], \tag{A.32}$$

$$D_{AVR2} = \left[\frac{-V_{sg}^D k_{pAVR}}{\sqrt{V_{sg}^{D\,2} + V_{sg}^{Q\,2}}} \quad \frac{-V_{sg}^Q k_{pAVR}}{\sqrt{V_{sg}^{D\,2} + V_{sg}^{Q\,2}}}\right]. \tag{A.33}$$

A.1.6 State-Space Matrices of the Speed Governor

The matrices below represent the state-space model of the speed governor of the SG:

$$B_{Gov1} = \left[1\right], \; B_{Gov2} = \left[-1\right], \; C_{Gov} = \left[k_{iGov}\right], \tag{A.34}$$

$$D_{Gov1} = \left[k_{pGov}\right], \quad D_{Gov2} = \left[-k_{pGov}\right]. \tag{A.35}$$

A.1.7 State-Space Matrices of the Diesel Gen-Set Model

The auxiliary matrices of the diesel generator aggregated small-signal model are presented below:

$$[\Delta x_{SG}] = \left[\Delta\alpha, \Delta\beta, \Delta v_f, \Delta t_m, \Delta\psi^D, \Delta\psi_f, \Delta\psi_k^D, \Delta\psi^Q, \Delta\psi_k^Q, \Delta\omega_r\right]^T, \tag{A.36}$$

$$[\Delta u_{SG}] = \left[\Delta v_{sg}^*, \; \Delta\omega_{sg}^*, \; \Delta v_{pcc}^{DQ}\right]^T, \tag{A.37}$$

$$A_{SG} = \begin{bmatrix} 0 & 0 & 0 & 0 & 0 & 0 \\ 0 & 0 & 0 & 0 & 0 & B_{Gov2} \\ B_E C_{AVR} & 0 & A_E & 0 & B_{E2} C_{EM3} & 0 \\ 0 & B_D C_{Gov} & 0 & A_D & 0 & B_D D_{Gov2} \\ 0 & 0 & B_{EM1} C_E & 0 & A_{EM} & B_{EM3} \\ 0 & 0 & 0 & B_{S1} & B_{S2} C_{EM1} & 0 \end{bmatrix}, \tag{A.38}$$

$$B_{SG1} = \frac{1}{U_B} \left[B_{AVR1},\ 0,\ B_{E1} D_{AVR1},\ 0,\ 0,\ 0 \right]^T, \tag{A.39}$$

$$B_{SG2} = \frac{1}{\omega_B} \left[0,\ B_{Gov1},\ 0,\ B_D D_{Gov1},\ 0,\ 0 \right]^T \tag{A.40}$$

$$B_{SG3} = \frac{1}{U_B} \left[B_{AVR2},\ 0,\ B_{E1} D_{AVR2},\ 0,\ B_{EM2},\ 0 \right]^T, \tag{A.41}$$

$$C_{SG1} = I_B \left[0, 0, 0, 0, C_{EM2}, 0 \right]^T,\ C_{SG2} = \omega_B \left[0, \vdots, 0, 1 \right]^T, \tag{A.42}$$

where U_B, I_B and ω_B are the base values of voltage, current and angular frequency.

A.2 State Space Models of Converters Subsystems

A.2.1 LCL Filter Model

The complete small-signal model of the LCL filter can be found in the literature [70]. If the state variables are $x_{LCL} = [\Delta i_i^{dq}\ \Delta v_c^{dq}\ \Delta i_o^{dq}]^T$, then:

$$[\dot{x}_{LCL}]_i = A^i_{LCL} [x_{LCL}]_i + B^i_{LCL1} \left[\Delta v_i^{dq} \right]_i + B^i_{LCL2} \left[\Delta v_{pcc}^{dq} \right]_i + B^i_{LCL3} \left[\Delta \omega_{PLL} \right]_i, \tag{A.43}$$

where i denotes the ith converter, v_i is the voltage command generated for the modulation stage and ω_{PLL} is the angular frequency generated by the PLL. The LCL filter auxiliary matrices are presented below:

$$A^i_{LCL} = \begin{bmatrix} \frac{-R_i}{L_i} & \Omega_i & \frac{-1}{L_i} & 0 & 0 & 0 \\ -\Omega_i & \frac{-R_i}{L_i} & 0 & \frac{-1}{L_i} & 0 & 0 \\ \frac{1}{C_d} & 0 & 0 & \Omega_i & \frac{-1}{C_d} & 0 \\ 0 & \frac{1}{C_d} & -\Omega_i & 0 & 0 & \frac{-1}{C_d} \\ 0 & 0 & \frac{1}{L_o} & 0 & \frac{-R_o}{L_o} & \Omega_i \\ 0 & 0 & 0 & \frac{1}{L_o} & -\Omega_i & \frac{-R_o}{L_o} \end{bmatrix}_i, \tag{A.44}$$

$$B^i_{LCL1} = \begin{bmatrix} \frac{1}{L_i} & 0 \\ 0 & \frac{1}{L_i} \\ 0 & 0 \\ 0 & 0 \\ 0 & 0 \\ 0 & 0 \end{bmatrix}_i, B^i_{LCL2} = \begin{bmatrix} 0 & 0 \\ 0 & 0 \\ 0 & 0 \\ 0 & 0 \\ \frac{-1}{L_o} & 0 \\ 0 & \frac{-1}{L_o} \end{bmatrix}_i, \tag{A.45}$$

$$B^i_{LCL3} = \left[I_{iq}, -I_{id}, V_{oq}, -V_{od}, I_{oq}, -I_{od} \right]^T_i. \tag{A.46}$$

A.2.2 Current Controller

A current controller generates the command for the modulation stage of the VSC $(v_i^{*dq})_i$ [70]:

$$\left[\Delta\dot{\gamma}^{dq}\right]_i = B^i_{CC1}\left[\Delta i_i^{*dq}\right]_i + B^i_{CC2}[x_{LCL}]_i, \tag{A.47}$$

$$\left[\Delta v_i^{*dq}\right]_i = C^i_{CC}\left[\Delta\gamma^{dq}\right]_i + D^i_{CC1}\left[\Delta i_i^{*dq}\right]_i + D^i_{CC2}[x_{LCL}]_i. \tag{A.48}$$

The current controller is defined by the following space state matrices:

$$B^i_{CC1} = \begin{bmatrix}1 & 0\\ 0 & 1\end{bmatrix}_i, B^i_{CC2}\begin{bmatrix}-1 & 0 & 0 & 0 & 0 & 0\\ 0 & -1 & 0 & 0 & 0 & 0\end{bmatrix}_i, \tag{A.49}$$

$$C^i_{CC} = \begin{bmatrix}k_{ic} & 0\\ 0 & k_{ic}\end{bmatrix}_i,\ D^i_{CC1} = \begin{bmatrix}k_{pc} & 0\\ 0 & k_{pc}\end{bmatrix}_i, \tag{A.50}$$

$$D^i_{CC2} = \begin{bmatrix}-k_{pc} & -w_nL_i & 0 & 0 & 0 & 0\\ w_nL_i & -k_{pc} & 0 & 0 & 0 & 0\end{bmatrix}_i. \tag{A.51}$$

A.2.3 Current Set-Point Calculation

The set-point is calculated in terms of the active and reactive power references. These equations are non-linear, so they have to be linearised. The non-linear equations are:

$$i^{*d} = \frac{p^*v^d_{pcc} + q^*v^q_{pcc}}{{v^d_{pcc}}^2 + {v^q_{pcc}}^2},\quad i^{*q} = \frac{-q^*v^d_{pcc} + p^*v^q_{pcc}}{{v^d_{pcc}}^2 + {v^q_{pcc}}^2}, \tag{A.52}$$

while the linearised model is:

$$\left[\Delta i_i^{*dq}\right]_i = D^i_{I1}\begin{bmatrix}\Delta p^*\\ \Delta q^*\end{bmatrix}_i + D^i_{I2}\left[\Delta v^{dq}_{pcc}\right]_i, \tag{A.53}$$

with

$$D^i_{I1} = \begin{bmatrix}\frac{V_{bd}}{V_{bd}^2+V_{bq}^2} & \frac{V_{bq}}{V_{bd}^2+V_{bq}^2}\\ \frac{V_{bq}}{V_{bd}^2+V_{bq}^2} & \frac{-V_{bd}}{V_{bd}^2+V_{bq}^2}\end{bmatrix}_i, \tag{A.54}$$

$$D^i_{I2} = \begin{bmatrix}\frac{P(V_{bd}^2+V_{bq}^2)-2V_{bd}(PV_{bd}+QV_{bq})}{(V_{bd}^2+V_{bq}^2)^2} & \frac{Q(V_{bd}^2+V_{bq}^2)-2V_{bq}(PV_{bd}+QV_{bq})}{(V_{bd}^2+V_{bq}^2)^2}\\ \frac{-Q(V_{bd}^2+V_{bq}^2)-2V_{bd}(-QV_{bd}+PV_{bq})}{(V_{bd}^2+V_{bq}^2)^2} & \frac{P(V_{bd}^2+V_{bq}^2)-2V_{bq}(-QV_{bd}+PV_{bq})}{(V_{bd}^2+V_{bq}^2)^2}\end{bmatrix}_i. \tag{A.55}$$

A.2.4 State-Space Matrices of the PLL

The state-space model of the PLL is defined by the matrices below:

$$A^i_{PLL} = \begin{bmatrix} A_{PLL_{ee}} & A_{PLL_{ed}} \\ A_{PLL_{de}} & A_{PLL_{dd}} \end{bmatrix}_i = \begin{bmatrix} 0 & k_{ipll}T^{-1}_{Vd} \\ 1 & k_{ppll}T^{-1}_{Vd} \end{bmatrix}_i, \tag{A.56}$$

$$B^i_{PLL1} = \begin{bmatrix} B_{PLL1e} \\ B_{PLL1d} \end{bmatrix}_i = \begin{bmatrix} k_{ipll}T^{-1}_{Sd} \\ k_{ppll}T^{-1}_{Sd} \end{bmatrix}_i, \tag{A.57}$$

$$B^i_{PLL2} = \begin{bmatrix} B_{PLL2e} \\ B_{PLL2d} \end{bmatrix}_i = \begin{bmatrix} 0 \\ -1 \end{bmatrix}_i. \tag{A.58}$$

A.2.5 Voltage Controller

A proportional-integral (PI) controller is used to control the voltage of the alternating current (AC) capacitor. This controller is modelled as in [70]. The linearised equations are:

$$\left[\Delta\dot{\phi}^{dq}\right]_i = B^i_{VC1}\left[\Delta v_c^{*dq}\right]_i + B^i_{VC2}[x_{LCL}]_i, \tag{A.59}$$

$$\left[\Delta i_i^{*dq}\right]_i = C^i_{VC}\left[\Delta\phi^{dq}\right]_i + D^i_{VC1}\left[\Delta v_c^{*dq}\right]_i + D^i_{VC2}[x_{LCL}]_i. \tag{A.60}$$

The state-space matrices of the voltage controller are:

$$B^i_{VC1} = \begin{bmatrix} 1 & 0 \\ 0 & 1 \end{bmatrix}_i,\ B^i_{VC2}\begin{bmatrix} 0 & 0 & -1 & 0 & 0 & 0 \\ 0 & 0 & 0 & -1 & 0 & 0 \end{bmatrix}_i, \tag{A.61}$$

$$C^i_{VC} = \begin{bmatrix} k_{iv} & 0 \\ 0 & k_{iv} \end{bmatrix}_i,\ D^i_{VC1} = \begin{bmatrix} k_{pv} & 0 \\ 0 & k_{pv} \end{bmatrix}_i, \tag{A.62}$$

$$D^i_{VC2} = \begin{bmatrix} 0 & 0 & -k_{pv} & -w_nC_f & 0 & 0 \\ 0 & 0 & w_nC_f & -k_{pv} & 0 & 0 \end{bmatrix}_i. \tag{A.63}$$

A.2.6 Droop Controller

Frequency and voltage droop controllers are implemented together with active and reactive power low-pass filters to obtain the voltage and frequency set-points [70]. Instantaneous active and reactive powers are calculated as follows:

$$p = v_o^d i_o^d + v_o^q i_o^q, \quad q = -v_o^d i_o^q + v_o^q i_o^d. \tag{A.64}$$

In addition, ω_{nd} and v_{nd} are considered as inputs of the system. Calling $x_{pq} = [\Delta\delta\ \ \Delta\tilde{P}\ \ \Delta\tilde{Q}]$, then:

$$\left[\dot{x}_{pq}\right]_i = A^i_P\left[x_{pq}\right]_i + B^i_{P1}\left[x_{LCL}\right]_i + B^i_{PIn}\begin{bmatrix} \Delta\omega_{nd} \\ \Delta v_{nd}^{dq} \end{bmatrix}_i + B^i_{PV}\left[\Delta v_o^{dq}\right]_i, \tag{A.65}$$

$$\left[\Delta\omega_{com}\right]_i = C^i_{P\omega}\left[x_{pq}\right]_i + D^i_{P\omega}\begin{bmatrix}\Delta\omega_{nd}\\ \Delta v^{dq}_{nd}\end{bmatrix}_i, \tag{A.66}$$

$$\left[\Delta v^{*dq}_c\right]_i = C^i_{PV}\left[x_{pq}\right]_i + D^i_{PV}\begin{bmatrix}\Delta\omega_{nd}\\ \Delta v^{dq}_{nd}\end{bmatrix}_i, \tag{A.67}$$

where

$$A^i_P = \begin{bmatrix}0 & -m_p & 0\\ 0 & -\omega_c & 0\\ 0 & 0 & -\omega_c\end{bmatrix}_i, \tag{A.68}$$

$$B^i_{P1} = \begin{bmatrix}0 & 0 & 0 & 0 & \omega_c V_{o_d} & \omega_c V_{o_q}\\ 0 & 0 & 0 & 0 & \omega_c V_{o_q} & -\omega_c V_{o_d}\end{bmatrix}_i,\ B^i_{P\omega} = \begin{bmatrix}-1\\ 0\\ 0\end{bmatrix}_i, \tag{A.69}$$

$$B^i_{PIn} = \begin{bmatrix}1 & 0 & 0\\ 0 & 0 & 0\\ 0 & 0 & 0\end{bmatrix}_i,\ B^i_{PV} = \begin{bmatrix}0 & 0\\ \omega_c I_{o_d} & \omega_c I_{o_q}\\ -\omega_c I_{o_q} & \omega_c I_{o_d}\end{bmatrix}_i, \tag{A.70}$$

$$C^i_{P\omega} = \begin{bmatrix}0 & -m_p & 0\end{bmatrix}_i,\ C^i_{PV} = \begin{bmatrix}0 & 0 & 0\\ 0 & 0 & -n_q\end{bmatrix}_i, \tag{A.71}$$

$$D^i_{P\omega} = \begin{bmatrix}1\end{bmatrix}_i,\ D^i_{PV} = \begin{bmatrix}0 & 0\\ 0 & 1\end{bmatrix}_i. \tag{A.72}$$

A.2.7 State-Space Matrices for Reference Frame Transformations

The following matrices are used for transformations between reference frames:

$$\left[\Delta i_{o_{DQ}}\right]_i = T^i_S\left[i_{o_{dq}}\right]_i + T^i_C\left[\Delta\delta\right]_i, \tag{A.73}$$

$$T^i_S = \begin{bmatrix}\cos\delta_0 & -\sin\delta_0\\ \sin\delta_0 & \cos\delta_0\end{bmatrix}_i, \tag{A.74}$$

$$T^i_C = \begin{bmatrix}-I_{od}\sin\delta_0 - I_{oq}\cos\delta_0\\ I_{od}\cos\delta_0 - I_{oq}\sin\delta_0\end{bmatrix}_i, \tag{A.75}$$

$$\left[\Delta v_{b_{dq}}\right]_i = T^{-1i}_S\left[v_{b_{DQ}}\right]_i + T^{-1i}_V\left[\Delta\delta\right]_i. \tag{A.76}$$

$$T^{-1i}_V = \begin{bmatrix}-V_{bd}\sin\delta_0 + V_{bq}\cos\delta_0\\ -V_{bd}\cos\delta_0 - V_{bq}\sin\delta_0\end{bmatrix}_i, \tag{A.77}$$

where δ_0 has been used instead of Δ to avoid confusion with the incremental operator "Δ".

A.2.8 State-Space Matrices of the GFL Converter

The matrices used in the grid-following (GFL) converter model are:

$$A^{GFL} = \begin{bmatrix} A_{PLLee} & A_{PLLed} & 0 & 0 \\ A_{PLLde} & A_{PLLdd} & 0 & 0 \\ 0 & B_{CC1}D_{I2}T_{Vd}^{-1} & 0 & B_{CC2} \\ B_{LCL3}A_{PLLde} & \begin{matrix} B_{LCL3}A_{PLLdd} \\ +(B_{LCL1}D_{CC1}D_{I2} \\ +B_{LCL2})T_{Vd}^{-1} \end{matrix} & B_{LCL1}C_{CC} & A_{LCL} + B_{LCL1}D_{CC2} \end{bmatrix}, \tag{A.78}$$

$$B_{PQ}^{GFL} = \begin{bmatrix} 0, & 0, & B_{CC1}D_{I1}, & B_{LCL1}D_{CC1}D_{I1} \end{bmatrix}^T, \tag{A.79}$$

$$B_V^{GFL} = \begin{bmatrix} B_{PLL1e} \\ B_{PLL1d} \\ B_{CC1}D_{I2}T_S^{-1} \\ (B_{LCL1}D_{CC1}D_{I2} + B_{LCL2})T_S^{-1} \\ +B_{LCL3}B_{PLL1d} \end{bmatrix}, \tag{A.80}$$

$$B_\omega^{GFL} = \begin{bmatrix} B_{PLL2e}, & B_{PLL2d}, & 0, & 0 \end{bmatrix}^T, \tag{A.81}$$

$$C^{GFL} = \begin{bmatrix} 0 & T_C & 0 & T_S \end{bmatrix}. \tag{A.82}$$

A.2.9 State-Space Matrices of the Droop-Controlled Converter

The matrices of the GFM converter are:

$$A^{GFM} = \begin{bmatrix} A_P + B_{PV}\begin{bmatrix} T_V^{-1} & 0 \end{bmatrix} & 0 & 0 & B_{P1} \\ B_{VC1}C_{PV} + B_{VC3}\begin{bmatrix} T_V^{-1} & 0 \end{bmatrix} & A_{VC} & 0 & B_{VC2} \\ B_{CC1}D_{VC1}C_{PV} + B_{CC1}D_{VC3}\begin{bmatrix} T_V^{-1} & 0 \end{bmatrix} & B_{CC1}C_{VC} & A_{CC} & B_{CC1}D_{VC2} + B_{CC2} \\ \begin{matrix} B_{LCL1}D_{CC_1}D_{VC_1}C_{P_V} \\ +B_{LCL3}C_{P\omega} \end{matrix} & B_{LCL1}D_{CC1}C_{VC} & B_{LCL1}C_{CC} & \begin{matrix} A_{LCL} \\ +B_{LCL1}D_{CC1}D_{VC2} \\ +B_{LCL1}D_{CC2} \end{matrix} \\ +(B_{LCL1}D_{CC1}D_{VC3} + B_{LCL2})\begin{bmatrix} T_V^{-1} & 0 \end{bmatrix} & & & \end{bmatrix} \tag{A.83}$$

$$B_{In}^{GFM} = \begin{bmatrix} B_{PIn} \\ B_{VC1}\begin{bmatrix} 0 & D_{PV} \end{bmatrix} \\ B_{CC1}D_{VC1}\begin{bmatrix} 0 & D_{PV} \end{bmatrix} \\ \begin{bmatrix} B_{LCL3}D_{P\omega} & B_{LCL1}D_{CC1}D_{VC1}D_{PV} \end{bmatrix} \end{bmatrix}, \tag{A.84}$$

$$B_V^{GFM} = \begin{bmatrix} B_{PV}T_s^{-1} \\ B_{VC3}T_s^{-1} \\ B_{CC1}D_{VC3}T_s^{-1} \\ (B_{LCL2} + B_{LCL1}D_{CC1}D_{VC3})T_s^{-1} \end{bmatrix}, \tag{A.85}$$

$$B_{\omega com}^{GFM} = \begin{bmatrix} B_{P\omega} \\ [0] \end{bmatrix}, \; C_I^{GFM} = \begin{bmatrix} \begin{bmatrix} T_C & 0 \end{bmatrix} & [0] & \begin{bmatrix} 0 & T_C \end{bmatrix} \end{bmatrix}, \tag{A.86}$$

$$C_\omega^{GFM} = \begin{bmatrix} C_{P\omega} & 0 \end{bmatrix}, \; D_\omega^{GFM} = \begin{bmatrix} D_{P\omega} & 0 \end{bmatrix}. \tag{A.87}$$

A.3 State-Space Matrices of Linear $R - L$ Load

The state-space matrices of the load are:

$$A_L = \begin{bmatrix} \frac{-R_l}{L_l} & \Omega_{sg} \\ -\Omega_{sg} & \frac{-R_l}{L_l} \end{bmatrix}, \; B_{L1} = \begin{bmatrix} \frac{1}{L_l} & 0 \\ 0 & \frac{1}{L_l} \end{bmatrix}, \tag{A.88}$$

$$B_{L2} = \begin{bmatrix} I_L^Q \\ -I_L^D \end{bmatrix}, \; C_L = \begin{bmatrix} 1 & 0 \\ 0 & 1 \end{bmatrix}. \tag{A.89}$$

A.4 State-Space Matrices of the Auxiliary Resistor

The state-space matrices of the auxiliary R are:

$$D_{R1} = \begin{bmatrix} \frac{1}{R_x} & 0 \\ 0 & \frac{1}{R_x} \end{bmatrix}, \; D_{R2} = \begin{bmatrix} \frac{-1}{R_x} & 0 \\ 0 & \frac{-1}{R_x} \end{bmatrix}. \tag{A.90}$$

Appendix B

Description of the Smart Energy Integration Laboratory (SEIL)

This appendix briefly describes the laboratory facilities of the IMDEA Energy Institute where experimental results were obtained. Additional information about its hardware, control, communications and implementations can be found in [143, 144, 157].

B.1 Smart Energy Integration Laboratory (SEIL)

The Smart Energy Integration Laboratory (SEIL) is a hardware in the loop platform specifically build to test control algorithms of power converters and microgrid (MG) controllers. It consists of several power electronic converters, a motor bank and a load bank that can be controlled and operated in real time. The control structure allows the implementation of primary, secondary and tertiary control layers. The hardware and the control and communications infrastructure are described in the following sections.

B.2 Hardware

Fig. B.1 represents the single line electrical diagram of the SEIL. The following infrastructure and devices can be found:

- Configurable alternating current (AC) panel (red). It consists of five AC busbars. Different network topologies can be implemented using the network impedances and the state of contactors. Contactors are managed from a compactRIO platform. The same platform is used to monitor voltage and current magnitudes at each node.
- Configurable network impedances (purple). A set of four impedances located between the AC bus bars can be used to emulate the line impedances between nodes.

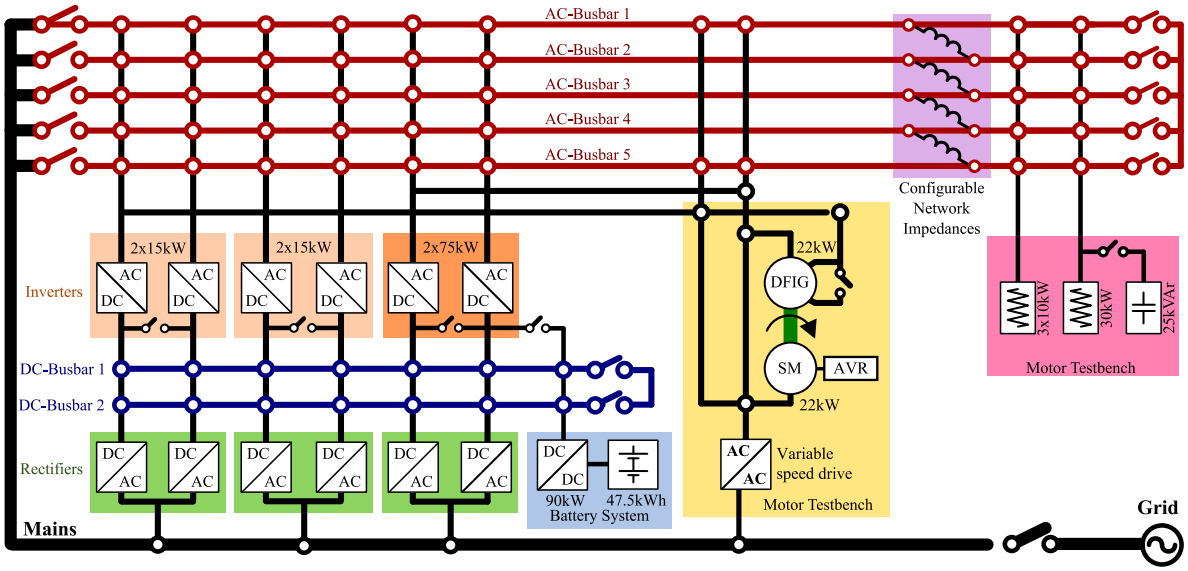

Figure B.1: Single-line electrical diagram of the SEIL.

Both the inductive and the resistive parts of the impedances are configurable.

- Configurable direct current (DC) panel (blue). Two DC busbars can be used to interconnect the DC side of power converters in different ways. Additionally, DC breakers and isolation measurements are included in the panel.

- Programmable passive load bank (pink). The load bank consists of a balanced resistive load bank of 30 kW that can be configured in steps of 3 kW, an unbalanced resistive load bank of 30 kW configurable in steps of 1 kW per phase and a capacitive load bank of 25 kvar.

- Four three-phase 15 kVA AC/DC power electronic converters (light orange). Each converter has a non-controlled rectifier (green) and a step-up transformer. They can be interconnected to the ac panel through an LC or an LCL filter. Converters are controlled in pairs with an embedded computer. This enables their back-to-back operation.

- Two three phase 75 kVA AC/DC power electronic converters (orange). Their topology is similar to the 15 kVA converters topology. However, their control system is implemented in independent control platforms. One of them has its DC side connected to an additional DC/DC converter (light blue).

- One 90 kW DC/DC converter with standard buck configuration (light blue). This one can used together with one a 75 kVA AC/DC converters as an electronic interface for the batteries.

- One 47.5 kWh lithium-ion battery system (light blue). It consists of 144 cells of 3.3 V, giving a total rated voltage of 475 V. This battery is connected to the low-voltage side of the DC/DC converter. A battery management system (BMS) sends via CAN bus the battery information (level of charge, voltage, etc.) to a central controller.

- A motor bank (yellow). It comprises a synchronous generator (SG) rated at 22 kW with an exciter and an automatic voltage regulator (AVR). The SG is coupled via the shaft to a doubly-fed induction generator (DFIG), also rated at 22 kW. A variable speed drive can either control the DFIG (with the rotor in short circuit configuration) or the SG. The machine that is not controlled by the drive can be connected to the AC panel

B.3 Control and Communications

Fig. B.2 shows the control and communications diagram of the laboratory. The control structure is very similar to the hierarchical control of a real MG. It consists of three levels: primary, secondary and tertiary. Primary control is local, that is, only local measurements are available. Primary controllers are implemented in Matlab Simulink that is run in a PC. Simulink models containing the controllers are converted to c-code, compiled and executed in real time targets (RTT). Real time communication between RTT and PC makes it possible to control and have access to control and electrical magnitudes in real time. Apart from primary control, this structure can be used to emulate small electrical grids and devices as done in Chapter 3 and in [157]. In this case, the model of the emulated system is included in Matlab/Simulink model as part of the primary control.

Since secondary control performs coordination tasks, information from all over the grid is necessary. Four CompactRIO and PLC gather the information of the devices in the grid. The information is sent using TCP/IP protocol to a LabVIEW application that is used to visualize the state of the grid and configure the laboratory topology.

Tertiary control is implemented on an external platform. It can be performed from a remote PC communicating via a VPN tunnel.

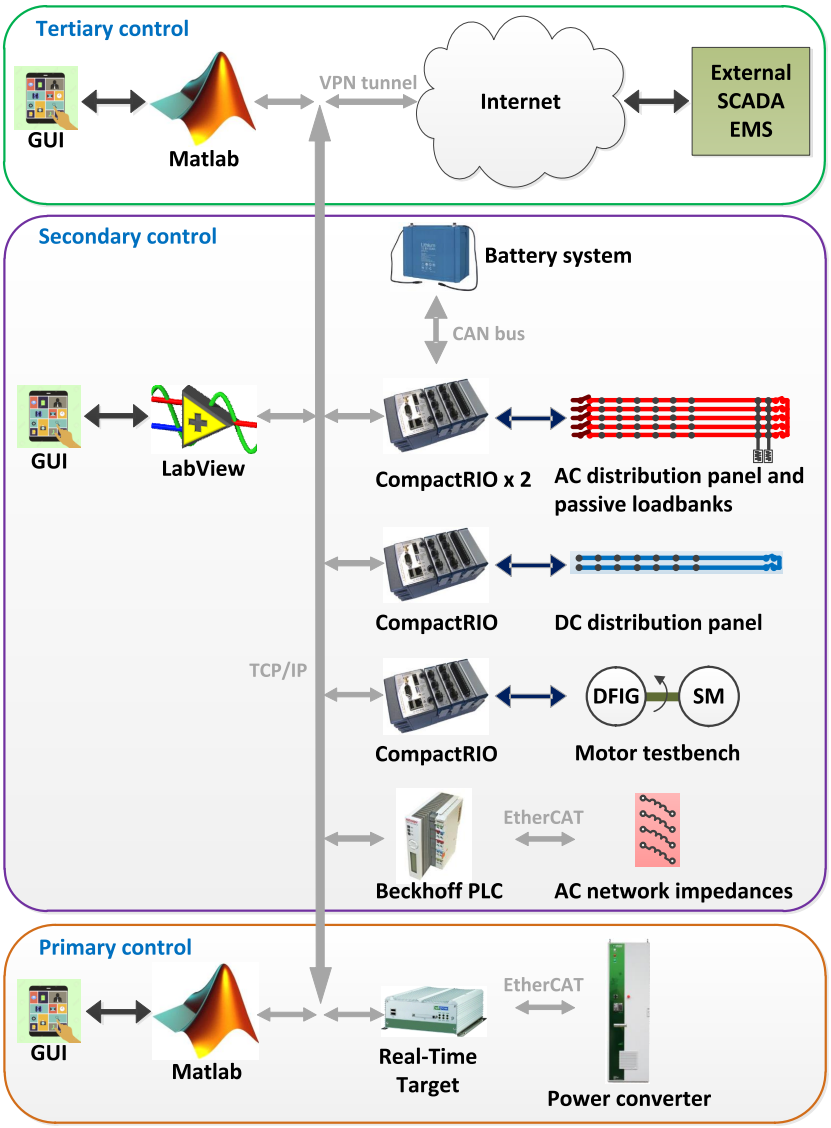

Figure B.2: Control and communications diagram of the SEIL.